Matrix Metalloproteinase-Responsive Superparamagnetic Iron Oxide Nanoparticles (SPIONs) to Distinguish Between Aggressive and Indolent Cancer

by

Tareq Anani

A dissertation submitted to the Graduate Faculty of
Auburn University
in partial fulfillment of the
requirements for the Degree of
Doctor of Philosophy

Auburn, Alabama
May 5, 2018

Keywords: Protease-responsive nanoparticles, molecular imaging, superparamagnetic iron oxide nanoparticles, multispectral optoacoustic tomography, contrast agent

Approved by

Dr. Allan E. David, Chair, Associate Professor of Chemical Engineering
Dr. Peter R Panizzi, Associate Professor of Drug Discovery and Development
Dr. Elizabeth A Lipke, Associate Professor of Chemical Engineering
Dr. Jin Wang, Associate Professor of Chemical Engineering

Abstract

Biomedical imaging modalities play a key role in the detection and accurate characterization of cancer lesions. While anatomical imaging modalities provide essential information about the location and size of a tumor lesion, they provide little regarding the genetic and molecular abnormalities that characterize various stages of tumorigenesis. On the other hand, molecular imaging modalities detect molecular level changes associated with early stages of tumor progression. Proteases are a class of biomolecules that are heavily involved in tumorigenesis, both at the primary and metastatic sites. The expression of one specific protease, matrix metalloproteinase-2 (MMP-2), correlates with tumor grade, and its catalytic nature and presence in the tumor microenvironment make it an excellent imaging target. While several imaging agents have already been developed to detect MMP-2 activity in the tumor microenvironment, the majority suffer from glaring limitations that hamper clinical success. The goal of this project was to develop a pharmacokinetically stable and tumor targeting imaging agent, based on superparamagnetic iron oxide nanoparticles (SPIONs), for quantifying MMP-2 activity. SPIONs were chosen as the base material due to their favorable toxicity profiles, biocompatibility, and unique physiochemical properties. The surface of SPIONs was decorated with an MMP-2 specific peptide for protease targeting, polyethylene glycol (PEG) for colloidal stability, Cy7 fluorophore for *in vivo* tracking with multispectral optoacoustic tomography (MSOT), and an RGD peptide for active tumor targeting. Extensive *in vitro* and *in vivo* characterization of the imaging agent was

conducted, with the agent showing tremendous potential as a diagnostic tool for early detection and accurate characterization of tumor lesions.

Acknowledgments

First, I want to thank my Ph.D. advisor Dr. Allan E. David for his steady encouragement and guidance throughout this journey. Your work ethic, intellect, and enthusiasm have made me a better researcher, and more importantly, a better person. You are a wonderful parent, friend, and teacher. You have consistently demonstrated a genuine caring for the well-being of your students. Thank you for being an excellent listener and a patient mentor.

Thank you, Dr. Peter Panizzi, Dr. Elizabeth Lipke, and Dr. Jin Wang (committee members), for your encouragement and support. Thank you, Dr. Ramesh Jeganathan, for being my university reader. Thank you, Dr. Eduardus Duin, for helping me with EPR. Thank you, Dr. Andrew Brannen, for helping me run all the *in vivo* studies. Thank you to the Auburn University Research Initiative in Cancer (AURIC) for three years of graduate fellowship support.

Thank you to all the members of the David Lab: Dr. Young Suk Choi, Dr. Xin Fan, Dr. Barry Yeh, Hunter Rogers, Dr. Alex Kelly, Alan Hanley, Prachi Sangle, Richard Cullum, Ricky Whitener, Camille Hanot, Chelsea Harris, and Marjan Azadi. Thank you Connor Read, Megan Webb, Leslie Langford, Bram Duke and Kareem Elkattan for many years of undergraduate assistance. Thank you, Dr. Mario Eden, Karen Cochran, Elaine Manning and all the other members of the Chemical Engineering Department.

Dear Mom, Dad, and Brothers – it's hard to express how thankful I am for all you've ever done for me. You are the most generous, kind, loving, and caring people I know. Thank you for a

lifetime of support and for always guiding me in the right direction. None of this would be possible without your support.

Table of Contents

List of Tables

List of Illustrations

List of Abbreviations

APMA	4-Aminophenylmercuric acetate
CT	Computed Tomography
DLS	Dynamic Light Scattering
EPR	Electron Paramagnetic Resonance
FRET	Fluorescence Resonance Energy Transfer
k_{cat}	Turnover number
Km	Michaelis constant
MAL-PEG-NHS	Maleimide-polyethylene glycol- N-Hydroxysuccinimide
MNP	Magnetic nanoparticles
MRI	Magnetic Resonance Imaging
MSOT	Multispectral Optoacoustic Tomography
NIRF	Near-infrared fluorescence
PBS	Phosphate buffered saline
PDI	Polydispersity index
PEG	Polyethylene Glycol
RES	Reticuloendothelial system
ROI	Region of interest
SPIONs	Superparamagnetic Iron Oxide Nanoparticles
SQUID	Super quantum interference device

Chapter 1 Introduction

The American Cancer Society have estimated approximately 1,700,000 new cases and 600,000 cancer-related deaths in 2017 in the United States, making it the second deadliest disease behind heart disease [1]. The success of cancer treatment relies on early and accurate diagnosis. While anatomical imaging modalities provide excellent structural information with high resolution, they provide little information about the tumor's biology and are therefore not well-suited for early diagnosis of cancer. On the other hand, molecular imaging detects, with high sensitivity, the molecular level changes that characterize the progression of cancer from an indolent to an aggressive stage [2,3]. Matrix metalloproteinases (MMPs) are excellent molecular imaging targets due to their catalytic nature and elevated expression at the invasive front of carcinomas [4]. In addition, the expression of MMPs correlates with tumor invasiveness and aggressiveness. For example, it's been shown that the expression of MMP-2 correlates with tumor grade in several types of cancer, including the prostate [5,6], brain [7], colorectal, gastric [8], and non-small cell lung cancer [9].

Accurate quantification of proteolytic activity at the tumor site remains a challenge. This is due to significant limitations in the design of the imaging probes and applicability of the imaging modalities frequently used for quantification of proteolytic activity. Small molecule probes are non-tissue specific; cleared quickly from circulation; and subject to degradation and photobleaching [10]. In addition, most probes rely on near-infrared fluorescence (NIRF) imaging that

is hampered by limited tissue penetration caused by strong light scattering and attenuation [11–13]. One alternative is to rely on multispectral optoacoustic tomography (MSOT) – a novel biomedical imaging modality that combines the high contrast of optical imaging with the high resolution and great penetration depth of ultrasound imaging [14].

The main objective of this research project was to create a molecular imaging probe that: **A.** withstands the harsh conditions of plasma and avoids quick clearance, **B.** possesses strong optoacoustic properties for sensitive MSOT imaging, **C.** specifically targets the tumor microenvironment, and **D.** demonstrates high specificity towards MMP-2. The imaging probe consisted of polyethylene glycol-conjugated (PEGylated) superparamagnetic iron oxide nanoparticles (SPIONs), a near-infrared fluorescent dye that resisted proteolytic cleavage, another fluorescent dye attached to the surface via an MMP-2 cleavable peptide linker (GPLGVRGC) [11,15–17], and a tumor-targeting ligand (**Figure 1.1**).

In chapter 3, we discuss the synthesis of PEGylated SPIONs and subsequent experiments aimed to simulate the reticuloendothelial system (RES) resistance process. In chapter 4, we discuss the development of dual fluorochrome SPIONs with strong optoacoustic properties and introduce the first MSOT phantom study. In chapter 5, we discuss the *in vitro* and *in vivo* effect of varying PEG's molecular weight on SPION stability, pharmacokinetics biodistribution. In chapter 6, we discuss the synthesis of an MMP-2 responsive probe and subsequent study of its sensitivity and specificity towards MMP-2. In chapter 7, we discuss the development of tumor-targeting (RGD and F3-conjugated) SPIONs and subsequent cellular uptake studies.

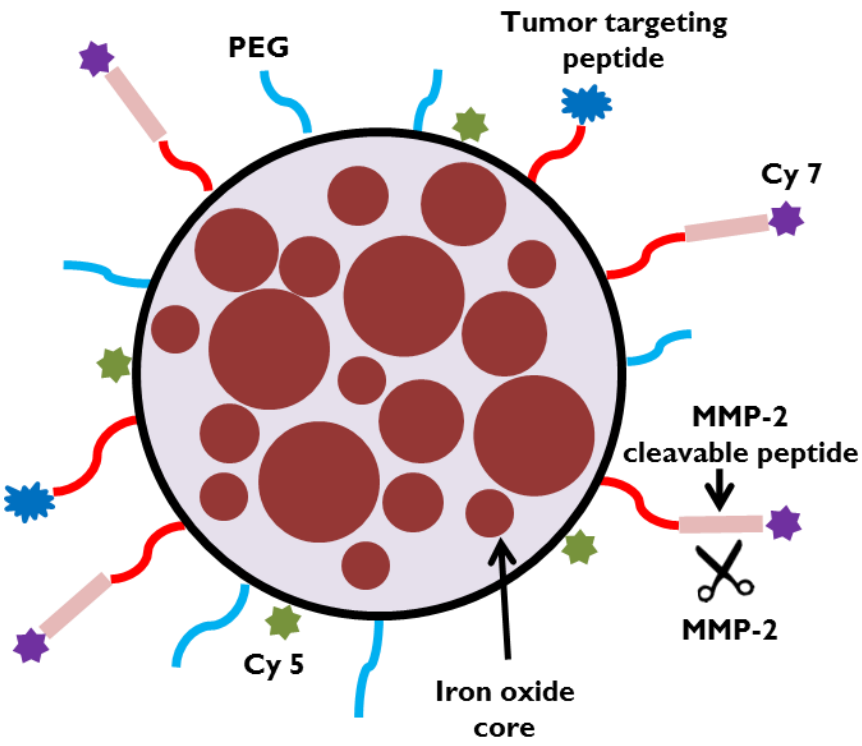

Figure 1.1 We developed a dual-fluorochrome, tumor-targeting MSOT contrast agent for imaging and quantification of MMP-2 activity in the tumor microenvironment.

Chapter 2 Background

2.1 Nanoparticle-based probes for molecular imaging of proteolytic activity

This section discusses recent advances in the development of nanoparticle-based molecular imaging probes for the detection of proteolytic activity in the tumor site.

2.1.1 Molecular imaging of tumorigenesis

Molecular imaging typically involves 2-D or 3-D imaging and quantification of a biological process over time [18]. Differential physiological characteristics (acidosis, hypoxia, increased proteolytic activity, etc.) between tumor and normal tissues can be visualized and/or quantified with molecular imaging probes for early tumor detection, risk stratification, assessment of therapeutic targets, and monitoring of therapeutic response [3,19,20].

The tumor microenvironment reflects a more acidic profile (pH 6.2-6.9) compared to normal tissue (pH 7.3-7.4) [21], which promotes pulmonary metastasis in human melanoma cells through acidity-induced up-regulation of matrix metalloproteinases (MMP-2 and MMP-9), cathepsins and proangiogenic factors (VEGF-A and IL-8) [22]. Many pH-sensitive nanoparticle systems were developed to target this acidic, "hostile" tumor microenvironment. In one example, iron oxide nanoparticles were functionalized with glycol chitosan, a pH-responsive polymer that transitions from neutral in the blood (pH 7.4) to cationic in the tumor microenvironment (pH < 7.0). Electrostatic interactions between the cationic nanoparticles and anionic components of the tumor microenvironment resulted in an increase in accumulation of the pH-responsive particles at

the tumor site, observed through enhanced contrast in T_2*-weighted MRI images compared to non-pH responsive controls [23].

Positron emission tomography (PET), magnetic resonance imaging (MRI), and optical imaging probes were developed to detect tumor hypoxia [24]. In one study, targeted luminescent near-infrared polymer nanoprobes experienced a distinctive ratiometric response to limited oxygen concentration found in tumor hypoxia [25]. However, imaging of acidosis and hypoxia requires diffusion of the imaging probe to regions typically situated far from blood vessels in the tumor's core, which are difficult to reach [20].

2.1.2 Nanoparticle-based probes for non-invasive imaging of proteolytic activity *in vivo*

Note: This section is taken directly (with minor changes) from the paper that myself, Dr. Peter Panizzi and Dr. Allan E. David published in 2016 in the journal Nanomedicine, titled 'Nanoparticle-based probes to enable noninvasive imaging of proteolytic activity for cancer diagnosis' [26]. Permission was granted through a 'license agreement between Tareq Anani and Future Medicine Ltd provided by Copyright Clearance Center'.

It is predicted that by 2030 there will be more than 22 million new cancer cases each year worldwide [27]. Successful management of cancer hinges on its early and accurate detection and subsequent treatment [28]. In many instances, both diagnosis and treatment planning rely on data gathered through biomedical imaging techniques. Conventional anatomical imaging modalities, which include magnetic resonance imaging (MRI), ultrasound and computed tomography, provide morphological information on the location and size of a tumor lesion. Anatomical imaging,

however, lacks specificity and sensitivity [29] and provides no information about abnormalities at the cellular and molecular level [30]. As a result, clinically utilized anatomical imaging techniques only detect tumors when the lesion diameter exceeds approximately 1 cm, at which point the tumor comprises more than a billion cells [31]. Molecular imaging, on the other hand, offers the potential to visualize and quantify the molecular and cellular processes associated with early stages of disease progression and its remission [3]. For example, differential physiological characteristics, which include the overexpression of several cell receptors such as epidermal growth factor receptors [18], low pH, hypoxia, and increased proteolytic activity, between tumor and normal tissues can be exploited in the development of tools for diagnosis and monitoring of disease state [3,19,20].

Imaging of tumor proteolytic activity is attractive for several reasons: protease expression can be elevated at even the early stages of tumor progression [32]; catalytic amplification provides for enhanced sensitivity [33]; the potential for improved signal-to-noise ratio through ON/OFF switching of probes by proteolytic activity; and the presence of proteases at the invasive front of tumors and at sites of angiogenesis – regions readily accessible to imaging probes [4]. Tumor progression and invasion makes significant use of proteases at the primary and metastatic sites [28]. In addition to degrading the extracellular matrix, proteases release growth factors and chemokines, which directly or indirectly affect tumor invasion, and they also activate latent proteins on the cell surface [34]. Matrix metalloproteinases (MMP), a family of extracellular, zinc-dependent enzymes involved in extracellular matrix remodeling, are of special interest as their increased activity is associated with the aggressiveness of many cancers [35,36]. Other proteases, including the lysosomal cysteine protease cathepsin B and the serine protease urokinase-type plasminogen activator, have also been implicated in tumor progression [37].

Numerous molecular probes, including those based on peptides [38,39], polymers [40,41], polymeric nanoparticles [15,42–44], protein nanoparticles [35] or inorganic nanoparticles [35,45–49], have been developed to image proteolytic activity. Recent interest in nanoparticle-based probes to quantify *in vivo* proteolytic activity is driven by attempts to overcome the limitations of small molecule probes, which tend to have poor pharmacokinetics, high background noise due to non-specific uptake by tissues and relatively poor detection limits [50]. Nanoparticles are able to overcome some of these limitations due to their size and vast surface area, which is readily functionalized with imaging agents for molecular imaging, cell targeting ligands for active targeting of the tumor site, and biocompatible surface coatings that can modulate pharmacokinetics and biodistribution [51]. Each nanoparticle has the potential to deliver numerous imaging agents, which enhances sensitivity for detection of the targeted molecular event [52]. Proper sizing of nanoparticles can also lead to preferential accumulation at tumor sites due to the enhanced permeability and retention effect [32,53]. Nanoparticles can also be designed to change size, charge and/or surface coating in response to environmental cues in order to optimize transport across the many physiological barriers encountered in vivo [20]. The various types of probes discussed in this review are summarized in **Table 2.1**. This discussion is focused on nanoprobes that provide the potential for noninvasive, spatial and temporal imaging of in vivo biological activity in tumor microenvironments [54].

Table 2.1 Summary of nanoparticle-based systems for imaging *in vivo* proteolytic activity.

Imaging modality	Target proteases	Nanoparticle type	Ref.
Magnetic Resonance Imaging (MRI)			
^{1}H MRI	MMP-2, -7, -9, -14, and legumain	SPION	47,55–58
^{19}F MRI	Legumain	^{19}F nanoparticles	59
Optical Imaging			
Pre-quenched fluorophores	MMP, cathepsin B, caspase-3, -8 and -9, matriptase, trypsin and uPA	Ferritin protein, glycol chitosan, AuNP and Au-Fe_3O_4 nanocomposites	15,17,35,60–64
Bioluminescence	Trypsin, MMP-2, and caspase-3	poly (phenylene ethynlene) nanoparticles. AuNPs, and UCNPs	65–67
Theranostic nanoparticles	MMP	AuNP and AuNR	68,69
Photoacoustic	MMP	Copper sulfide	70
Secondary Cerenkov-induced fluorescent imaging	MMP-2	AuNP	45
Multimodal Imaging			
MRI/optical	MMP	SPIONs and Gadolinium-labeled dendrimeric nanoparticles	4,12
PET/optical	MMP	^{64}Cu-radiolabeled glycol chitosan	16
CT/optical	MMP	AuNP	46

MMP: Matrix metalloproteinase; SPION: Superparamagnetic iron oxide nanoparticle; uPA: Urokinase-type plasminogen activator; AuNP: Gold nanoparticle; UCNPs: Lanthanide-doped upconversion nanoparticles; AuNR: Gold nanorods

Magnetic Resonance Imaging (MRI)

MRI is a noninvasive imaging modality that provides high spatial resolution and deep-tissue imaging [12,56]. Hydrogen protons, which are most frequently imaged in MRI because of its abundance, are normally found in the body with their spin axes randomly aligned. When exposed to a strong magnetic field, the spin axes of protons align with the applied field, which is the low energy state for the system. This alignment is then displaced by application of a radiofrequency pulse, which excites the protons to a higher energy level. Subsequent relaxation of the excited nuclei back into alignment with the applied magnetic field is characterized by a relaxation time, which varies based on tissue properties and is the means for discrimination between healthy and malignant tissues [71,72]. Contrast agents are used to improve the sensitivity and contrast of MR images by shortening either the T1 (longitudinal) or T2 (transverse) relaxation times. Standard MRI contrast agents used in the clinic are gadolinium chelates (T1) and magnetic nanoparticles (T2) [12]. Some clinical success has been achieved with magnetic nanoparticles as targetable MRI contrast agents [53]. The high magnetic susceptibility of iron oxide cores leads to noticeable enhancement of transverse (T2 and T2*) relaxivity, which is observed as a darkening of T2-weighted MR images (hypointensity) [73].

While MRI allows for whole-body imaging [56], it generally suffers from poor sensitivity for measuring molecular events [11]. Since magnetic susceptibility and r2-relaxivity depend on particle size, the growth of single iron oxide crystals into larger aggregate structures is one method that has been explored to enhance the sensitivity of T2-weighted MRI. The growth of particle size, however, can also negatively affect the pharmacokinetic properties and biodistribution of the

particles. A potential strategy to overcome this problem is to design particles that are initially stable in the blood but which then form aggregates in response to proteolytic activity. One approach utilizes two sets of complimentary, colloidally stable superparamagnetic iron oxide nanoparticles (SPIONs) that only self-assemble in response to proteolytic cleavage, as depicted in **Figure 2.1**. To accomplish this, Gallo et al. designed two families of SPIONs that undergo a bi-orthogonal, copper-free click conjugation following MMP cleavage [47]. The nanoparticles were tagged with cyclopentapeptide, a C-X-C chemokine receptor type 4 (CXCR4) targeting ligand, for enhanced targeting of metastatic tumors, an MMP 2/9 cleavable peptide (PLGMWSR), PEG for enhanced in vivo stability, and either azide or alkyne moieties. The particles were colloidally stable in the absence of MMP 2/9, but proteolytic cleavage exposed the alkyne and azide moieties, which led to a [3+2] cycloaddition reaction that crosslinked the particles and altered magnetic relaxivity. Simultaneous administration of the two SPIONs in tumor-bearing mice displayed T2 signal enhancement, which dropped significantly with inhibition of MMP.

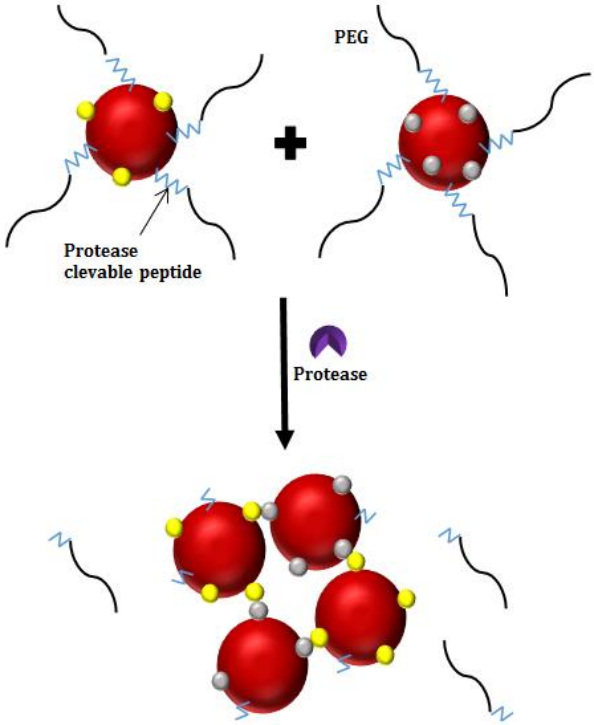

Figure 2.1 Two sets of complementary, sterically stabilized iron oxide nanoparticles aggregate (e.g. through neutravidin/biotin interactions) following proteolytic cleavage of peptide substrate and removal of polyethylene glycol (PEG). Cluster formation enhances magnetic susceptibility and r2 relaxivity to allow MRI detection of proteolytic activity.

The ability to simultaneously monitor the activity of multiple molecular targets associated with a given disease has tremendous diagnostic value. Von Maltzahn and colleagues developed a nanoprobe capable of simultaneously monitoring the activity of two matrix-metalloproteinases, MMP-2 and MMP-7 [55]. The SPIONs were designed to aggregate in response to logical 'AND' or 'OR' functions, causing an amplification of the T2 relaxation rate and enabling MRI-based detection. In the AND case, two sets of nanoparticles, one with an MMP-2 specific substrate (GPLGVRG) and biotin and the other with an MMP-7 substrate (VPLSLTM) and neutravidin, self-assembled by biotin- neutravidin interactions only if both enzymes were present. In the OR

case, two sets of nanoparticles, one having both MMP substrates in series and tethered with biotin while the other nanoparticle was tethered with only neutravidin, would self-assemble in the presence of either one or both proteases.

A significant limitation of the enzyme-activated MRI-nanoprobes discussed so far is that they require separate sets of SPIONs, which can exhibit different circulation times and biodistribution patterns in vivo. The co-delivery issue can be eliminated if a single nanoparticle is used. Schellenberger et al. designed protease-specific iron oxide nanoparticles (PSOP), which upon activation by MMP-9, switch from an electrostatically stabilized, low-relaxivity stealth state to aggregating, high-T2* relaxivity particles [56]. Initially, peptides comprising an arginine-rich coupling domain with an MMP-9-cleavable domain linked by a glycine bridge (NH2-GGPRQITAG-K(FITC)-GGGG-RRRRR-G-RRRRR-amide) were reacted with amine-reactive N-hydroxysuccinimide-methyl-PEG (NHS-mPEG). The resulting positively charged mPEG-peptide was electrostatically adsorbed onto the surface of negatively charged citrate iron oxide particles to yield PSOP. Cleavage of the peptide by MMP-9 results in the release of PEG and a loss of steric stabilization, causing aggregation due to both magnetic attraction as well as the electrostatic attraction between the positively charged arginine-rich coupling domain and the negatively charged citrate coat, as shown in **Figure 2.2**. While the probes discussed so far perform well in an in vitro setting, their in vivo application is limited by our inability to determine whether the increase in MRI contrast is due to proteolytic cleavage and subsequent aggregation of particles or if it is simply due to increased accumulation of particles at the target site, thus complicating quantitative analysis.

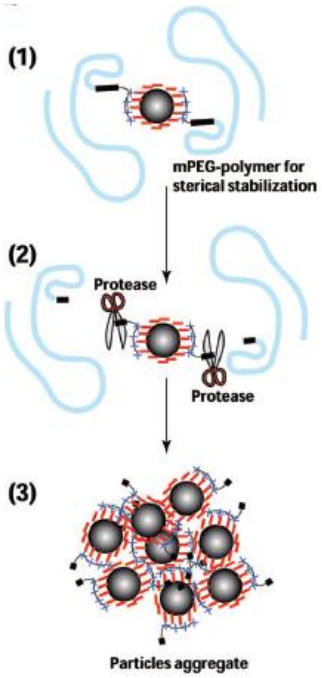

Figure 2.2 Sterically stabilized protease-specific iron oxide nanoparticles (1) release peptide-mPEG in the presence of MMP-9, which results in a loss of steric stabilization (2), causing aggregation due to both magnetic attraction of the magnetic cores as well as the electrostatic attraction between the positively charged arginine-rich coupling domain and the negatively charged citrate coat (3). Reproduced with permission from [56].

In one application, the activity of the protease legumain was utilized to tag tumor-associated macrophages (TAM) with magnetic nanoparticles. Legumain is a lysosomal/vacuolar cysteine protease that cleaves substrates at the C-terminal of asparagine, and is overexpressed in prostate, breast and colon cancers [74,75]. TAMs overexpress legumain on their surface and play an important role in the progression of certain cancers [76,77]. Yan et al. designed a Y-shaped legumain-targeting peptide (Y-Leg) with the sequence AANLHK(HK)2 and grafted it onto oxidized carbon nanotubes (OCNTs) loaded with Fe3O4 nanoparticles for in vivo targeting and MRI of TAMs [57]. T2-weighted MRI images following intravenous administration of Y-Leg-OCNT/Fe3O4 to 4T1

tumor-bearing mice revealed targeting of the nanotubes toward the TAM-infiltrated tumor microenvironment. On the other hand, control peptide-conjugated nanotubes showed no significant change in the MRI signal.

Chemotherapeutics are hindered by undesired systemic toxicity to healthy tissues. Ansari and colleagues developed an MMP-14 activatable theranostic probe (TNP) based on US FDA approved Ferumoxytol nanoparticles conjugated to an MMP-14 cleavable peptide conjugate of azademethylcolchicine, a tumor vasculature-disrupting agent, for tumor-selective therapeutic delivery [78]. The probe allowed for simultaneous MRI imaging of TNP tumor accumulation and protease-specific drug activation. MRI scans following intravenous injection to MMP-14 positive, MMTVPyMT mammary tumor-bearing mice indicated significant accumulation of the theranostic probe at the tumor site, and a significant antitumor effect and tumor necrosis, with no detectable toxicity and MRI signal in healthy tissues. It is important to note, however, that the MRI images indicated TNP delivery but not drug activation.

Due to the abundance of hydrogen protons and the scarcity of intrinsic 19F atoms in the body, 19F MRI provides better contrast-to-noise ratio than 1H MRI. Yuan et al. designed a 19F nanoparticle contrast agent which self-assembles intracellularly in the presence of glutathione (GSH) and disassembles in the presence of legumain [59]. The ‘off ’ and ‘on’ 19F NMR/MRI signal was used to detect legumain activity in HEK 293T tumor-bearing zebrafish, which showed a strong signal compared with healthy zebrafish.

Optical imaging

Optical imaging detects photons emitted by fluorescent or bioluminescent contrast agents, and can simultaneously image multiple contrast agents depending on their excitation/emission spectra. Recently, near-infrared fluorescence (NIRF) imaging has become increasingly important for visualizing important *in vivo* processes occurring at the cellular and molecular levels [79]. NIRF offers several advantages over visible-range optical imaging, including lower light scattering and lower absorption by endogenous biomolecules that strongly absorb visible (e.g. hemoglobin) and infrared light (e.g. water and lipids), leading to deeper tissue penetration [80,81]. The specificity of NIRF imaging can be substantially improved by utilizing fluorescently-quenched, peptide-based activatable probes. These probes emit little fluorescence in their native state but become highly fluorescent in the presence of a target protease [79]. The quality of a NIRF probe for imaging of *in vivo* proteolytic activity is determined by the efficiency of its quenching, its quantum yield, the target-to-background ratio, probe targeting and pharmacokinetics, protease specificity, and the probe's photostability in physiological conditions [29,64]. The following section examines the various strategies to detect proteolytic activity *in vivo* utilizing optically active nanoprobes.

Pre-quenched fluorophores

The majority of probes developed for optical imaging of in vivo proteolytic activity utilize one or more fluorescence quenching effects that include self-quenching, fluorescence resonance energy transfer (FRET), or energy transfer between dye and nanoparticle surface to reduce the pre-activation fluorescence signal. Fluorescence is recovered following the release of the quencher or dye by proteolytic activity. High quenching efficiency is essential for an effective probe.

i. FRET

FRET is a process in which an excited fluorophore (donor) transfers its excitation energy to a nearby chromophore (acceptor). The efficiency of FRET is strongly affected by the spectral overlap, dipole orientations and distance between the donor and acceptor. Separation of the two dyes causes a detectable change in signal, which is utilized to measure proteolytic activity [82]. Protease-activatable probes that employ FRET consist of a NIRF dye and quencher at both ends of a protease-specific peptide. Lin et al. developed two sets of ferritin protein cages, one with a fluorescently labeled MMP-specific peptide sequence (Cy5.5-GPLGVRGC) and another with black hole quencher (BHQ-3), that self-assemble to bring the energy donor and receptor into close proximity [35]. The ratio of donor and receptor that gave the highest fold increase in fluorescence following incubation with MMP was optimized and the probe validated following intratumoral injection in vivo against two MMP positive cell lines, UM-SCC-22B and SCC-7.

Cathepsin B (CB), which normally remains in the intracellular lysosomal compartments, is secreted into the pericellular region in high amounts as cells gain metastatic potential [83]. Ryu et al. developed CB-activatable fluorogenic nanoprobes for early detection of metastases [60]. The nanoprobe was synthesized by conjugating a CB-responsive fluorogenic peptide substrate (GRRGKGG), which included a donor (Cy5.5) and a quencher (BHQ-3), onto the surface of tumor-targeting glycol chitosan nanoparticles. The probe displayed strong specificity to CB, compared to cathepsin L, cathepsin D, and CB plus inhibitor, and was also able to discriminate metastases in liver, lung and peritoneal metastatic mouse models.

Simultaneous imaging of multiple proteolytic activities has the potential to provide a more complete map of disease progression. Park et al. developed various caspase substrate-linked

fluorescent proteins immobilized on gold nanoparticles (AuNP-FPs) for real-time simultaneous detection of multiple caspase activities in cancer cells during apoptosis [61]. AuNP served as a broad-spectrum fluorescence quencher. As shown in **Figure 2.3**, AuNP-FPs were designed to release blue-, red-, and yellow-fluorescent protein following activation by caspase-8 (IETD), caspase-9 (LEHD), and caspase-3 (DEVD), respectively, where the peptide sequence in brackets indicates the caspase cleavage site. While this is a promising approach to quantify multiple proteases, only in vitro results have been presented to date.

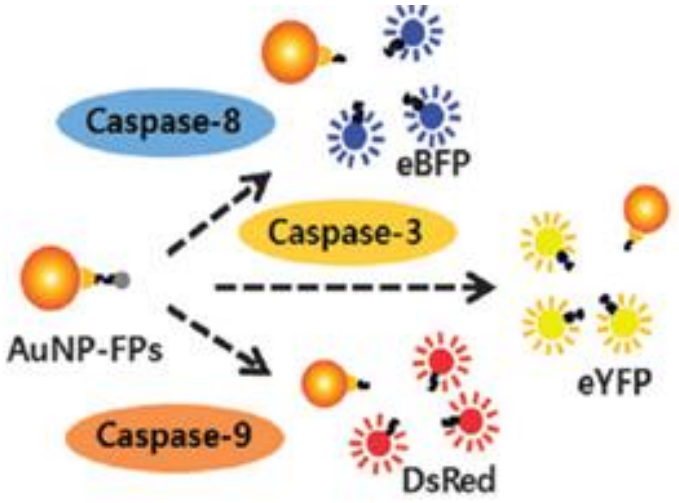

Figure 2.3 Fluorescent protein-conjugated gold nanoquenchers (AuNP-FPs) for simultaneous imaging of multiple caspase activities involved in apoptosis. AuNP-FPs were designed to release blue-, red-, and yellow-fluorescent protein following activation by caspase-8, caspase-9, and caspase-3, respectively. Reproduced with permission from [61].

ii. Quenching by gold nanoparticles (AuNPs)

Strong electronic interactions with chromophores near the surface make AuNPs very efficient quenchers of molecular excitation energy [84], with larger quenching distances (~20 nm) compared to FRET [63]. Deng et al. developed spherical and rod-shaped AuNPs for detection of in

vivo matriptase, a type II transmembrane epithelial serine protease which activates several pro-enzymes including urokinase plasminogen activator (uPA) and MMPs associated with several cancers [62]. The expression of matriptase is known to correlate with tumor staging, making it an excellent target for molecular imaging. The molecular beacon consisted of a fluorescent dye attached to AuNPs through a matriptase cleavable peptide substrate linker (GRQSRAGC). NIRF images of mice bearing matriptase-expressing HT-29 tumor xenografts showed enhanced fluorescence recovery following intratumoral injection of the molecular beacon.

The success of AuNPs that rely on the thiol-gold chemistry is hampered in an in vivo setting, due to off-target site activation in the thiol-rich blood. To overcome this limitation, flower-like Au-Fe3O4 nanocomposites with a single Au core and several Fe3O4 petals were developed as an MMP activatable fluorescence imaging probe [63]. The nanocomposite sensor, which can be tuned for shape, size, and composition, combines the robust surface chemistry of Fe3O4 for conjugation of an MMP-specific peptide-dye (Cy5.5-GPLGVRG), with the excellent quenching properties of nearby Au. The flower-like shape of Au-Fe3O4 creates an architecture whereby the fluorophores on the Fe3O4 petals are in close proximity to the Au core for efficient quenching. Separate groups of SCC-7 xenograft tumor-bearing mice received injections of flower-like activatable nanoparticles (FANP), with and without preinjection of MMP inhibitor, or gold-based activatable nanoparticles (GANPs). NIRF images for the FANP group showed high signal at the tumor site after 30 minutes, which increased gradually up to 4 hours post-injection. Pre-injection of an MMP inhibitor significantly reduced the observed signal. Meanwhile, the GANP control group showed a weak optical signal in the tumor after 4 hours (**Figure 2.4**).

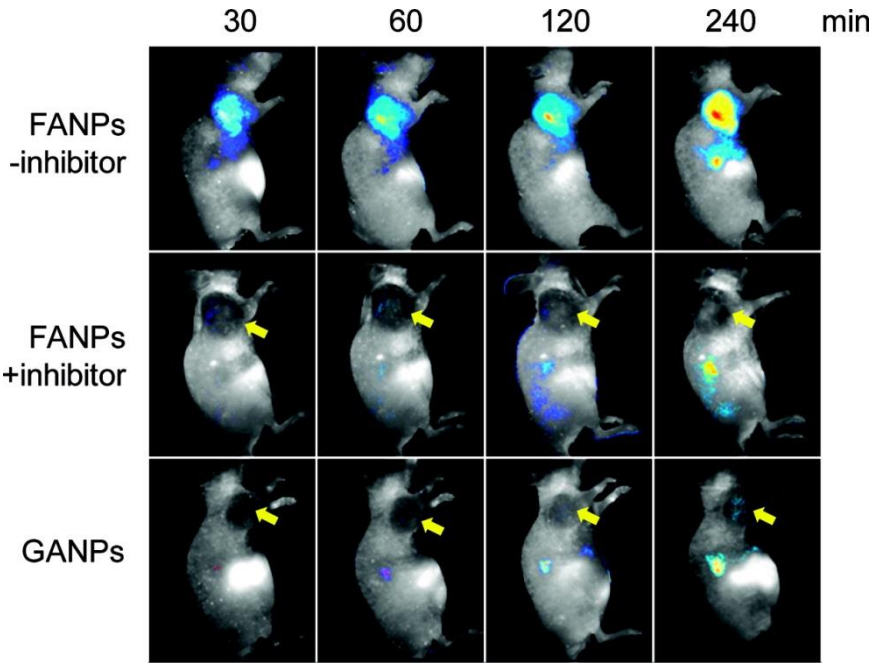

Figure 2.4 NIRF images following injection of flower-like activatable nanoparticles (FANP), FANP plus MMP inhibitor, or gold-based activatable nanoparticles (GANPs). The additional iron oxide phase incorporated into composite FANPs allowed higher loading of MMP-specific peptide-dye and better quenching properties, which resulted in higher NIRF signal in the tumor site. Reproduced with permission from [63].

iii. Combination of different quenching mechanisms

The efficiency of quenching is enhanced by combining different quenching mechanisms into a single probe. In one example, self-quenching and FRET were combined in an MMP-responsive nanosensor for NIRF imaging of MMP [15]. The nanosensor consisted of a self-assembled chitosan nanoparticle and an activatable MMP-specific peptide sequence with the NIRF dye Cy5.5 and dark quencher BHQ3 (Cy5.5-GPLGVRGK(BHQ3)-GG) to create a FRET pair. NIRF of Cy5.5 was quenched by both the interaction of the dye with BHQ-3 and dye-dye self-quenching mechanism. High recovery of Cy5.5 fluorescence signal was observed in vivo, as

evidenced by fluorescence tomography following intravenous administration of the nanosensor in an MMP-positive SCC-7 xenograft tumor and correlated with levels of active MMPs. Meanwhile, the signal was attenuated when animals were pretreated with an MMP-inhibitor. Afterward, the nanosensor was intravenously injected into mice carrying SCC-7 tumors of varying sizes, between 3.5 - 381.5 mg, to determine the nanosensor's response. After 2 hours, the animals were euthanized and the excised tumors analyzed by measuring fluorescence intensity, which was found to increase proportionally with tumor size (**Figure 2.5A**). MMP-2/9 activities were also quantified using gelatin zymography and correlated strongly with the NIRF signal intensity (**Figure 2.5B**).

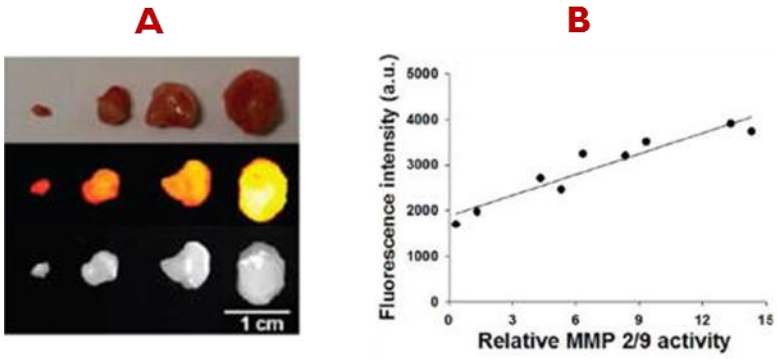

Figure 2.5 To distinguish different stages of tumors in vivo, a fluorescently-quenched, peptide-based activatable nanosensor was intravenously injected into mice carrying MMP secreting SCC-7 tumors of varying sizes. **A.** NIRF images of different sized excised tumor tissues (3.5, 66.8, 172.0, and 381.5 mg), with overall signal increasing with tumor size. **B.** Total fluorescent intensity (tumor grade) increased proportionally to MMP 2/9 activity, as measured by gelatin zymography. Reproduced with permission from [15].

Lee and colleagues developed an MMP protease-sensitive probe with AuNPs and Cy5.5 linked together through an MMP-cleavable peptide substrate (Cy5.5-GPLGVRGC-amide) [17]. The combination of AuNP surface and the close proximity of Cy5.5 induced a strong multi-quenching

effect on the fluorescence of Cy5.5. Upon exposure to MMPs, the peptide was cleaved, releasing free Cy5.5 and recovering the NIRF signal, as shown in **Figure 2.6**.

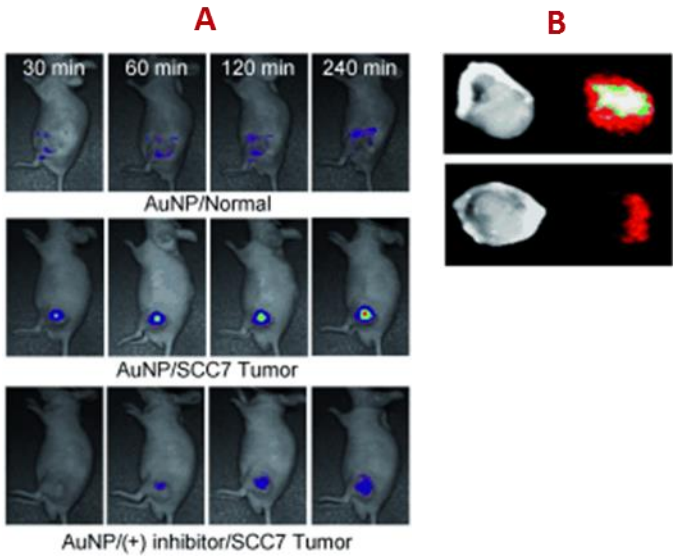

Figure 2.6 A. A series of NIRF tomographic images of normal and SCC-7 tumor-bearing athymic nude mice after intratumoral injection of an MMP-sensitive gold nanoprobe (AuNP), with and without inhibitor. Clear visualization of MMP-2 activity was evident in tumor-bearing mice. Signal diminished significantly in normal mice and in MMP-2 inhibitor-treated tumor-bearing mice. **B.** Ex vivo validation: NIRF signals of excised tumors were significantly higher (upper image) compared to inhibitor-treated tumors (lower image).Reproduced with permission from [17].

In another example, self-assembled heterogeneous monolayers of the fluorophore (Quasar 670) and a dark quencher (BHQ-2)-labeled peptide were adsorbed onto 20 nm AuNPs as an activatable probe for the detection of trypsin and uPA [64]. Fluorescence, attenuated due to self-quenching and FRET between Quasar 670 and BHQ-2, is restored following proteolytic cleavage. The probe displayed high fluorescence image contrast in a subcutaneous tumor phantom model in athymic nude mice.

Bioluminescence resonance energy transfer (BRET)

A luminescence "turn ON"-"turn OFF" system based on protease-responsive organic nanoparticles was developed and consisted of a tightly packed, semiconducting poly (phenylene ethynylene) (PPE) core bearing pentiptycene units and randomly inserted far red emissive dye (perylene) [65]. The probe also consisted of an external, hydrophilic hydrogel coating with reactive succinimide groups. Aggregation induced quenching by tuning of the π-associations in the PPE core was accomplished by reacting the succinimide groups with a protease-sensitive peptide (KCRPLALWRSK), which lead to cross-linking of the shells of the nanoparticles [strained OFF state]. Quenched luminescence was recovered upon exposure to the protease trypsin, which leads to highly fluorescent non-crosslinked nanoparticles [ON state] with a 15 fold increase in luminescence.

Bioluminescence resonance energy transfer (BRET) offers several advantages over FRET-based systems, including larger differences in the emission spectra between the BRET donor and acceptor, high sensitivity and low background emissions. Kim et al. utilized the strong quenching properties of AuNPs (BRET acceptor) to silence the bioluminescence emission of Renilla luciferase [66]. Bioluminescence was recovered in vitro following 1-hour incubation with MMP-2 and subsequent cleavage of an MMP-2 peptide linker substrate (IPVSLRSG).

Lanthanide-doped upconversion nanoparticles (UCNPs) can sequentially absorb multiple low-energy excitation photons to generate higher energy anti-Stokes luminescence [85]. UCNPs offer strong photostability, large anti-Stokes shifts, and sharp emission bandwidths. Zeng et al. developed biostable luminescence resonance energy transfer (LRET)-based UCNPs through facile peptide-mediated phase transfer to image proteolytic activity [67]. Oleic acid on the surface of

UCNPs was displaced by chimeric peptides containing a polyhistidine-tag and a caspase-3 cleavage domain (DEVD). (H)6-GDEVDAK-TAMRA –coated, caspase-3 responsive UCNPs were used to monitor the therapeutic efficacy of doxorubicin in a tumor mouse model. The upconversion luminescence (UCL) signal, which was collected between 450 and 600 nm (under 980 nm excitation), gradually increased the expression of light over a period of 12 hours in DOX-treated tumors, as opposed to saline-treated tumors.

Theranostic nanoparticles in optical imaging

Multifunctional nanoplatforms that integrate *in vivo* imaging and drug delivery into a single theranostic nanoparticle (TNP) enable simultaneous visualization of probe biodistribution, therapy and response to treatment [86]. Prodrugs, which exploit the unique characteristics of the tumor microenvironment such as overexpressed proteolytic activity or pH, could be delivered for selective treatment of cancer cells while minimizing off-target toxicity [87,88]. The addition of imaging capability enables direct monitoring of the delivery and activation of the prodrug in the tumor microenvironment [89]. In one example, doxorubicin (Dox) was conjugated to AuNPs via an MMP-2 cleavable peptide substrate (CPLGLAGG) [68]. Fluorescence of Dox was quenched by AuNPs and recovered following exposure to MMP-2. This switchable fluorescence property allowed for imaging of the activity of MMP-2 in tumor sites in vivo.

One disadvantage of incorporating both drugs and imaging agents on a nanoparticle is the competition for space, which can lead to a less than optimal surface density and reduced imaging and therapeutic efficacy. Moreover, drug incorporation adds to the cost and difficulty of synthesis and purification [86]. One alternative is to take advantage of the intrinsic therapeutic ability of several types of nanoparticles [69]. The efficient absorption of light by gold nanorods (AuNR) and the

subsequent conversion of that energy to heat make these particles good candidates for photothermal therapy [90]. Yi et al. developed a theranostic probe based on MMP sensitive gold nanorods (MMP-AuNR) for simultaneous cancer imaging and photothermal therapy, as shown in **Figure 2.7A** [90]. A Cy5.5-labeled MMP substrate (Cy5.5-GPLGVRGC) was conjugated on to the surface of AuNR, which quenched NIRF. NIRF tomographic images of SCC-7 tumor-bearing mice after intratumoral injection of MMP-AuNR with and without inhibitor were taken and significantly greater NIRF signal was observed in the case when no inhibitor was added (Figure **2.7B**). Additionally, following laser irradiation, the temperature of MMP-AuNR injected tumors increased up to 45° after 4 minutes (Figure **2.7C**), which is sufficient to damage cancer cells, and coincided with in vitro results.

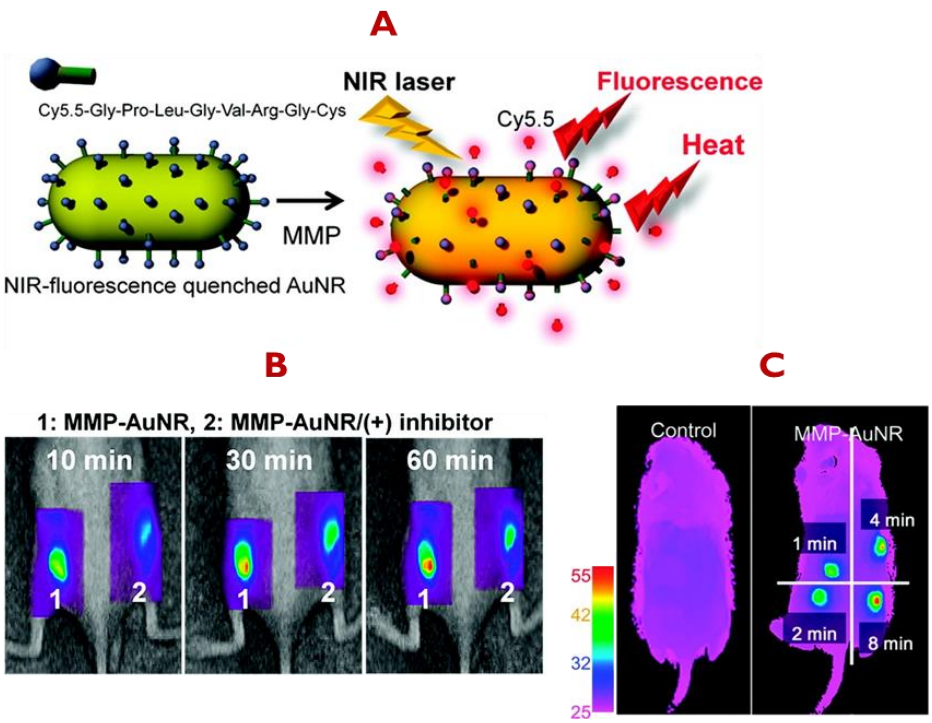

Figure 2.7 A. Schematic of a theranostic probe based on MMP sensitive gold nanorods (MMP-AuNR) for simultaneous cancer imaging and photothermal therapy. **B.** NIRF tomographic images of SCC-7 tumor-bearing mice following intratumoral injection of MMP-AuNR without (1) and with (2) inhibitor were taken, showing a significantly enhanced NIRF signal in the tumor with no inhibitor added, compared to that treated with an inhibitor. **C.** The hyperthermal therapeutic potential of MMP-AuNR was visualized through infrared thermal images of tumor-bearing mice and measured with a hypodermic thermocouple. Laser irradiation at various times was done after intratumoral injection of MMP-AuNR. The temperature increased up to 45° after 4 minutes of laser irradiation. Reproduced with permission from [69].

Photoacoustic imaging

Photoacoustic imaging (PAI) is an emerging technology that has the ability to provide structural, functional and molecular information of target tissues. PAI was developed as a means to overcome the scattering of signal from a source within an animal [91], a problem that dramatically reduces the resolution of optical imaging modalities. In general, PAI uses a focused excitation

pulse to provide energy to target probes and cause them to enter the excited state. In so doing, the probes or endogenous molecules in tissue (e.g., hemoglobin) release a heat signature in the form of thermal expansion that results in an acoustic wave, which is detected by transducers and assembled by image reconstruction analysis [92].

Recently Yang and colleagues developed an activatable photoacoustic (PA) nanoprobe which consisted of BHQ3 conjugated to 20 nm copper sulfide (CuS) nanoparticles via an MMP-cleavable peptide substrate (GPLGVRGKGG) [70]. The resulting CuS-peptide-BHQ3 (CPQ) probe displayed strong PA signals at 680 nm and 930 nm due to the strong optical absorbance of BHQ3 and CuS nanoparticles, respectively, which was used to distinguish the two components. It was hypothesized that MMP activity would disassociate BHQ3 from the CuS nanoparticles and lead to their rapid clearance from the tumor, due to their small size, while the larger CuS nanoparticles are retained. CPQ was intratumorally injected into mice bearing SCC7 tumors with and without MMP inhibitor. Ratiometric analysis of the PA signals (680/930 nm) showed MMP activity in the tumor; decreasing after 2 hours in the case with no inhibitor, but remaining almost uniform when an MMP inhibitor was pre-injected.

Other

NIRF signals obtained from in vivo lesions are a function of the intensity of incident light and the size and depth, from the surface, of the lesion. The observed signal will also depend on the proteolytic activity present in the lesion and the concentration of nanoprobe delivered, which complicates any attempt to quantify proteolytic activity in vivo [93]. A solution proposed by Scherer utilized a dual fluorochrome probe, in which polyamidoamine PAMAM-Generation 4 dendrimers were coupled to a Cy5.5 fluorophore-labeled, MMP7-cleavable peptide (RPLALWRS), to detect

proteolysis (S, sensor), and AF750 as a non-cleavable internal reference fluorophore, to monitor the total concentration (cleaved and uncleaved) of the reagent (R, reference), hence facilitating quantitative analysis [42]. The dye AF750 was also used as a quencher and its signal used to evaluate pharmacokinetics. The sensitivity of the probe was evaluated with two subcutaneous xenografted tumors on either flank of athymic nude mice that only differed in the expression of MMP7. Effective cleavage of the Cy5.5 fluorophore in the tumor was calculated by dividing the sensor signal by that of the internal reference (S/R), a ratio that corrects for differences in the lesion size and depth. S/R increased over time and was consistently greater in MMP7 expressing tumors compared to control tumor.

Many of the probes discussed so far require post-synthesis modification, which causes variability in surface charge, payload, and other characteristics. A controllable on-chip preparation of nanoprobe involved cadmium selenide quantum dot (CdSe QD) payload embedded into the hydrogel-like interior of MMP-responsive supramolecular gelatin nanoparticles (SGNs) to produce CdSe QDs encapsulated SGNs [94]. Self-assembly was done on a microfluidic device with hydrodynamic flow focusing, and the physiochemical properties were precisely controlled by changing the flow rates of the fluids. Degradation of the gelatin corona, upon exposure to MMP in the tumor, releases the QDs which can be subsequently internalized by cancer cells. In vitro cellular uptake by MMP secreting HT1080 cells was observed while the addition of an MMP inhibitor decreased the fluorescence signal.

Thorek et al. utilized energy transfer between Cerenkov luminescence-emitting radionuclide and an activatable fluorescent AuNP probe for low background, secondary Cerenkov induced fluorescent imaging (SCIFI) of MMP-2 activity [45]. The platform consisted of FAM-

labeled, MMP-2 cleavable peptide (IPVSLRSG) conjugated to AuNP, which quenched FAM fluorescence. Mice bearing SCC-7 xenografts were co-injected with [18F]-FDG radionuclides and activatable AuNP. Cleavage of the peptide by MMP-2 at the tumor site releases the fluorophore, which is then excited by nearby [18F]-FDG, leading to secondary Cerenkov-induced fluorescent conversion and detection by SCIFI.

Multimodal imaging

A growing trend in disease diagnosis is to synergistically combine several complimentary imaging modalities into a single platform, thus overcoming their individual limitations [46]. This has the potential to provide more complete information on disease pathology. Much research effort has been dedicated towards combining nanotechnology and molecular imaging to obtain a new generation of multimodal imaging nanoparticles. This section will look at the various multimodal, nanoparticle-based imaging probes developed thus far for imaging proteolytic activity in vivo.

MRI/Optical

MRI provides excellent anatomical information and great tissue penetration but it has limited sensitivity, which hampers imaging of molecular events [11]. Optical imaging, on the other hand, provides excellent molecular imaging but weak anatomical information and limited tissue penetration [12,13]. Nanoprobes that can be imaged by both of these modalities could potentially provide excellent anatomical and molecular information. Iron oxide nanoparticles, which quench fluorescence, were fabricated with a thin silica coating (PCM-CS) that contained a Cy5.5-MMP substrate (Cy5.5-GPLGVRG) for MRI/NIRF dual imaging, with molecular (MMP) activity determined through optical imaging and anatomical information through MRI [11]. PCM-CS

successful visualized the tumor regions in SC77 tumor-bearing xenografted mice using both imaging modalities. No NIRF signal was detectable in normal mice, whereas signal increased gradually in tumor-bearing mice up to 12 hours, with NIRF intensity 3-4 times higher than in normal tissue. Administration of MMP-2 inhibitor 30 minutes before injection of PCM-CS significantly reduced NIRF signal. Noticeable darkening in T2-weighted MRI images appeared at 6 hours post-injection in the tumor region as compared to the healthy muscle regions in the mice. While the decrease in MRI signal hit a maximum at 12 hours, similar to the trend exhibited in the NIRF images, it should be noted that MRI and optical imaging were conducted on different mice.

Harris et al. developed a strategy for reversibly veiling a cell internalization domain on magnetofluorescent dextran-coated iron oxide nanoparticles by shielding it with sterically protective, MMP-2 cleavable PEG (PEG-GK(TAMRA)GPLGVRGC) [4]. FITC was used to label the cell internalizing domain and thus track cellular internalization, while TAMRA- labeled peptide-PEG was used to measure MMP activity. Following administration to mice via tail-vein injection, unveiled controls cleared 8 times faster than veiled particles from the blood, and fluorescence molecular tomography and MRI showed that veiled particles accumulated to a greater extent in tumor xenografts.

A different shielding strategy was developed by Olson et al., who instead of using PEG chains, used MMP cleavable polyanionic peptides to electrostatically neutralize short, cell-penetrating polycationic domains on the surface of dendrimeric nanoparticles [12]. Following cleavage of the cleavable linker (PLGCAG) by MMP, the polyanionic domain departs from the polycation and associated nanoparticle, which are then able to penetrate cells in the immediate vicinity of the protease. Tracking of nanoparticle uptake in tumor-bearing mice by optical imaging

and T1-weighted MRI was possible by labeling the cell-penetrating peptide with Cy5, gadolinium (Gd), or both. Residual tumor and metastasis as small as 200 μm was detected with optical imaging, while GD-labeled nanoparticles deposited 30-50 μM of Gd in tumor parenchyma, which resulted in significant T1 contrast that persisted for 2-3 days after injection.

Positron emission tomography (PET)/Optical

PET provides tomographic images with excellent sensitivity and information on metabolic activities [16]. PET, unlike optical imaging, is limited in its ability to provide molecular information on proteolytic activity. As a result, combining PET imaging with optical imaging can provide vital information on tumor-targeting efficacy and proteolytic activity. Lee and co-workers prepared a PET/optical imaging probe by conjugating 64Cu radiolabeled DOTA complex and activatable MMP-sensitive probe onto azide-functionalized glycol chitosan nanoparticles via copper-free click chemistry [16]. The 64Cu-radiolabeled DOTA was used as an "always on" PET imaging agent, while the MMP- sensitive probe (Cy5.5-GPLGVRGK(BHQ-3)GG) was used as an "activatable" optical imaging agent. The activity of MMP and the biodistribution of the probe following intravenous injection were successfully measured in tumor-bearing mice by both NIRF and PET. NIRF signal could be detected in the tumor region 1 hour after injection and kept increasing until it reached a maximum value after 6 hours. Meanwhile, administration of an MMP inhibitor significantly reduced the NIRF signal. PET imaging enabled in vivo real-time visualization of tumor accumulation and biodistribution of the probe. Tumor accumulation continued to increase until it reached a plateau 24 hours post-injection.

Computed tomography (CT)/Optical

Combining both CT and NIRF functionalities onto the same probe enables the simultaneous gathering of CT anatomical images with high spatial resolution and optical images with high sensitivity [95]. It is also a cheaper alternative to MRI-fluorescence multimodal imaging [79]. Sun et al. developed a CT/optical imaging agent based on X-ray absorption and optical quenching properties AuNPs [46]. To increase the physiological stability of AuNPs, they modified the surface with biocompatible glycol chitosan (GC) polymers (GC-AuNPs). For fluorescence optical imaging of MMP activity, an MMP-specific activatable peptide probe (Cy5.5-GPLGVAGL-BHQ3) was conjugated to GC-AuNPs (MMP-GC-AuNPs), which resulted in combinatorial quenching effect of NIRF of Cy5.5 by the black hole quencher (BHQ-3) and AuNP surface. In vivo dual CT/optical imaging studies were performed with HT-29 tumor-bearing mice to confirm the specific accumulation and MMP-responsive behavior of MMP-GC-AuNPs. CT images provided anatomical information of the tumor (**Figure 2.8A**), while the NIRF signal was detected in the tumor region 1 hour after injection, and increased gradually until reaching a maximum value after 4 hours. Meanwhile, administration of an MMP inhibitor intratumorally 30 minutes before injection significantly reduced the NIRF signal (**Figure 2.8b**).

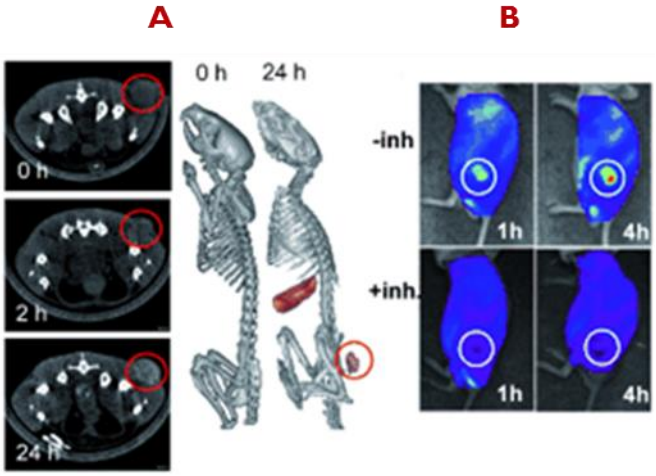

Figure 2.8. The potential of MMP-GC-AuNP as an in vivo CT/optical dual imaging agent was evaluated following intravenous injection of the probe into MMP-2 positive, HT-29 tumor-bearing mice. CT images confirmed the tumor-targeting efficacy of the probe, while the NIRF images confirmed its MMP-2-responsive. Reproduced with permission from [46].

Conclusion & future perspective

Genomics and proteomics have provided tremendous insight into the genetic, biochemical and cellular abnormalities that occur during cancer pathogenesis [30]. With this greater understanding, imaging of in vivo proteolytic activity provides the potential for early detection and staging of cancer. It is especially advantageous due to the catalytic nature of proteases, which allows for signal amplification and for the design of activatable probes with minimal background noise and enhanced contrast. To be effective, the imaging probe must display excellent pharmacokinetic properties, minimal toxicity, specific tumor targeting capability, specificity and selectivity to a target protease, and high signal to noise ratio.

Nanoparticles possess unique physical and chemical properties that can be varied for optimal tumor targeting and recognition of proteolytic activity. While small molecule probes may

be optimum for some applications, nanoprobes do offer some advantages over small molecule-based systems. Small molecule-based probes tend to be unstable and non-specifically distributing into tissue, yielding a high background noise. On the other hand, nanoparticles, with a high surface area to volume ratio, enable the incorporation of large peptide-dye payloads, which leads to enhanced target selectivity, increased sensitivity through signal amplification, and the potential for multimodal imaging of proteolytic activity, not possible with small molecule systems. Moreover, nanoparticles can also offer multifunctionality through their inherent unique optical, magnetic and therapeutic properties. However, while incorporating surface coatings, targeting ligands, imaging agents and therapeutics can yield desirable properties for diagnosis and therapy, the additional complexity could introduce challenges to large-scale production and batch-to-batch reproducibility – potentially hampering clinical translation and commercialization. This is a significant problem that hinders the production of nanoprobes, as opposed to small molecule imaging systems. Also, since even small changes in any one of the physiochemical properties (e.g. size, surface chemistry, etc.) tend to affect the pharmacokinetics, biodistribution, and toxicity of nanoprobes, these systems are inherently difficult to optimize due to the large parameter space. However, given their enormous potential in both diagnosis and therapy, significant effort in their development continues.

Several biological, physical and regulatory barriers must be overcome prior to clinical translation and commercialization of nanoparticle-based proteolytic imaging probes. Unfortunately, only a small number of probes are able to provide quantitative rather than semi-quantitative information about proteolytic activity at the target site. Semi-quantitative information, where the only signal obtained is from the activated product, can be misleading since the probe

does not accumulate uniformly throughout the body or even in the tumor volume [96]. Moreover, following activation by proteases, it is difficult to pinpoint the exact location of the probe. To overcome this issue, the concentration of both the probe and the activated product should be co-localized simultaneously and the signal ratio used to correct for lesion heterogeneity. While the dual fluorochrome probes and some of the multimodality probes discussed in this review are capable of providing quantitative information about proteolytic activity, much work remains to be done.

Another challenge in the measurement of in vivo proteolytic activity is the shielding of the peptide sequence from preactivation prior to reaching the target site. This is a difficult challenge due to the variety of proteases present in serum, which can increase the background noise. Shielding of the peptide with PEG instills a stealth property that can reduce preactivation, but can also inhibit the action of the target proteases. Advancement in nanoprobe design requires a fine balancing between the nanoparticle physiochemical properties and safety features with imaging sensitivity. The choice of protease is also very important. Proteases that are present in the tumor interstitium require extravasation and penetration of nanoparticles through the various barriers to reach the desired regions in the tumor interstitium, a slow and complex process that requires extended plasma half-life, which in turn could lead to high background noise. Moreover, fluorescent molecules tend to photobleach and destabilize over time. Proteases present in the angiogenic tumor vasculature may be an easier target as those probes don't require prolonged circulation or tissue penetration properties. Otherwise, further effort should be placed towards discovering more selective and sensitive shielding strategies and into the discovery of specific peptide substrates as these in large part determine the signal-to-noise ratio of the contrast agent.

There is also a limited understanding of the potential adverse effects of these nanoparticle-based systems, which could have drastically different toxicity profiles from their constituent components [79]. Many of the studies discussed in this review, for example, focus on enhanced tumor targeting without assessing the impact on other organs such as the liver. Obtaining a full toxicity profile, short-term and long-term, as well as nanoparticle biodistribution to critical organs and clearance is essential.

Quantification of in vivo proteolytic activity promises to tremendously increase our knowledge of disease progression, potentially also leading to improved therapies. For this to become reality, however, the specificity, selectivity, and sensitivity of probes need to be further developed, along with the computational methods necessary for data analysis. Such an effort will require a multidisciplinary effort with collaboration between engineers, chemists, biologists, physicists, and clinicians.

2.2 Multispectral optoacoustic tomography (MSOT)

Near-infrared fluorescence (NIRF) imaging is the most commonly used optical imaging modality in small animals. However, NIRF imaging suffers from weak tissue penetration due to strong light scattering, which severely limits its resolution, especially at depths exceeding a few mm. MSOT is a novel imaging modality that combines ultrasound and optical imaging for high-resolution imaging of disease state. This section discusses the most recent advancements in MSOT technology.

2.2.1 Principle of operation

Single-wavelength optoacoustic imaging systems provide limited anatomical information about disease state *in vivo* [97,98]. MSOT is an emerging optoacoustic imaging modality that uses tunable light sources, usually an optical parametric oscillator, to access multiple wavelengths and provide excellent structural, functional and molecular information. MSOT provides up to a 40-fold increase in sensitivity over single wavelength optoacoustic imaging by relying on advanced quantitative reconstruction and spectral unmixing algorithms [99].

In MSOT, a target tissue is illuminated by a pulsed laser at different wavelengths, which get absorbed by NIR absorbers [100]. A pressure wave is released at ultrasonic frequencies due to thermoelastic expansion, which gets detected by ultrasound transducers. MSOT simultaneously detects the spatial concentrations of endogenous tissue chromophores (oxyhemoglobin, deoxyhemoglobin, and melanin) and exogenous imaging agents (e.g. NIR dyes, conjugated polymers, and single-walled carbon nanotubes) through image reconstruction at different wavelengths and subsequent spectral unmixing [101–103].

MSOT contains a tomographic ultrasound array, with an imaging resolution of 20-200 µm. The spatial resolution depends on the ultrasound frequency, with 5 MHz and 30 MHz ultrasound transducers producing resolutions of ~ 150 µm and ~50 µm, respectively [98]. The sensitivity of MSOT, equal to the minimum amount of agent necessary to generate a detectable signal [104], depends on (i) volume and depth of lesion, (ii) spectral unmixing approach, (iii) number of excitation wavelengths, (iv) reconstruction algorithm for image formation, (iv) absorption coefficient of target molecule/probe, and (v) detection frequency and sensitivity of the ultrasound transducer [99,105]. The spectral unmixing algorithm has a significant impact on sensitivity and specificity [104]. In addition, increasing the number of excitation wavelengths (up to a certain limit) enhances the probability and reliability of differentiating molecules of interest from tissue background [99].

2.2.2 Biomedical applications

Optoacoustic imaging and has been used in preclinical studies to image cancer [14,102,103,106–110], arthritis [111,112], myocardial infarction [113], gastrointestinal motility [114], and monitor gene delivery [115]. In one study, MSOT was used for molecular imaging of a folate receptor positive MCF-7 breast cancer xenograft model following system administration of folate-functionalized, conjugated polymer nanoparticles (folate-CP dots). A 4-fold increase in MSOT signal was observed at the tumor site with folate-CP dots compared to control nontargeted CP dots [103]. In another study, MSOT was used to detect and monitor orthotopic S2VP10 pancreatic adenocarcinoma *in vivo* using a CF750 fluorescently-labeled Syndecan-1 ligand probe. A spike in MSOT signal confirmed preferential accumulation of Syndecan-1 probe at the tumor site compared to off-target sites (liver

and kidney). In addition, MSOT displayed significantly greater sensitivity in lesion detection over 2-D fluorescent planar imaging.

In a study conducted by Buehler et al., MSOT provided more accurate spatial information about the location of targeted tumor targeting probe compared to a molecular tomography (FMT)/small animal X-ray CT (XCT) integrated imaging system. In this case, MSOT accurately showed that the probe accumulated in the tumor vasculature, without penetrating the tumor interstitium, a result that was confirmed by *ex vivo* epi-fluorescence imaging of cryo-sliced sections. Meanwhile, FMT lacked sufficient depth resolution to differentiate between the vasculature and interstitium, and thus couldn't precisely locate the probe [102].

Fluorescence and bioluminescence imaging modalities are hampered by strong light scattering and attenuation, and thus not well-suited to characterize tumor activity in orthotopic models at depths exceeding the subcutaneous level. On the other hand, MSOT was able to detect EGFR-expressing orthotopic pancreatic tumor with high resolution following intravenous injection of an EGF-conjugated CF-750 near-infrared fluorescent probe [108].

The high spatial and temporal resolution of MSOT makes it an excellent choice for use in dynamic studies. In one example, MSOT imaging was used to characterize the biodistribution of indocyanine green (ICG) in the liver and gallbladder [116]. In another study, MSOT was used to study the effect of changing the route of administration (intravenous vs. intraperitoneal vs subcutaneous) on the biodistribution profile of NIR-loaded PEI-PLGA nanoparticles.

2.3 Superparamagnetic iron oxide nanoparticles (SPIONs)

SPIONs were used as the core nanomaterial throughout the duration of this research project. This section provides background on some common synthesis techniques, physiochemical characterization techniques, and SPION-based tumor diagnostics available in the literature.

2.3.1 SPION synthesis

Extensive synthesis protocols have been established to produce SPIONs of various shapes and sizes. Hydrolytic co-precipitation and thermal decomposition are the two most commonly used methods to produce SPIONs [117]. In hydrolytic co-precipitation, a concentrated base (e.g. NH_4OH or NaOH) is added to Fe^{2+} and Fe^{3+} salts to produce water-soluble SPIONs with relative ease and at an industrial level. However, hydrolytic co-precipitation produces highly polydispersed sizes and shapes at suboptimal crystallinity [118]. On the other hand, thermal decomposition produces SPIONs with a narrow size distribution, homogenous shape, and high crystallinity and magnetization; all highly desirable properties for biomedical applications [118].

2.3.2 Physiochemical characteristics of SPIONs: Effect on pharmacokinetics and biodistribution

i. Size

The physiochemical properties of SPIONs affect their biocompatibility, circulation half-life, biodegradability, toxicity, biodistribution and tumor targeting capabilities. Iron oxide nanoparticles are classified as (1) Ultrasmall superparamagnetic nanoparticles (USPIONs) when the size is less than 50 nm, (2) Superparamagnetic iron oxide nanoparticles (SPIONs) when the size is between 50 and 150 nm, or (3) Oral SPIONs when the size is between 300 nm and 3.5 μm

[119]. While USPIONs and SPIONs can be administered intravenously, larger sized particles can only be administered orally and therefore limited to studying the gastrointestinal tract [120].

The size of SPIONs affects its pharmacokinetics and biodistribution. Small nanoparticles (<5.5 nm) are subjected to rapid tissue extravasation and kidney clearance [121], whereas large nanoparticles (>200 nm) are rapidly opsonized and removed by phagocytic cells, especially by macrophages of the liver and spleen [120,122]. Medium-sized nanoparticles (10-100 nm) are considered pharmacokinetically optimal [53], as they are significantly better at evading opsonization compared to larger SPIONs, and are big enough to evade kidney clearance [123]. Moreover, medium-sized SPIONs can passively target solid tumors via the enhanced permeability and retention effect [124]. Solid tumors are characterized by a damaged and leaky vasculature that promotes extravasation of nanoparticles from the blood into the tumor interstitium [125], and poor lymphatic drainage that extends SPION retention [120]. On the other hand, normal vasculature consists of densely packed endothelial cells that prevent SPIONs bigger than 10 nm from passing through [119].

ii. Shape

Investigators have also studied the effect of changing the shape of SPIONs on its physicochemical properties. While the majority of SPIONs used in biomedical applications tend to be spherical, other shapes (nanostars [126], nanocubes [127], and nanorods [128]) were synthesized by altering the reaction conditions. While the shape of SPIONS affects its magnetic properties and surface composition, very conflicting results appear on its effect on stability and performance *in vivo* [19,129].

iii. Surface coating

Incorporating a hydrophilic and biocompatible coating on the surface of SPIONs generates a 'core-shell' structure for additional stability *in vivo*. Polymers are the most commonly used surface coating and are classified as homopolymers or copolymers, neutral or charged, natural or synthetic. Examples include chitosan, alginate, gelatin, polyethylene glycol (PEG), albumin and starch [130]. Polymers are incorporated during synthesis or post-synthesis through a ligand addition mechanism by hydrogen bonds and electrostatic interactions [120,131].

2.3.3 SPION toxicity

Evaluation of the toxicity of nanomaterials is a critical component of preclinical and clinical studies. Most intravenously injected SPIONs are cleared from circulation by macrophages of the liver and spleen, which are then degraded by low lysosomal pH and enzyme hydrolysis [132], releasing iron, which becomes part of the body's iron pool (hemoglobin, ferritin, and transferrin) [133,134]. Excess iron results in an imbalance in iron homeostasis and the formation of reactive oxygen species, which can cause oxidative stress, DNA mutations and tissue damage [124,135]. However, small injections of SPIONs are highly unlikely to cause toxicity issues and are considered biologically safe at concentrations up to 0.2 mg/mL [118].

2.3.4 Physiochemical characterization techniques

Several physiochemical characterization techniques are used to evaluate the size, shape, surface charge, toxicity, cellular uptake and magnetic properties of SPIONs. Common techniques include transmission electron microscopy (TEM), X-ray diffraction (XRD), and dynamic light scattering (DLS) [124]. TEM utilizes an electron beam to image the electronic densities of a specimen and provides information about the size, morphology and crystal packing of the SPION core [119].

In XRD, an X-ray beam is scattered based on the crystalline structure of the material. Several methods (e.g. Scherrer and Williamson-Hall) are used to analyze the X-ray diffraction line profiles to characterize the crystal packing, shape and size of sample [136]. DLS uses the Stokes-Einstein equation to measure the hydrodynamic radius and size distribution of spherical nanoparticles based on its Brownian motion in solution and the intensity of light scattered. DLS is also used to measure the zeta potential of a sample. Zeta potential is a measure of the surface charge of a nanoparticle sample [119] and is based on the electrical double layer surrounding each nanoparticle, due to the accumulation of ions of opposite charge in the surrounding interfacial region.

Thermogravimetric analysis (TGA) is used to determine the amount of coating material on the surface of SPIONs. In TGA, the temperature is gradually increased to decompose the surface coating, and weight loss is recorded at various temperatures [137]. Higher levels of the surface coating will lead to a higher amount of weight loss at a given temperature.

The magnetic properties of SPIONs can be studied using several devices, including super quantum interference device (SQUID) magnetometry and vibrating sample magnetometry (VSM). SPIONs display zero magnetization at zero magnetic fields, and a narrow hysteresis loop of magnetization at varying magnetic fields [119].

2.3.5 SPION-based tumor diagnostics

Single-core magnetite (Fe_3O_4) SPIONs are superparamagnetic at diameters smaller than 15 nm [138]. Multicore SPIONs larger than 15 nm exhibit superparamagnetic behavior through the controlled assembly of smaller single-core SPIONs. Superparamagnetic materials exhibit zero net magnetic moment in the absence of an external magnetic field [119]; a result of random flipping of

the dipole moments by thermal fluctuations [53,139]. Superparamagnetism minimizes self-aggregation due to permanent or remnant magnetization [140], a phenomenon that occurs in non-superparamagnetic iron oxide nanoparticles, causing rapid uptake by phagocytes, thrombosis and vessel embolism [124,139]. Moreover, SPIONs act as a single magnetic domain as opposed to the multiple magnetic domains present in large magnets, and thus experience a strong magnetic attraction, up to their saturation magnetization, to small magnetic fields [124,132]. Therefore, SPIONs are stable under physiological conditions, have favorable toxicity profiles, and experience strong magnetic attraction to small magnetic fields, making them ideal for biomedical applications.

SPIONs are often used in MRI applications [141–143]; magnetic sorting of cancer cells [144], proteins [145], fatty acids [146], heavy metal ions [147], and oil-water mixtures [148]; hyperthermia[149]; biosensing [150,151]; drug delivery [73,152,153]; enzyme immobilization [154,155]; and catalysis [156,157]. Several SPION formulations have been approved as T_2 MRI contrast agents for detecting liver lesions, including Resovist (60 nm) and Feridex (120-180 nm) [158]. The high magnetic susceptibility of the iron oxide core leads to noticeable enhancement of transverse (T_2 and T_2^*) relaxivity, i.e. shortening of T_2 of protons in areas where SPIONs accumulate [53], as seen by the darkening of T_2-weighted MR images (hypointensity) [73]**.** Cole et al. developed PEG-modified, starch coated SPIONs for imaging 9L-glioma brain tumors [159]. T_2^*-weighted, gradient echo images of the brain tumor showed sustained negative contrast for PEG-modified SPIONS compared to non-PEGylated SPIONs.

The intrinsic MRI properties of SPIONs make them an excellent choice for multimodal imaging. Multimodality overcomes the individual limitations of single imaging systems. With

proper functionalization, SPIONs have been developed for dual MRI/optical imaging [160,161], MRI/PET [162], and MRI/CT imaging [163].

Chapter 3 Synthesis and characterization of PEGylated SPIONs

3.1 Introduction

Superparamagnetic iron oxide nanoparticles (SPIONs) are the most commonly used type of magnetic nanoparticles for biomedical applications.[146] This is due to their biocompatibility, biodegradability and more favorable toxicity profiles compared to other MNPs such as nickel and cobalt. SPIONs possess unique magnetic and quantum properties; a large surface area-to-volume ratio; and simple surface chemistry for high loading of moieties [119,164].

For the probe to be effective, it must be colloidally stable to evade plasma protein adsorption and subsequent macrophage uptake. Naked SPIONs tend to irreversibly aggregate through Van der Waals interactions [120,132], which can be minimized by incorporating a hydrophilic coating (e.g. PEG). The reactive surface of SPIONs allows for further modifications with biocompatible surface coatings to improve its biocompatibility and colloidal stability *in vivo* [53,71,72,165].

To enhance the pharmacokinetic properties of the probe, 5 kDa PEG were conjugated to the surface of SPIONs. This chapter discusses the synthesis of PEGylated SPIONs from a starch-coated base SPION material; the various physiochemical characterization techniques used to measure the hydrodynamic diameter, size distribution, zeta potential, surface composition and magnetic properties of SPIONs; and the effect of PEGylation on the colloidal stability of SPIONs *in vitro*.

3.2 Materials and methods

3.2.1 Materials

100 nm starch-coated, fluidMAG-D SPIONs were purchased from Chemicell. L-ascorbic acid, barium chloride (10%), iodine solution (0.1N), potassium permanganate (5%), ammonium hydroxide (containing 28-30% ammonia), sodium hydroxide (5.0 N), dimethyl sulfoxide (DMSO), and hydrochloric acid were purchased from BDH Chemicals. Fluorescamine, ammonium acetate (ACS, 97.0%), ethanolamine and epichlorohydrin (99%) were purchased from Alfa Aesar. 5 kDa succinimidyl polyethylene glycol (mPEG-NHS) was purchased from Nanocs. Slide-A-Lyzer dialysis cassette was purchased from Thermo Scientific. MagneSphere Technology magnetic separation stands were purchased from Promega. Iron standard (1000 mg/L Fe in nitric acid) was purchased from Fluka Analytical. Neocuproine hydrochloride monohydrate (99%) was obtained from ACROS. Ferrozine iron reagent was purchased from J.T. Baker. Dulbecco's Modified Eagle's Medium (1X, DMEM) and HBSS (1X) were purchased from HyClone. Sodium phosphate dibasic heptahydrate and sodium phosphate monobasic monohydrate were purchased from Amresco.

3.2.2 Synthesis and characterization of PEGylated, cross-linked SPIONs

Crosslinking and aminating SPIONs- Starch moieties on the surface of iron oxide nanoparticles were cross-linked and aminated as described by Cole and colleagues [159]. Briefly, 2 mL of starch-coated SPIONs (35 mg Fe/mL) was mixed with 3 mL 5N NaOH and incubated at room temperature for 15 minutes. Afterward, 1.3 mL of epichlorohydrin was added dropwise to the mixture, vortexed, and incubated for 24 hours at room temperature with gentle shaking. The cross-linked, starch-coated product was dialyzed against water over 24 hours using a 10 kDa

molecular weight cut-off (MWCO) Slide-A-Lyzer dialysis cassette to remove excess, unreacted reagent. The purified product was incubated with 2 mL concentrated ammonium hydroxide (28-30 % ammonia) for 24 hours at room temperature. Aminated SPIONs were dialyzed again against water for 24 hours using a 10 kDa MWCO dialysis cassette. The final product was placed on a magnetic separator and concentrated to 35 mg Fe/mL. Successful amination was confirmed using the zeta potential test and quantitative fluorescamine assay.

PEGylating SPIONs - N-Hydroxysuccinimide (NHS) chemistry was used to conjugate 5 kDa succinimidyl polyethylene glycol NHS (mPEG-NHS) to aminated SPIONs. Briefly, 30 mg of 5 kDa mPEG-NHS (in 600 uL pH 8, 0.2M phosphate buffer and 600 uL DMSO) was added to 300 µL aminated SPIONs (30 mg Fe/mL) and incubated for 4 hours at room temperature with shaking. The PEGylated product was placed on a magnetic separator and washed four times with DI water to remove excess, unreacted mPEG-NHS. Successful PEGylation was confirmed using the zeta potential test and quantitative barium iodide tests.

The following methods were used to characterize the physiochemical properties of SPIONs throughout the synthesis procedure:

Iron Quantification Assay - The iron content of SPIONs was determined using a ferrozine-based assay developed by Riemer and colleagues [166]. Briefly, a 200 µL dilution (n=3) of SPIONs in 10 mM HCl was mixed with 200 µL of $KMnO_4$/HCl (4.5% w/v $KMnO_4$ and 1.4M HCl) and 200 µL of 50 mM NaOH, then incubated for 2 hours at 60°C. 60 µL of the iron-releasing agent (6.5mM ferrozine, 6.5mM Neocuproine, 2.5M ammonium acetate, and 1M ascorbic acid in DI-H_2O) was added to the mixture following a 10-minute cooling period and incubated at room

temperature for 30 minutes. 280 µL was then transferred to a 96 well plate, and absorbance was measured at 550 nm using SpectraMax i3 plate reader (Molecular Devices). A standard curve was generated for iron standard solutions (Fluka Analytical) between 0 and 14 µg Fe/mL at 550 nm.

Amine Quantification Assay - The amine content of SPIONs was determined using a quantitative fluorescamine assay. Briefly, 50 µL fluorescamine (3 mg/mL in DMSO) was added to 250 µL SPION samples (0.5 mg Fe/mL), incubated for 10 minutes at room temperature, and centrifuged for 24 minutes at 14,000 RPM. The fluorescence intensities of 200 µL of the supernatants were measured at 400/460 nm using a microplate reader. Standard curves were created using ethanolamine between 0 and 1.25 mM amine.

PEG Quantification Assay - The PEG content of SPIONs was determined using a quantitative barium iodide assay. 100 µL of 6M HCl was mixed with SPIONs (0.4 mg Fe/mL) and incubated for 3 hours at room temperature. 50 µL were mixed with 100 µL 1% BaCl2 and 100 µL 0.002N iodine in a 96-well plate, and absorbance measured at 535 nm. Standard curves were created using 5 kDa mPEG-NHS solutions between 0 and 0.22 mg PEG/mL.

Dynamic Light Scattering (DLS) - The hydrodynamic size (backscattering angle of 173 ºC) and zeta potential (ZP; Smoluchowski model) of SPION samples were measured by Malvern Zetasizer Nano ZS (Malvern, UK).

Super Quantum Interference Device (SQUID) Magnetometry – The magnetic moment of SPIONs was measured as a function of magnetic field (-10,000 to +10,000 Oe) using SQUID

magnetometry with a Physical Property Measurement System (Quantum Design) operating at room temperature.

3.2.3 In vitro RES resistance simulations

SPION size stability in RAW 264.7 cell culture medium – Starch-coated and PEGylated SPIONs were mixed with RAW 264.7 cell culture medium (DMEM + 10% FBS + 1% antibiotics) at a concentration of 0.05 mg Fe/mL, then placed inside a cell culture incubator (37 ºC, 5% CO_2) for 22 hours. At set time points, particle size was measured using DLS.

Protein binding study in 60% FBS – 100 µL of starch-coated or PEGylated SPIONs (1.5 mg Fe/mL; n=3) were mixed with 100 µL 1X PBS buffer (pH 7.4) and 300 µL fetal bovine serum (FBS). A mixture of 100 µL SPIONs and 400 µL 1X PBS was used as a negative control. All mixtures were incubated for 2 hours at 37 ºC, centrifuged at 10,600x g, and washed four times with PBS. After the last wash, SPIONs were dispersed in 300 µL PBS, mixed with 300 µL of bicinchoninic acid (BCA) working reagent, and incubated for 2 hours at 60 ºC. Samples were centrifuged at 7,400x g for 15 minutes, and the absorbance of 230 µL of the supernatants measured at 562 nm. A standard curve was generated with bovine serum albumin (BSA) solutions.

RAW 264.7 macrophage cell uptake – RAW 264.7 macrophage cells were cultured in 100 mm dishes containing cell culture media (89% DMEM, 10% FBS and 1% antibiotics) in a cell incubator (37 ºC, 5% CO_2) until they reached ~80% confluency. Cells were harvested by scraping and seeded at $4*10^5$ cells/well (2 mL) in a 6-well plate. Plates were incubated for 24 hours to allow cells to reach ~80% confluency, then washed 3 times with HBSS. 2 mL of SPIONs (0.05 mg Fe/mL, n=3) in complete culture media were added and allowed to incubate for 15 minutes. The

same experiment was repeated at different incubation times (2 hours, 4 hours, and 24 hours). Blank media (without SPIONs) was used as a negative control. Afterward, wells were washed 3 times with 1X PBS, and quantitative iron-quantifying ferrozine assay was conducted similarly to what was described in **section 3.2.2**. The only difference was that 300 µL of 10 mM HCl, 50 mM NaOH and KMnO4/HCl were used instead of 200 µL.

3.2.4 Statistical analysis

The hydrodynamic diameter and PDI values are reported as the mean ± coefficient of variation. All other values are reported as the mean ± standard deviation (n=3).

3.3 Results and discussion

3.3.1 Synthesis and characterization of PEGylated, cross-linked SPIONs

Starch-coated SPIONs were used as the base nanomaterial for several reasons. SPIONs have a favorable toxicity profile and were previously approved by the FDA as an MRI contrast agent [167]. In addition, the biocompatible starch coating provides ample hydroxyl groups for additional surface modifications. In this case, starch moieties were initially cross-linked with epichlorohydrin for additional chemical stabilization, then aminated with ammonium hydroxide. NHS chemistry was then used to conjugate 5 kDa m-PEG-NHS polymer to the surface of aminated SPIONs (**Figure 3.1**).

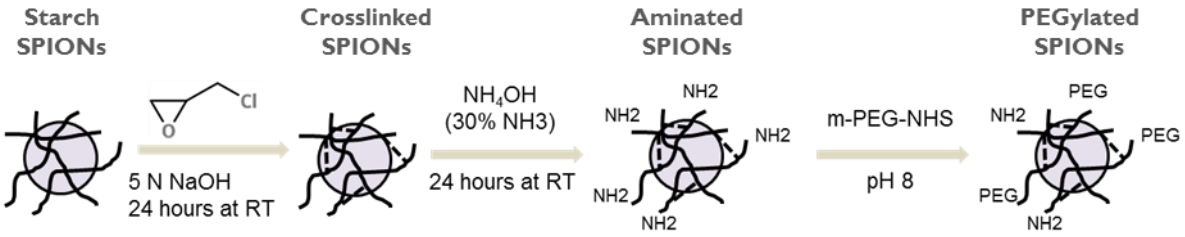

Figure 3.1 Synthesis of PEGylated SPIONs from starch-coated SPIONs.

Various physiochemical characterization techniques were used to test the size, surface charge, surface coverage, morphology, and magnetic properties of SPIONs throughout the surface modification process. The quantitative fluorescamine and barium iodide assays confirmed successful amination and PEGylation of SPIONs, respectively (**Table 3.1**). DLS was used to measure the zeta potential (ZP), hydrodynamic diameter, and polydispersity index (PDI) of starch-coated, aminated and PEGylated SPIONs (**Table 3.1**). ZP measurements (**Figure 3.2A**), which reflect the surface charge of particles [119], confirmed successful amination (shift towards positive

ZP) and PEGylation (shift towards neutral ZP). The hydrodynamic diameter increased from 98.2 ± 25.0 nm (starch-coated) to 131.2 ± 34.1 nm (aminated) to 136.4 ± 33.8 nm (PEGylated) nm. The PDI values were low (< 0.13) for all three configurations; suggesting that SPIONs remained mono-modally distributed throughout the surface modification process.

Table 3.1 Characterization of size, zeta potential, amine content, and PEG content throughout the surface modification process.

SPION	Hydrodynamic diameter (nm)	PDI	Zeta potential (mV)	[NH2] nmol amine/mg Fe	[PEG] nmol PEG/mg Fe
Starch	98.2 ± 25.0	0.097	-11.3 ± 6.89	–	–
Aminated	131.2 ± 34.1	0.116	16.7 ± 7.29	684.9 ± 178.7	–
PEGylated	136.4 ± 33.8	0.125	3.96 ± 3.28	584.9 ± 164.3	180.2 ± 26.1

Finally, SQUID magnetometry was used to measure the magnetic properties of starch-coated and PEGylated SPIONs. Magnetization hysteresis loops, which plot the magnetic moment as a function of magnetic field, are shown in **Figure 3.2B**. Both curves displayed reversible hysteresis behavior and zero coercivity, which ensured that the superparamagnetic properties of SPIONs remained intact during the surface modification process. In addition, both SPIONs had similar saturation magnetization values (~16.8 emu/g Fe).

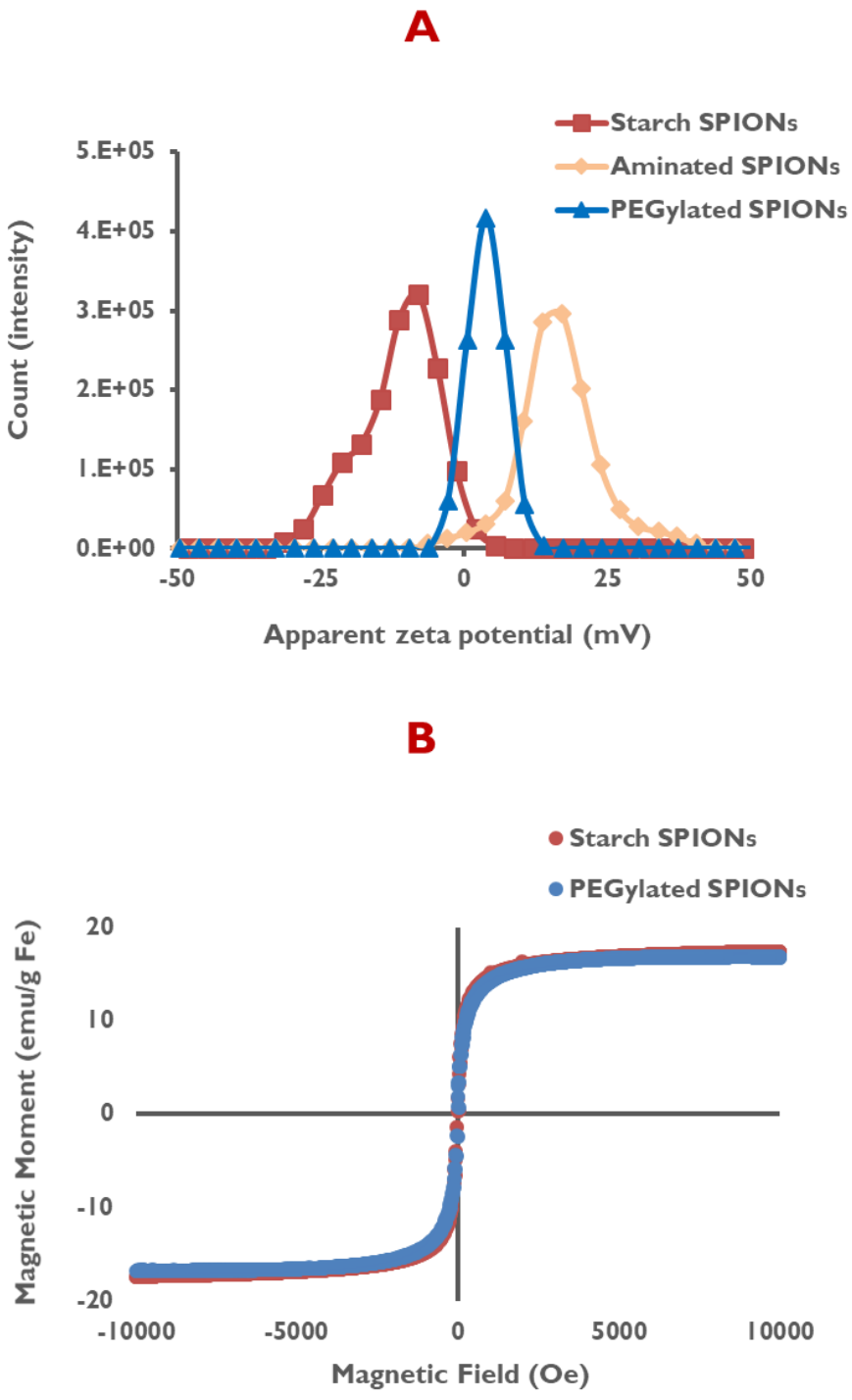

Figure 3.2 A. Zeta potential curves for starch, aminated and PEGylated SPIONs. **B.** Magnetization hysteresis loops of starch-coated and PEGylated SPIONs measured using SQUID magnetometry.

3.3.2 *In vitro* RES resistance simulations

The primary mechanism by which SPIONs are cleared from circulation involves the reticuloendothelial system (RES). Circulating plasma opsonin proteins adsorb onto the surface of SPIONs, which triggers subsequent uptake by macrophages of the RES and removal from circulation. *In vitro* RES resistance simulations and size stability studies were conducted to validate the enhanced pharmacokinetic properties of PEGylated SPIONs versus the starting material.

The rate of clearance depends primarily on the aggregation behavior of SPIONs while in circulation, which can be mimicked by measuring the size stability of SPIONs in complete culture. PEGylated SPIONs demonstrated significantly higher size stability compared to starch-coated SPIONs, which experienced a 207-nm increase in hydrodynamic diameter after 1.5 hours (**Figure 3.3A**).

In addition, PEGylation reduced protein adsorption (**Figure 3.3B**), and macrophage uptake (**Figure 3.3C**) of SPIONs significantly. The rate of opsonization and macrophage uptake is strongly dependent on the material's size, surface charge, and hydrophobicity. Addition of a hydrophilic, electrostatically neutral PEG polymer provided a "stealth" property through steric hindrance to opsonization and macrophage uptake [139]. This property is very useful in tumor targeting and drug delivery applications: By prolonging circulation, SPIONs have a greater opportunity to passively target the compromised, leaky tumor vasculature through the enhanced permeability and retention effect.

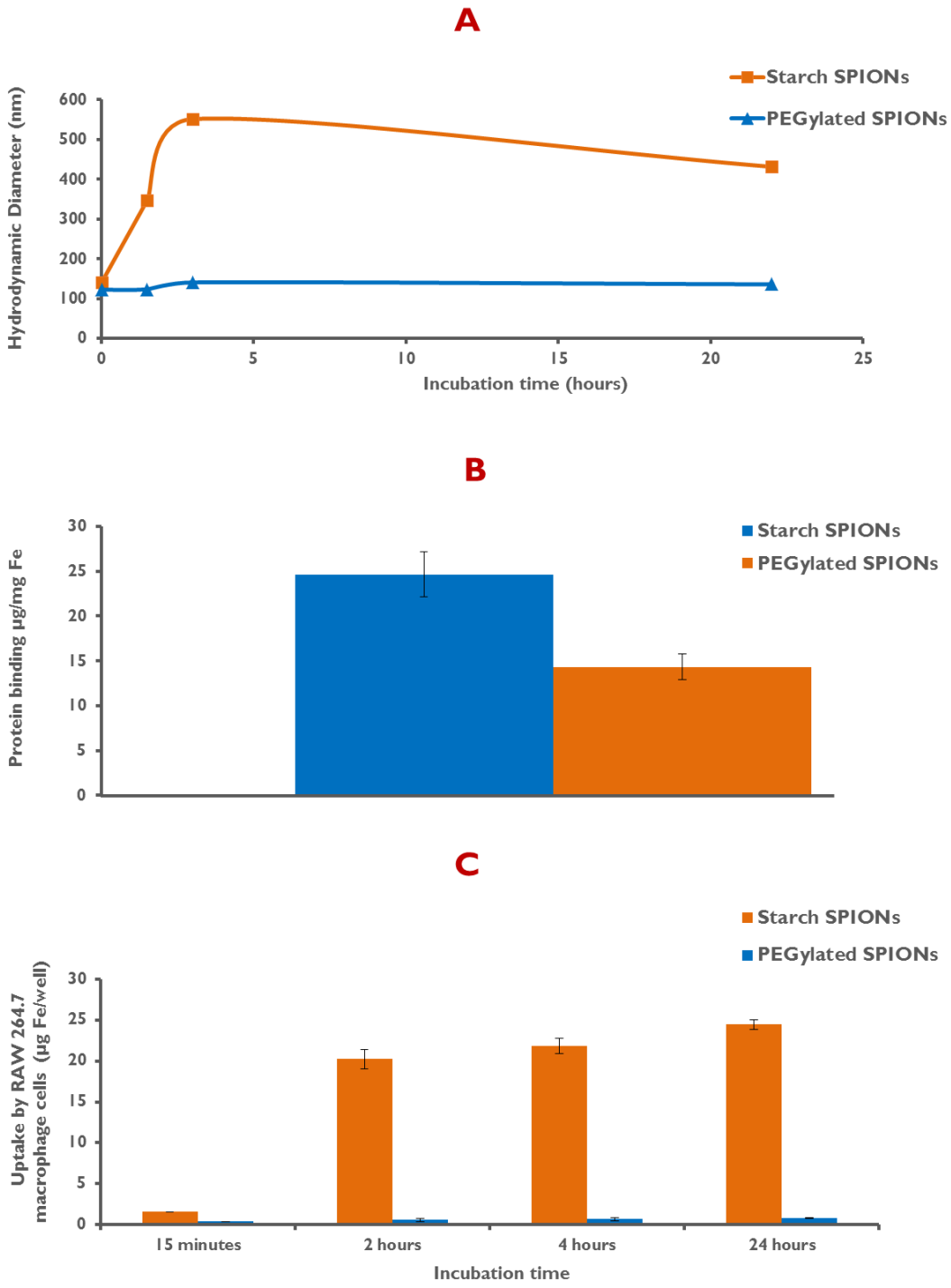

Figure 3.3 RES simulations to study the effect of PEGylation on size stability, protein binding and macrophage uptake of SPIONs. **A.** Size stability in RAW 264.7 cell culture medium. **B.** Protein binding in 60% FBS. **C.** Uptake by RAW 264.7 macrophages.

3.4 Conclusion

In this chapter, we demonstrated the ability to generate PEGylated SPIONs from starting starch-coated SPIONs; introduced the various characterization techniques that will be discussed throughout this work; and performed *in vitro* RES simulation tests to study the effect of PEGylation on colloidal stability. The fluorescamine assay, barium iodide assay and zeta potential test confirmed successful amination and PEGylation of SPIONs. The PDI values remained under 0.15 throughout the surface modification process; suggesting that the PEGylated nanoparticles had a monodispersed size distribution. Finally, magnetization hysteresis loops indicated that the superparamagnetic property of SPIONs was preserved throughout the surface modification process.

Next, the main steps involved in the reticuloendothelial clearance process of SPIONs from circulation were simulated *in vitro*. PEGylated SPIONs had significantly higher size stability in physiological media, lower protein adsorption, and lower uptake by RAW 264.7 macrophage cells *in vitro*.

Chapter 4 Development of dual fluorochrome SPIONs

4.1 Introduction

Several nanoparticle-based probes have been developed for the imaging of proteolytic activity *in vivo* (**Section 2.1.2**). Most are fluorescently-quenched activatable probes that rely on fluorescence recovery following proteolytic cleavage. However, imaging of single fluorochrome nanoprobes provides semi-quantitative rather than true quantitative information. **Figure 4.1A** illustrates how semi-quantitative, near-infrared fluorescence (NIRF) imaging of proteolytic activity can be misleading. In one scenario (cases 4&5), a negligible fluorescence signal is generated in both tumor microenvironments despite having drastically different proteolytic activities. In this case, it is virtually impossible to tell whether the negligible signal is due to negligible nanoparticle penetration (case 4) or negligible proteolytic activity (case 5) at the tumor site. Case 4 provides false negative information and is a clear limitation of fluorescently-quenched activatable probes. In another scenario, different fluorescence signals are generated for identical proteolytic activities (cases 1, 3 &4). To overcome this limitation, several multimodal imaging probes, including dual MRI/NIRF and CT/NIRF probes, have been developed for quantitative imaging of proteolytic activity [12,16,46] (**section 2.1.2**). In this case, one imaging modality is used to track the location of the nanoparticles, while the other imaging modality is used to track proteolytic activity. However, multimodal imaging suffers from the complexity and inefficiency of co-registering data from different imaging systems [168]. Therefore, there is a need to develop a protease-sensitive probe that (i) provides true quantitative assessment of proteolytic activity at the

target site and (ii) can be imaged by a single modality with similar contrast enhancement and improved resolution over NIRF.

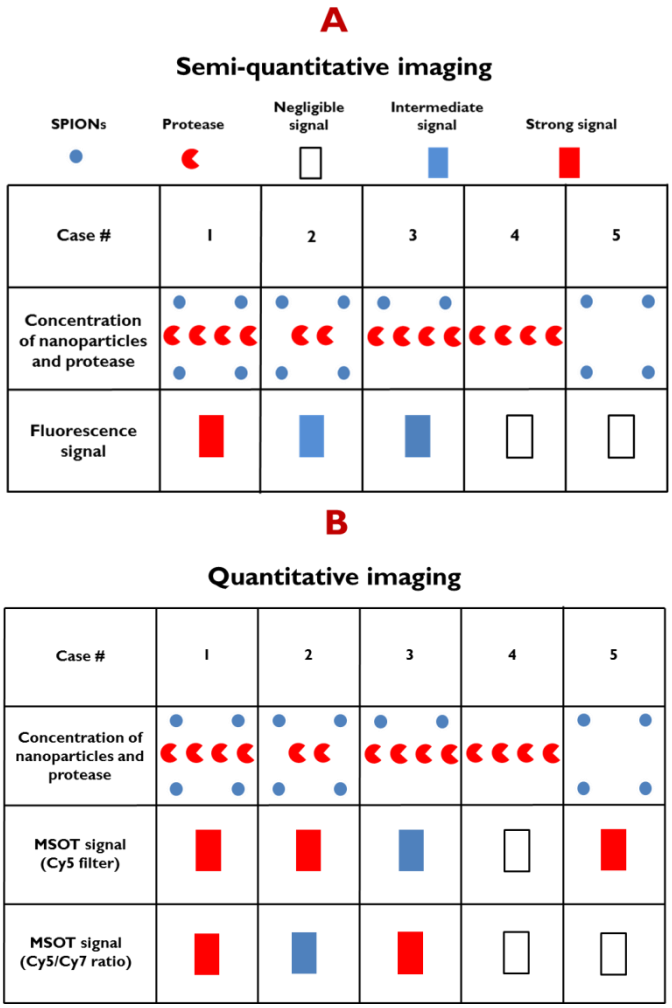

Figure 4.1 An illustration of **A.** semi-quantitative imaging of proteolytic activity using fluorescently-quenched, peptide-based activatable probes; and B. Quantitative MSOT imaging using dual fluorochrome SPIONs.

This chapter discusses the development of dual fluorochrome Cy5-Cy7-SPIONs as a multispectral optoacoustic tomography (MSOT) contrast agent. In this highly innovative approach, MSOT would quantify the concentration of SPIONs delivered to any given point in the tumor

region (through the Cy5 images), serving as a baseline, while also quantifying the rate of Cy7 release from SPIONs (through the Cy7 images). Taken together, the ratio of Cy5 over Cy7 signal is expected to increase rapidly in MMP-2 rich environments, and slowly in MMP-2 depleted environments (**Figure 4.2**), thus providing true quantitative information about the proteolytic activity (**Figure 4.1B**).

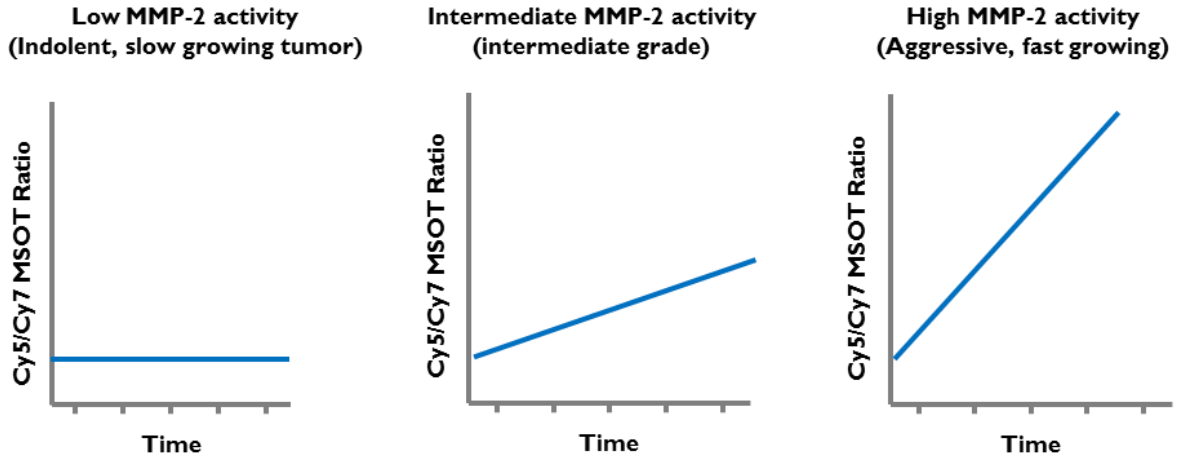

Figure 4.2 Conceptual representation of the response of dual fluorochrome SPIONs and the corresponding Cy5/Cy7 MSOT signal ratio to varying MMP-2 activity found in indolent (left), intermediate (middle), and aggressive (right) tumors.

4.2 Materials and methods

4.2.1 Materials

100 nm starch-coated, fluidMAG-D superparamagnetic iron oxide nanoparticles (SPIONs) were purchased from Chemicell GmbH. Sulfo-Cy5-NHS ester and sulfo Cy7-NHS ester were purchased from Lumiprobe. 20% intralipid was purchased from Sigma. Granulated agar was purchased from Difco^{TM}. Sodium phosphate dibasic heptahydrate and sodium phosphate monobasic monohydrate (phosphate buffer components) were purchased from Amresco.

4.2.2 Absorption spectra of Cy5 and Cy7

The absorption spectra of sulfo-Cy5-NHS and sulfo-Cy7-NHS dyes were measured using a microplate reader. Serial dilutions of each dye were made between 0 to 25 μg/mL (n=2), and absorbance was measured from 300-950 nm with an interval of 10 nm.

4.2.3 Synthesis of dual fluorochrome SPIONs

17 μL of sulfo Cy5 NHS ester (10 mg/mL in H_2O) and 250 μL aminated SPIONs (6.54 mg Fe/mL in 0.1M, pH 8 phosphate buffer) were mixed together, incubated for 1 hour at room temperature while being protected from light, placed on a magnetic separator, washed three times with fresh pH 8 0.1M phosphate buffer to remove unbound Cy5, and labeled Cy5-SPIONs. Cy5-SPIONs were divided into three equal portions, and various volumes of Cy7 (10 mg/mL in H_2O) were added to each solution (**Table 4.1**). All three mixtures were incubated overnight and then placed on a magnetic separator to remove excess, unbound Cy7. The washing process was repeated three times until no more Cy7 was detected in the supernatant.

Table 4.1 Generating Cy5-SPIONs, Cy5-lowCy7-SPIONs and Cy5-highCy7-SPIONs.

Label	Volume (µL) of sulfo Cy7 NHS (10 mg/mL) added to Cy5-SPION
Cy5-SPIONs	0
Cy5-lowCy7-SPIONs	3
Cy5-highCy7-SPIONs	25

4.2.4 Absorption spectra of dual fluorochrome SPIONs

The absorption spectra (400-900 nm) of Cy5-SPIONs, Cy5-lowCy7-SPIONs, and Cy5-highCy7-SPIONs were measured at 0, 1, 3, and 6 days.

4.2.5 MSOT phantom preparation

A tissue-mimicking scattering agar phantom (2 cm in diameter) made of 1.5% agar and 1% intralipid was prepared. The phantom's dimensions were controlled by pouring the gel solution (at ~100 ºC) into a 20-mL syringe with an internal diameter of 2 cm at room temperature until the gel polymerized. Two cylindrical channels (3 mm diameter) were then made by inserting two cylindrical straws (3 mm OD) into two separate positions.

4.2.6 MSOT imaging system

Optoacoustic imaging of phantom gels was done using an MSOT inVision 256-TF imaging system (iThera Medical, Munich, Germany). The system uses a pulsed optical parametric oscillator (OPO) powered by an Nd:YAG solid state laser to deliver last pulses (10 ns duration) between 680-980 nm. A static fiber bundle with 10 arms is used to homogeneously illuminate the object. The 256-TF imaging system contains a 256-element, 270º tomographic array of piezocomposite

(5MHz) ultrasound transducers that detect ultrasound signals and provide a 150 μm resolution. Measurements were taken in a temperature controlled water bath at 34 ºC. Water, with its tissue-like speed of sound, is used as the coupling medium between the phantom holder and the ultrasound detector.

4.2.7 MSOT phantom studies to quantify the optoacoustic properties of SPIONs

The optoacoustic properties of Cy5-SPIONs, Cy5-lowCy7-SPIONs, and Cy5-highCy7-SPIONs were measured by placing two 3-mm straws containing 200 μL of solution (one sample and one control) into the two channels within the phantom gel. The absorption spectra of Cy5, Cy7, aminated-SPIONs, and Cy5-SPIONs were inputted into the MSOT software prior to imaging. Ten averages (laser pulses) were acquired at 680, 700, 730, 750, 800, 850 and 900 nm. It was mathematically crucial to select a number of wavelengths that was equal to or greater than the number of spectra selected. Imaging was repeated for different SPION concentrations (0.185, 0.08, 0.04, 0.02, 0.01 and 0.005 mg Fe/mL).

Data were processed by the iThera Medicals MSOT software. Images were reconstructed using a back-projection algorithm, while multispectral processing was done using linear regression. The absorption spectra of the individual absorbers were fit, based on least-squares linear regression, to the pixel intensities at different wavelengths. The result was component images for each one of the selected absorbers. Two regions of interest (ROI) were drawn around the sample and control, and MSOT signal quantified with the ViewMSOT software.

4.3 Results and discussion

4.3.1 Synthesis and characterization of dual fluorochrome probe

MSOT imaging relies on the strong absorption of near-infrared (NIR) light by endogenous and exogenous molecules in the 680-900 nm range. Unmodified SPIONs have weak absorption properties in the NIR range. To solve this problem, the NIR and water-soluble dyes sulfo-Cy5 and sulfo-Cy7 were conjugated to the surface of aminated SPIONs through NHS chemistry. The absorption spectra of sulfo-Cy5 and sulfo-Cy7 were measured between 300 and 900 nm (**Figure 4.3A).** Both dyes have distinctive absorption spectra, with maximum absorption occurring at 650 and 750 nm for sulfo-Cy5 and sulfo-Cy7, respectively. Standard curves were then created by measuring the absorption of different concentrations of sulfo-Cy5 and sulfo-Cy7 at 650 and 750 nm (**Figure 4.3B**). It is worth noting that while sulfo-Cy5 has a negligible absorbance at the $Abs_{max,750\ nm}$ of sulfo-Cy7, sulfo-Cy7 does absorb moderately at the $Abs_{max,650\ nm}$ of sulfo-Cy5.

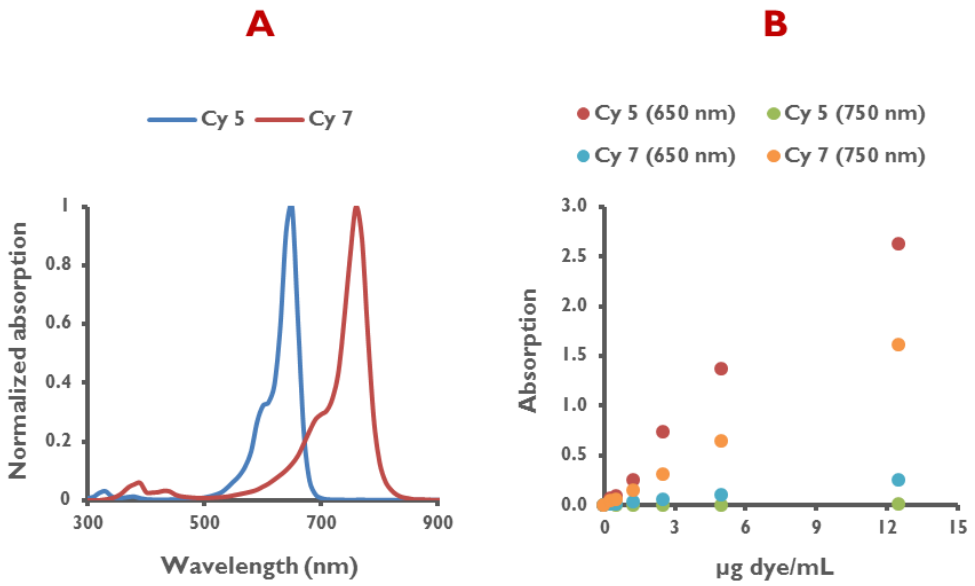

Figure 4.3 Absorption properties of sulfo-Cy5 NHS and sulfo-Cy7 NHS. **A.** Absorption spectra of both dyes. **B.** Standard curves at 650 and 750 nm.

Cy5-SPIONs, Cy5-lowCy7-SPIONs, and Cy5-highCy7-SPIONs were synthesized by conjugating Cy5 and varying amounts of Cy7 to aminated SPIONs. The reaction mechanism is shown in **Figure 4.4A**. The step-by-step process of measuring µg Cy7/µg Fe and µg Cy5/µg Fe for all three configurations is explained in detail in **Figure 4.4B**, and the results are shown in **Table 4.2**.

Table 4.2 Quantifying Cy7 concentration for different SPION structures.

Label	µg Cy5/µg Fe	µg Cy7/µg Fe
Cy5-SPIONs	0.045	–
Cy5-lowCy7-SPIONs	0.045	0.07 ± 0.04
Cy5-highCy7-SPIONs	0.045	0.14 ± 0.03

The absorption spectra of aminated SPIONs and the three dye-conjugated SPIONs are plotted in **Figure 4.5A**. As expected, the single fluorochrome probe Cy5-SPIONs had a single peak around 650 nm, while the dual fluorochrome probes Cy5-lowCy7-SPIONs and Cy5-highCy7-SPIONs had two-peak curves at 650 and 750 nm.

Another important criterion for MSOT contrast agents is their photostability over time. The absorption spectra of dye-conjugated SPIONs were measured over a period of 6 days and remained relatively constant over time (**Figure 4.5B**). The developed probes remain strong absorbers of NIR light over an extended period of time.

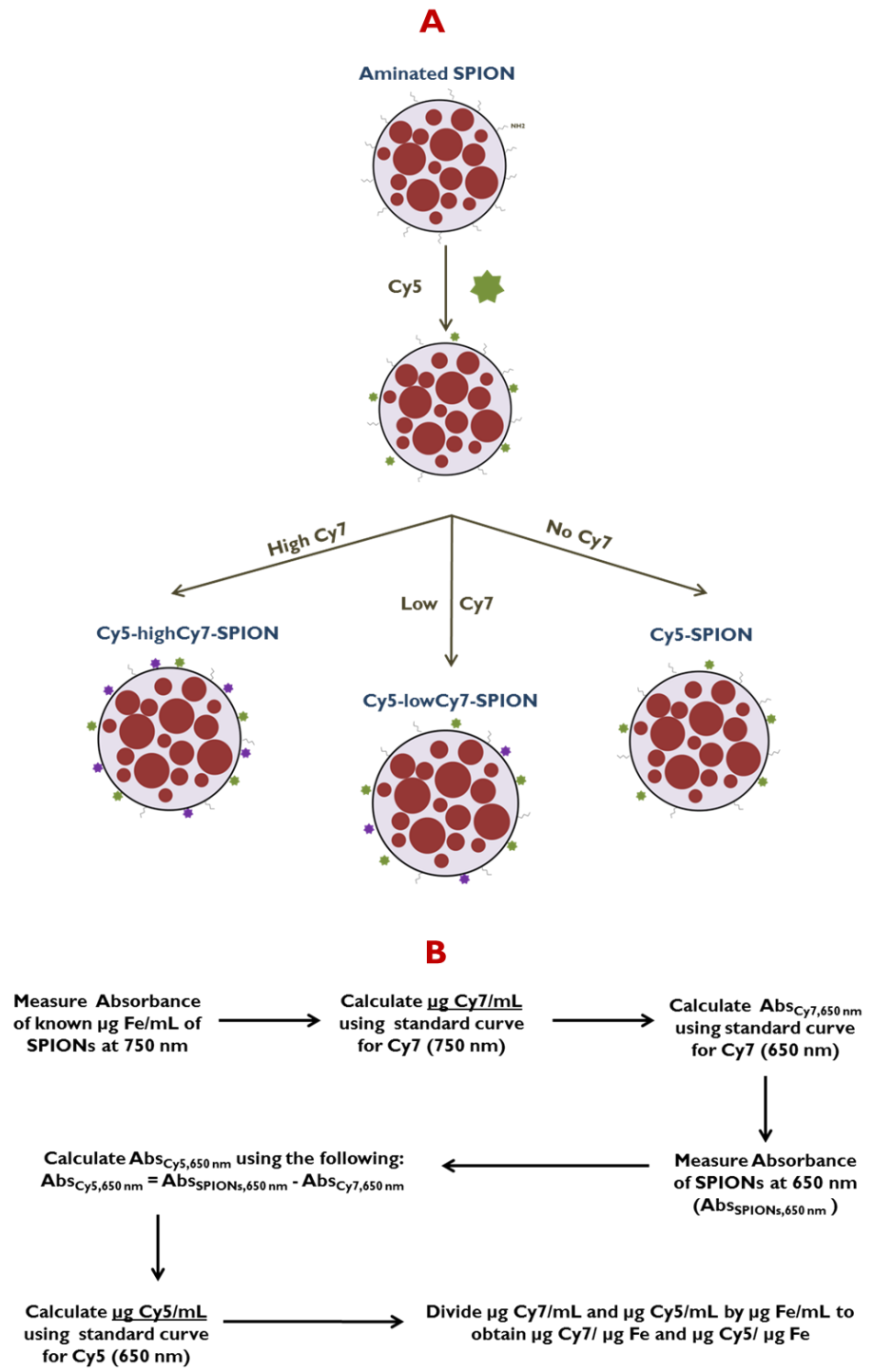

Figure 4.4 A. Reaction scheme of synthesizing Cy5-SPIONs with varying concentrations of Cy7. **B.** Step by step process for calculating µg Cy7/µg Fe and µg Cy5/µg Fe on the surface of SPIONs.

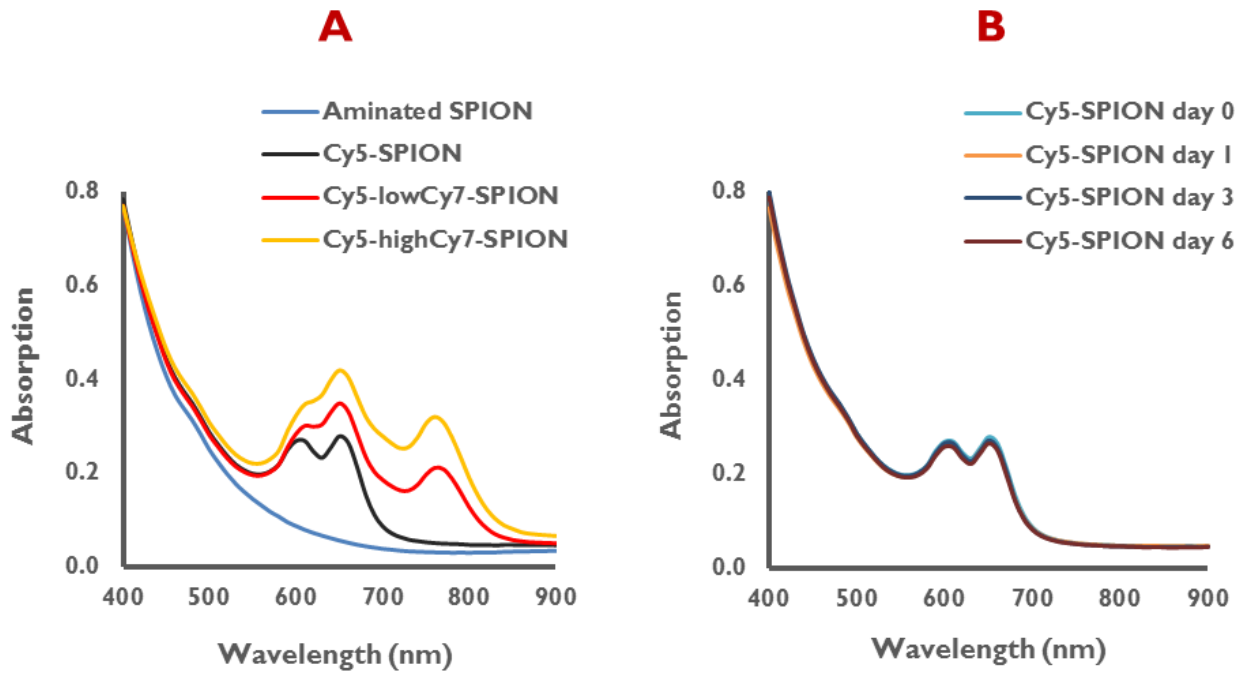

Figure 4.5 A. Absorption spectra of dye-conjugated SPIONs. **B.** Over a period of 6 days

4.3.2 MSOT phantom studies to quantify the optoacoustic properties of SPIONs

The next goal was to measure the optoacoustic properties of the dye-conjugated SPIONs. MSOT was chosen as the imaging modality due to its high spatial and temporal resolution and deeper penetration depths compared to NIRF imaging. The following questions were investigated:

A. Do the optoacoustic properties of dye-conjugated SPIONs correlate with their optical absorption properties?

B. Does the optoacoustic signal exhibit a linear relationship with probe concentration at different wavelengths?

C. Is MSOT able to spectrally unmix the contributions of Cy5-SPIONs and Cy7 for dual fluorochrome Cy5-highCy7-SPIONs? Also, does the signal ratio of 'Cy5-SPION over Cy7' remain constant at different probe concentrations?

D. Does the signal ratio of 'Cy5-SPION over Cy7' increase with increasing Cy7 surface densities (i.e. comparing Cy5-highCy7-SPION, Cy5-lowCy7-SPION, and Cy5-SPION)?

To answer those questions, a tissue-mimicking scattering agar phantom gel was prepared with two cylindrical inserts (for sample and control). MSOT imaging of the phantom gel was performed at different wavelengths between 680 and 900 nm, and images were reconstructed with a back-projection algorithm. **Figure 4.6A** shows cross-sectional MSOT images for Cy5-highCy7-SPION at different wavelengths. A region of interest (ROI) was drawn around both cylindrical channels, and signal quantified using the ViewMSOT software, which was corrected by subtracting the signal from the control channel. **Figure 4.6B** shows the normalized optoacoustic and absorption spectra side by side, which appear very similar in shape (answers **Question A).**

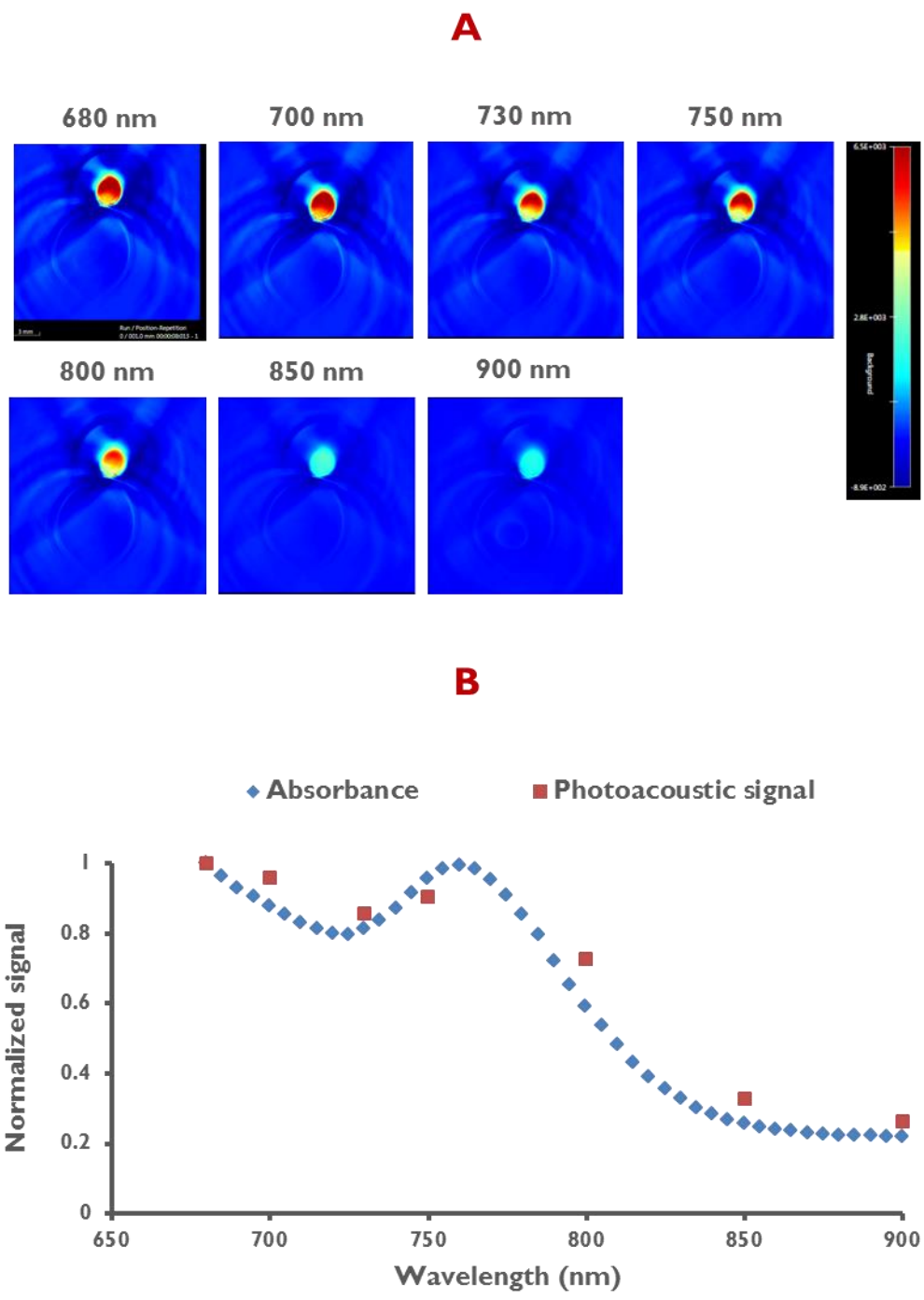

Figure 4.6 Cy5-highCy7-SPION **A.** Optoacoustic images at various wavelengths. **B.** Normalized absorbance and optoacoustic spectra.

The optoacoustic signal versus SPION concentration is shown in **Figure 4.7** at different wavelengths. There was a strong linear correlation between the optoacoustic signal and SPION concentration up to 0.04 mg Fe/mL (answers **Question B)**.

The next objective was to spectrally unmix, with linear regression, the contribution of Cy5-SPIONs from the contribution of Cy7. The absorption spectra of Cy5-SPIONs (**Figure 4.5A**), and Cy7 (**Figure 4.3A**) were inputted into the MSOT software. The first step was to resolve the contribution of Cy5-SPIONs at different concentrations of Cy5-highCy7-SPIONs. MSOT images and subsequent signal quantification of ROIs are shown in **Figure 4.8A and B**. The strong correlation between signal and nanoparticle concentration validates the ability of MSOT to quantify SPION concentrations. MSOT was also able to detect significant optoacoustic differences between control and SPIONs even at 0.005 mg Fe/mL. Future studies (**chapter 5**) include concentrations as low as 0.00078 mg Fe/mL. MSOT was also able to resolve the contribution of Cy7 for different concentrations of Cy5-highCy7-SPIONs with high accuracy and sensitivity (**Figure 4.8C and D**).

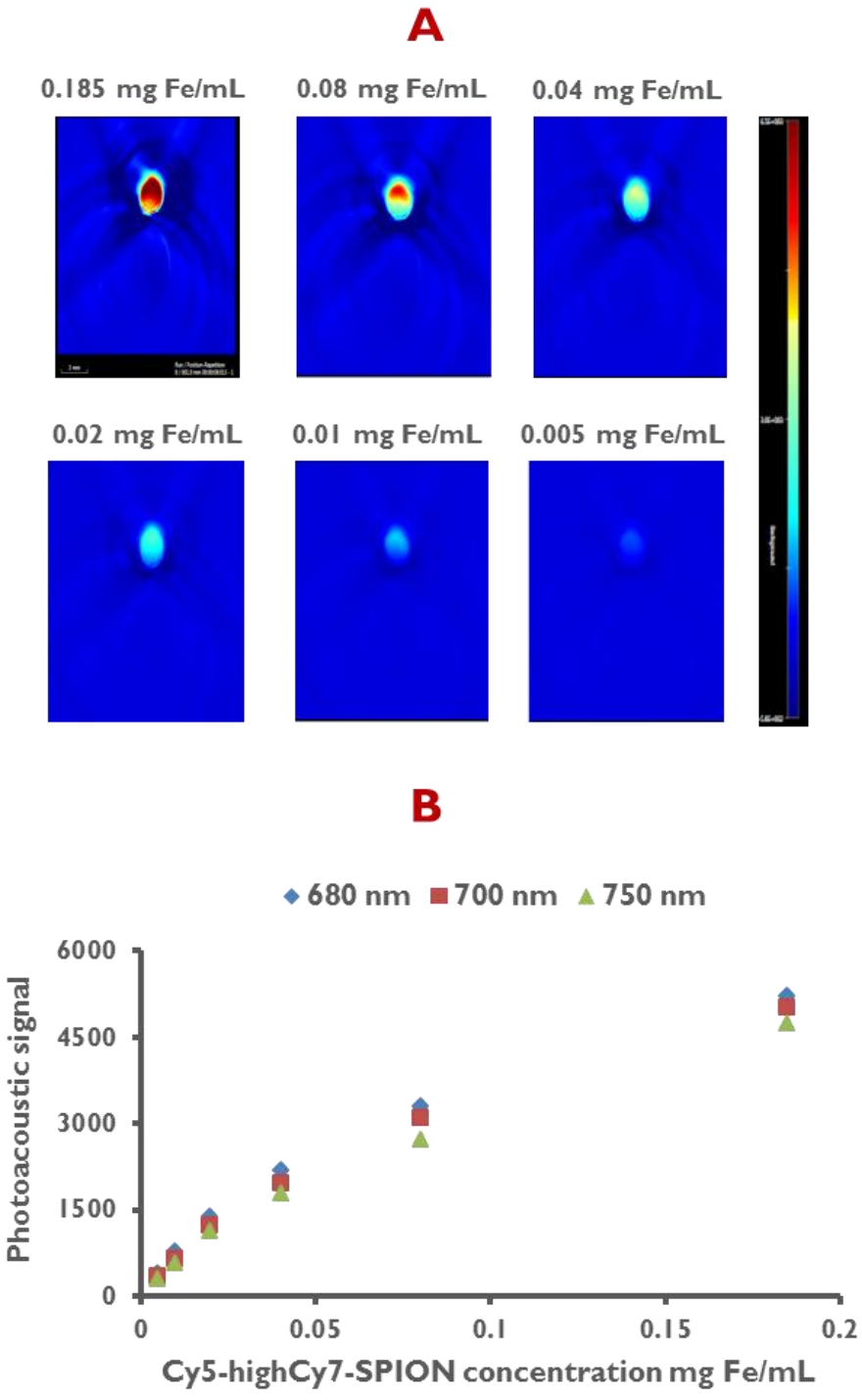

Figure 4.7 Cy5-highCy7-SPION **A.** Optoacoustic signal versus SPION concentration (at 680 nm). **B.** Optoacoustic standard curves are shown at different wavelengths.

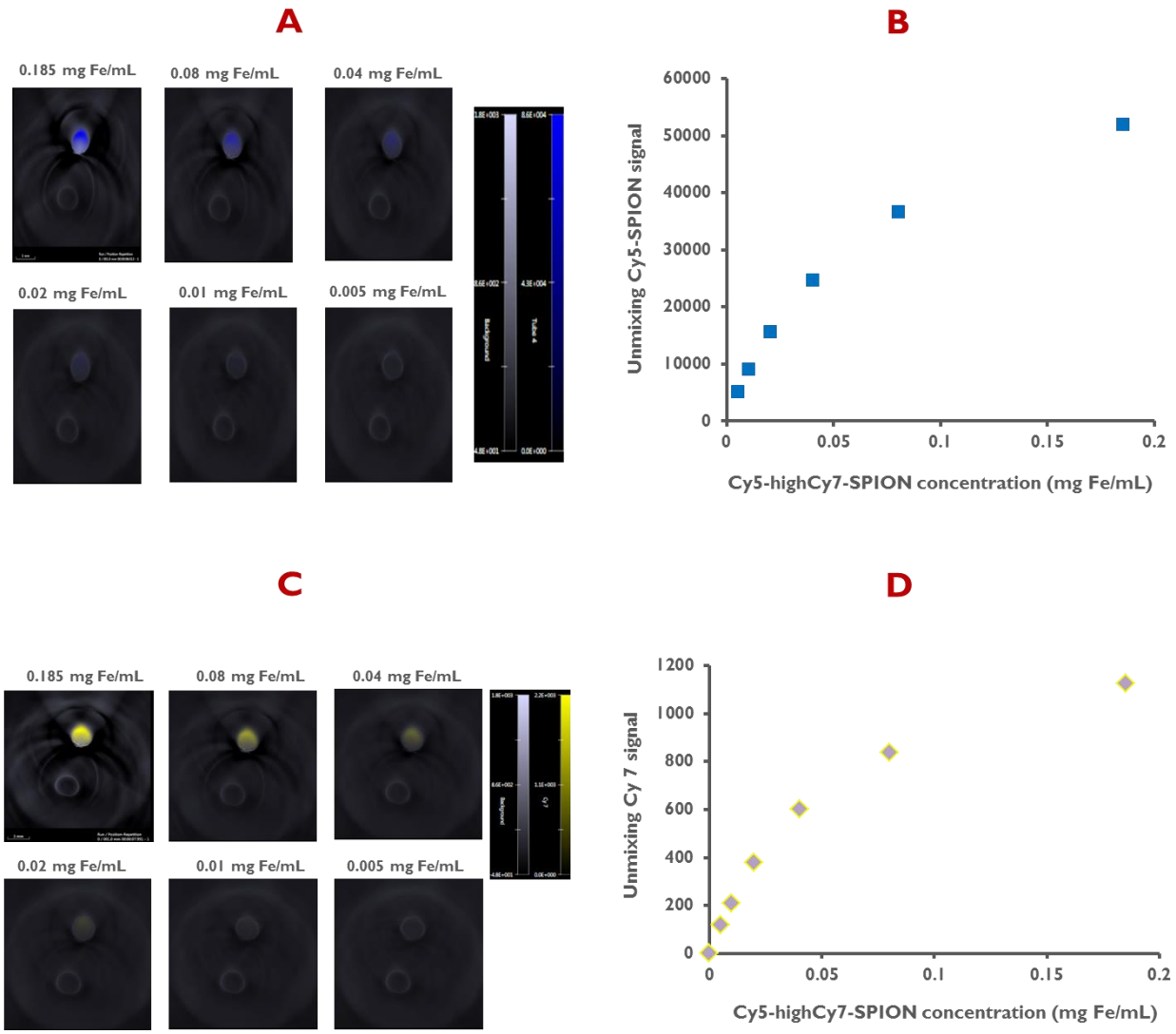

Figure 4.8 Spectral unmixing of Cy5-SPION and Cy7 for different concentrations of Cy5-highCy7-SPION. **A.** Images following spectral unmixing of Cy5-SPION. **B.** Standard curves following quantification of signal (Cy5-SPION). **C.** Images following spectral unmixing of Cy7. **D.** Standard curves following quantification of signal (Cy7).

The MSOT signal ratio of Cy5-SPION over Cy7 was measured for different concentrations of Cy5-highCy7-SPIONs (**Figure 4.9**). The ratio remained relatively constant over the entire concentration range; an important result that indicates that the signal ratio is independent of the SPION concentration.

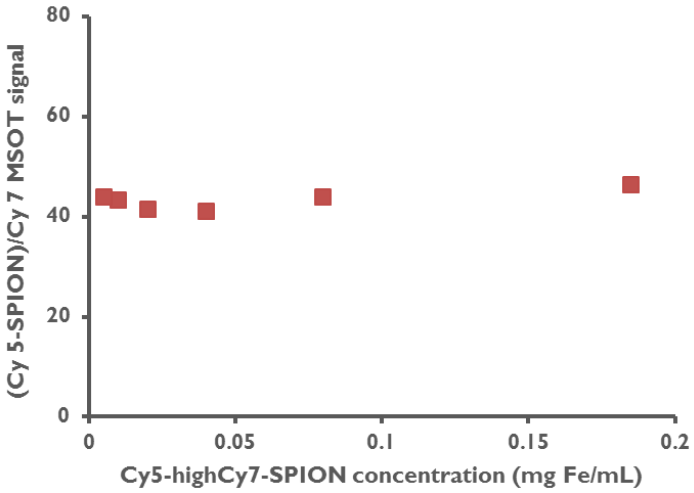

Figure 4.9 The ratio of Cy5-SPION over Cy7 signal remained relatively constant at different Cy5-highCy7-SPION concentrations.

Cy5-SPIONs, Cy5-lowCy7-SPIONs, and Cy5-highCy7-SPIONs were synthesized to model the fate of SPIONs in different tumor microenvironments with varying MMP-2 activities. Cy5-highCy7-SPIONs model the starting particles injected into the mouse, and are expected to stay intact in low MMP-2 activity microenvironments (indolent, low-grade tumors). Cy5-lowCy7-SPIONs model the fate of particles in moderate MMP-2 activity microenvironments (intermediate tumor grade), if Cy7 molecules are linked to SPIONs through an MMP-2 cleavable peptide. Due to its significantly smaller size, Cy7 is expected to diffuse away from the tumor microenvironment following proteolytic cleavage by MMP-2. The third structure (Cy5-SPIONs) carries no Cy7 dye

and represents SPION fate in high MMP-2 activity microenvironments (aggressive, high tumor grade). MSOT images were obtained for all three structures at identical particle concentrations (**Figure 4.10A** shows the Cy7 images). As expected, Cy5-highCy7-SPIONs had the highest Cy7 signal. The Cy5-SPION/Cy7 MSOT signal ratios were then calculated, with Cy5-highCy7-SPIONs having the lowest signal (**Figure 4.10B**).

A

B

SPION	µg Cy7/µg Fe	Cy5-SPION/Cy 7 MSOT signal
Cy5-SPION	0	815.3
Cy5-lowCy7-SPION	0.07 ± 0.04	62.5
Cy5-highCy7-SPION	0.14 ± 0.03	43.8

Figure 4.10 A. Cy7 images for different SPION structures. **B.** Cy5-SPION/Cy7 signal ratio (at identical SPION concentrations).

4.4 Conclusion

Cy5-SPIONs, Cy5-lowCy7-SPIONs, and Cy5-highCy7-SPIONs were synthesized to simulate the fate of SPIONs in different tumor microenvironments with varying proteolytic activities. The concentration of Cy7 on the surface of SPIONs is expected to decrease in the presence of active MMP-2, assuming that Cy7 is linked to SPIONs through an MMP-2 cleavable peptide. To simplify the model, Cy5 and Cy7 dyes were conjugated directly to the surface of SPIONs without the use of an MMP-specific peptide. MSOT demonstrated high sensitivity in quantifying dye-conjugated SPION concentrations and was able to spectrally unmix the contributions of Cy5 and Cy7 for the three synthesized configurations.

Chapter 5 MSOT imaging of the pK and biodistribution of PEGylated Cy7-SPIONs

Multispectral optoacoustic tomography (MSOT) is an emerging non-invasive biomedical imaging modality for whole-body, high-resolution small animal imaging. In this study, the real-time dynamic imaging capability of MSOT was utilized to monitor the pharmacokinetics (pK) and biodistribution of a newly developed MSOT contrast agent based on superparamagnetic iron oxide nanoparticles (SPIONs). SPIONs provide competitive advantages over other nanomaterials due to its safety, biocompatibility, and biodegradability. The surface of SPIONs was decorated with polyethylene glycol (PEG) and Cy7 near-infrared dye to produce a colloidally stable MSOT contrast agent. The effect of varying the molecular weight of PEG (2K, 5K, and 20K) on the pharmacokinetics (pK) and biodistribution of SPIONs was investigated both *in vitro* and *in vivo*.

20K-Cy7-SPIONs were not considered for *in vivo* testing due to rapid sedimentation in cell culture media and rapid uptake by murine RAW 264.7 macrophage cells; a result of strong interparticle interaction in solutions with high ionic strength. 2K and 5K-Cy7 SPIONs remained relatively stable under such conditions, and their uptake by RAW 264.7 cells was negligible – therefore, they were deemed safe for *in vivo* testing. MSOT phantom studies were conducted to test the optoacoustic property of the developed agent, and demonstrated excellent sensitivity, with a detection limit (DL) $\leq$ 0.78 μg Fe/mL. *In vivo* pK and biodistribution studies were then conducted. 2K-Cy7-SPIONs demonstrated significantly prolonged half-life (8.10 ± 1.46 min; $p < 0.01$) in circulation compared to 5K-Cy7-SPIONs (2.75 ± 0.92 min). Both SPIONs accumulated

rapidly in the liver and spleen; reaching maximum values within 15 minutes. As expected, the >100 nm SPIONs experienced minimal accumulation in the kidneys. *Ex vivo* quantitative analysis of tissue distribution with electron paramagnetic resonance (EPR) indicated maximum accumulation of SPIONs in the liver followed by the spleen, and negligible accumulation in the kidneys, brain, and heart. In addition, EPR and MSOT showed excellent agreement –validating MSOT's ability to quantify SPION concentrations with high temporal and spatial resolution.

5.1 Introduction

Non-invasive imaging of the pK and biodistribution profiles of diagnostic imaging agents is essential for their successful translation into the clinic. Real-time dynamic imaging modalities, such as multispectral optoacoustic tomography (MSOT), provide essential biological information about tissues in their native environment. MSOT is an emerging real-time imaging modality that overcomes the limited tissue penetration associated with near-infrared (NIR) imaging. MSOT combines the high contrast of optical imaging with the high resolution of ultrasound imaging for high-throughput *in vivo* whole-body imaging. MSOT relies on the absorption of the pulsed laser by tissue photo-absorbers and the subsequent release of ultrasound waves following thermoelastic expansion [169]. Ultrasound waves scatter considerably less than light, which results in MSOT having significantly higher spatial resolution and deeper penetration depths (few centimeters) compared to conventional NIR imaging [105,114]. In addition, the multispectral feature of MSOT allows for simultaneous detection of endogenous tissue chromophores (e.g. oxy and deoxy-hemoglobin), and exogenous agents (e.g. NIR dyes and nanoparticles) [101–103], and provides up to a 40 fold increase in sensitivity over single wavelength optoacoustic imaging [99]. The non-invasive, tomographic and fast imaging nature of MSOT makes it an excellent choice for non-invasive imaging of the pK and biodistribution profiles of promising imaging agents.

Several nanomaterials, including gold nanorods [112,170,171], gold nanoprisms [172], and single-walled carbon nanotubes [173] have been established as optoacoustic contrast agents, due to their strong absorption and optoacoustic responses in the NIR range and excellent photostability. However, there are serious concerns about the safety, biodegradability, and toxicity of such nanomaterials, which hampers their potential applicability in a clinical setting. On the other hand,

SPIONs are considered relatively safe, biodegradable, and biocompatible, and with proper surface functionalization with a NIR dye, become an excellent contrast agent for MSOT applications. Furthermore, several SPION formulations have already been approved by the FDA, paving the way for future formulations to enter the clinic [53,174].

The success of future SPION formulations as an imaging and/or therapeutic agent depends heavily on their pK and biodistribution profiles. When the intended imaging target is located outside the reticuloendothelial system (RES), it becomes essential that SPIONs evade rapid systemic clearance from circulation. Surface character and hydrodynamic size are the two most important properties that determine the biological fate of SPIONs *in vivo* [53]. **N**aked SPIONs aggregate rapidly when exposed to a physiological environment, and are removed quickly from circulation [175]. To overcome this limitation, a suitable surface coating, such as polyethylene glycol (PEG) can be applied to promote water solubility and steric stabilization in physiological conditions [176]; minimize nonspecific protein adsorption and degradation in the blood for prolonged circulation; and provide additional sites for conjugation of moieties for multifunctionality [156].

The purpose of this study was to develop PEGylated Cy7-SPIONs as a new MSOT contrast agent; assess MSOT's ability to simultaneously track the location of the developed agent in circulation and in multiple organs of elimination; examine the effect of varying the molecular size of PEG, and thus surface composition, on the *in vivo* pK and biodistribution profiles of PEGylated Cy7-SPIONs; and assess the quantitative feature of MSOT imaging by directly comparing it to a reliable *ex vivo* SPION quantification technique.

5.2 Materials and methods

5.2.1 Materials

100 nm starch-coated, fluidMAG-D SPIONs were purchased from Chemicell GmbH. Sulfo-Cyanine7 NHS ester (sulfo-Cy7 NHS) was purchased from Lumiprobe. 2 kDa, 5 kDa and 20 kDa succinimidyl PEG NHS (2K, 5K, and 20K mPEG-NHS) were purchased from Nanocs. L-ascorbic acid, ammonium hydroxide (containing 28-30% ammonia), dimethyl sulfoxide (DMSO), and hydrochloric acid were purchased from BDH Chemicals. Sodium hydroxide (5.0 N), fluorescamine, ethanolamine and epichlorohydrin (99%) were purchased from Alfa Aesar. 10 kDa molecular weight cut-off (MWCO) Pierce BCA Protein Assay Kit and Slide-A-Lyzer dialysis cassette were purchased from Thermo Scientific. MagneSphere Technology magnetic separation stands were purchased from Promega. Iron standard (1000 mg/L Fe in nitric acid) was purchased from Fluka Analytical. Neocuproine hydrochloride monohydrate (99%) was obtained from Acros Organics. Ferrozine iron reagent was purchased from J.T. Baker. Dulbecco's Modified Eagle's Medium (1X, DMEM) and HBSS (1X) were purchased from HyClone. Potassium permanganate (5%) was purchased from Ricca. Ammonium acetate was purchased from VWR. 20% intralipid was purchased from Sigma. Granulated agar was purchased from Difco^{TM}. Deionized (DI) water was generated using an ELGA PURELAB® Flex system.

5.2.2 Synthesis and characterization of 2K, 5K, and 20K-Cy7-SPIONs

Synthesis of aminated SPIONs

Aminated SPIONs were prepared using the method developed by Cole and colleagues.[159] Briefly, 1.4 mL of starch-coated SPIONs (at 17.76 mg Fe/mL) were incubated with 1.5 mL 5N NaOH at room temperature for 15 minutes. Afterward, 650 μL of epichlorohydrin was added

dropwise, vortexed for a minute, and incubated for 24 hours at room temperature with gentle shaking. The resulting cross-linked SPIONs were dialyzed against DI water for 24 hours using a 10 kDa MWCO dialysis cassette to remove excess, unreacted reagents, and then incubated with 1 mL ammonium hydroxide (28-30 % ammonia) at room temperature for 24 hours. The cross-linked, aminated SPIONs were dialyzed against DI water for 48 hours using 10 kDa MWCO dialysis cassette. The final purified product was concentrated to 10 mg Fe/mL using a magnetic separator.

Synthesis of 2K, 5K and 20K PEGylated SPIONs with and without Cy7

PEGylated Cy7-conjugated SPIONs were prepared by incubating a mixture of 495 μL Sulfo-Cy7 NHS (5 mg/mL in H_2O), 750 μL aminated SPIONs (10.08 mg Fe/mL in H_2O; 1590.15 nmol amine/mg Fe), 750 μL 0.2M sodium bicarbonate buffer (pH 8.5), and 600 μL DMSO for 80 minutes at room temperature with gentle mixing. This corresponds to a 1 to 4 Cy7 to amine ratio. The solution was sonicated for 1 minute at 10% amplitude and then split equally into three samples - to which either 2K, 5K, or 20K mPEG-NHS was added at a 1.3:1 PEG to amine molar ratio. Additional DMSO and 0.2M sodium bicarbonate were added at a 16.7% v/v ratio, and the samples were incubated for 3 hours at room temperature and labeled 2K-Cy7-SPIONs, 5K-Cy7-SPIONs, and 20K-Cy7-SPIONs. Following incubation, samples were sonicated for 2 minutes at 10% amplitude and then washed four times using a magnetic separator to remove unbound Cy7 and PEG. Samples were sonicated for 30 seconds (8% amplitude) after each wash. Control 2K, 5K, and 20K-SPIONs were synthesized as described above, without the addition of Cy7.

Amine quantification assay

The amine content of aminated SPIONs was determined using a quantitative fluorescamine assay. Briefly, 50 µL fluorescamine (3 mg/mL in DMSO) was added to 250 µL SPION samples (0.4 mg Fe/mL), incubated for 10 minutes at room temperature, and centrifuged for 24 minutes at 14,000 RPM. 200 µL of the supernatants were transferred to a 96 well plate, and fluorescence was measured at 400/460 nm using a FlexStation 3 microplate reader (Molecular Devices). Standard curves were created using ethanolamine between 0 and 0.8 mM amine.

Size, PDI and zeta potential measurement

The hydrodynamic size (backscattering angle of 173 ◦C), polydispersity index (PDI) and zeta potential (Smoluchowski model) of 0.05 mg Fe/mL SPIONs were measured by dynamic light scattering (DLS) using Malvern Zetasizer Nano ZS (Malvern, UK).

Quantification of nmol Cy7/ mg Fe

The amount of conjugated Cy7 was calculated by measuring the corrected absorbance of PEGylated Cy7-SPIONs at 750 nm. A standard curve was created by measuring the absorbance values of sulfo-Cy7 NHS between 0 and 5 µg Cy7/mL at 750 nm.

5.2.3 Size stability and *in vitro* uptake of PEG-Cy7-SPIONs by RAW 264.7 cells

In vitro uptake by RAW 264.7 macrophage cells

RAW 264.7 murine macrophage cells were cultured in 100 mm dishes containing cell culture media (89% DMEM, 10% FBS, and 1% antibiotics) in a cell incubator (37 ºC, 5% CO_2). After reaching ~70-80% confluency, cells were harvested with a cell scraper then seeded at $1.3*10^5$

cells/well (500 μL) in a 24-well plate. The plate was incubated for 24 hours to allow cells to reach ~70-80% confluency and then washed with HBSS. 500 μL of aminated or PEGylated (with and without Cy7) SPIONs in DMEM was added at a concentration of 0.07 mg Fe/mL. The control consisted of blank media without SPIONs. After a 4-hour incubation period, wells were washed three times with 1X PBS, suspended in 100 μL 1X PBS and 200 μL 50 mM NaOH, and incubated for 30 minutes at 37 ºC. Two 25 μL samples were transferred to 1 96-well plate for quantitative protein analysis with the BCA assay, while the remaining 250 μL of cell lysate was kept in the original 24-well plate for quantitative iron analysis with the ferrozine assay.

In the BCA assay, 200 μL of the BCA working reagent was mixed with 25 μL cell lysate, incubated at 60 ºC for 30 minutes, cooled down to room temperature for 5 minutes, and spectrophotometrically analyzed at 562 nm. A standard curve was created by measuring the BCA signal of varying RAW 264.7 cell number (counted with a hemocytometer).

The ferrozine assay was based on the procedure developed by Riemer and colleagues [166]. In it, 250 μL of equal volumes of 4.5% $KMnO_4$ and 1.4M HCl were added to 250 μL cell lysate and incubated for 2 hours at 60 ºC. 62.5 μL of ferrozine solution (6.5mM ferrozine, 6.5mM Neocuproine, 2.5M ammonium acetate, and 1M ascorbic acid in H_2O) was added, followed by 30-minute incubation at room temperature. 250 μL solutions were then transferred to a 96 well plate and absorbance was measured at 550 nm. Standard curves were created using known concentrations of SPIONs between 0 and 6.7 μg Fe/mL.

SPION size stability in RAW 264.7 cell culture medium

Aminated SPIONs, 2K-Cy7-SPIONs and 5K-Cy7-SPIONs were mixed with RAW 264.7 cell culture medium (DMEM + 10% FBS + 1% antibiotics) at a concentration of 0.07 mg Fe/mL, then placed inside a cell culture incubator for 74 hours. At set time points, particle size was measured using DLS. Due to rapid aggregation, the particle size of 20K-Cy7-SPIONs in DMEM was measured continuously for 17 minutes.

5.2.4 MSOT phantom studies of PEG-Cy7-SPIONs

Preparation of MSOT phantom gels

A tissue-mimicking scattering agar phantom was prepared. A 15-mL preheated solution of 1.5% agar and 1% intralipid was added to a 20-mL syringe with an internal diameter of 2 cm, then cooled down to room temperature until the gel polymerized. Two cylindrical channels, one for the sample and the other for the control, were made by inserting 3 mm straws into the gel after it polymerized.

Measuring the optoacoustic properties of 2K-Cy7-SPIONs and 5K-Cy7-SPIONs with MSOT

Phantom imaging was done in a temperature-controlled water bath within MSOT's inVision 256-TF imaging system (iThera Medical, Munich, Germany). MSOT measurements of various dilutions of 2K-Cy7-SPION and 5K-Cy7-SPIONs, from 0.00078 to 0.025 mg Fe/mL, were acquired at 680, 710, 730, 740, 760, 785, 800, 850 and 900 nm using 25 averages (laser pulses) per illumination wavelength. Data was processed by iThera Medicals MSOT software. Image reconstruction and multispectral unmixing were based on a back-projection algorithm and least-squares linear regression, respectively.

5.2.5 MSOT imaging of *in vivo* pK and biodistribution of PEG-Cy7-SPIONs

Animal experiments presented in this work were approved by Auburn University's Institutional Animal Care and Use Committee (IACUC).

All animals were shaved on both sides and weighed before the experiment, then placed on a polyethylene membrane attached to a small animal holder that was connected to an isoflurane chamber set at 2% for constant anesthesia delivery. Long polyethylene catheter tubing (0.28 mm I.D. and 0.61 mm O.D.) was connected to the mouse's lateral tail vein via a 30 G needle. A generous amount of ultrasound gel was applied evenly on both sides of the mouse, and the animal holder was placed inside the MSOT's water bath with the ventral side of the mouse facing upwards and the dorsal side facing the transducer. The mouse was given sufficient time to equilibrate to the bath's 34 ºC temperature while being anesthetized under 2% isoflurane, and its breathing rate was continuously monitored throughout the imaging process.

The MSOT parameters were selected, which included the illumination wavelengths of 680, 710, 730, 740, 760, 785, 800, 850 and 900 nm, and the number of frames per wavelength (25). The tail vein position was marked prior to SPION injection, and transverse slices of the liver, spleen, kidneys, and the neck region were selected. Pre-scan images were acquired and served as a control for direct comparison to MSOT images post-injection.

2K or 5K-Cy7-SPIONs (10 mg Fe/kg) were intravenously injected via a catheter into the tail vein of BALB/c mice and its pK and biodistribution were immediately monitored up to 70 minutes after injection. Additional scans were gathered at later time points, with some mice being imaged up to 3 days after injection. The mice were then euthanized via isoflurane overexposure and cervical dislocation. The heart, spleen, liver, kidneys, and brain were gathered and frozen at -

80 °C. MSOT images were reconstructed using a back-projection algorithm, followed by multispectral processing using linear regression. A region of interest (ROI) was drawn around the liver, spleen, kidneys and the jugular vein, and signal quantified using the ViewMSOT software.

Plasma pK analysis was performed using Microsoft Excel's PK solver 2.0 add-in program. The pK profiles of plasma concentration *C(t)* versus time *t* were fitted into a one-compartment model (equation 5.1):

$$C(t) = C_0 e^{-kt} \qquad (Eq. 5.1)$$

Where C_o is the initial plasma SPION concentration after injection and *k* is the elimination rate constant. Equations 5.2-5.4 were used to calculate the circulation half-life ($t_{1/2}$), the total area under the plasma concentration-time curve ($AUC_{0\rightarrow\infty}$), and clearance (*CL*).

$$t_{1/2} = \frac{\ln(2)}{k} \qquad (Eq. 5.2)$$

$$AUC_{0\rightarrow\infty} = \int_0^\infty C(t)dt \qquad (Eq. 5.3)$$

$$CL = \frac{k * Dose}{C_o * Body\ weight} \qquad (Eq. 5.4)$$

Analysis of SPION biodistribution in the liver and spleen was done by plotting the normalized MSOT signal *y(t)* over time. The time for the signal to reach half its maximum value ($t_{1/2max}$) was calculated by fitting equation 5.5 into the biodistribution profiles for the initial period up to its maximum value:

$$y(t) = 100 - (A_o e^{-Bt}) \qquad (Eq. 5.5)$$

$$t_{1/2max}(liver, spleen) = \frac{\ln 2}{B} \qquad (Eq. 5.6)$$

5.2.6 Quantitative *ex vivo* analysis with electron paramagnetic resonance (EPR)

The concentration of SPIONs in *ex vivo* tissues was quantified using Bruker's EMX EPR Spectrometer. Tissue samples were inserted into the bottom of EPR tubes (Wilmad-LabGlass) using the technique developed by Chertok and colleagues [122]. Briefly, frozen tissues were partitioned into small samples with a blade and pushed into the bottom of EPR tubes, pre-cooled to subzero temperatures on dry ice, with a glass rod. The net mass was determined by weighing the EPR tube before and after sample loading. Triplicate samples were loaded for the liver. Due to their smaller size, only one sample was loaded for the remaining tissues. The resonance frequency was set at 9.4 GHz; microwave power (P) at 1.99 mW; modulation amplitude at 6 G; receiver gain at 6.32×10^2; and temperature at 77 K. EPR spectra were plotted as dP/dB versus the magnetic field B (Gauss), and the double integral $\iint(dP/dB)dBdB$ calculated using Bruker's EPR software. In addition, the background EPR spectra of control tissues were measured by gathering tissues from mice not exposed to either type of SPIONs. A calibration curve was created by measuring the EPR spectra of samples between 0 and 0.06 mg Fe and plotting the $\iint(dP/dB)\ dBdB$ versus SPION concentration.

5.2.7 Statistical analysis

Experiments were run in triplicates unless otherwise stated. Data are presented as mean ± S.D., and p values were calculated using student's t-test.

5.3 Results and discussion

5.3.1 Synthesis and characterization of PEGylated Cy7-SPIONs

Several nanomaterials, including gold nanorods and carbon nanotubes, have been investigated as MSOT contrast agents due to their intrinsic absorption properties in the NIR range. However, these materials typically suffer from long retention times in tissues, which raises serious toxicity concerns [177]. On the other hand, SPIONs are biocompatible, biodegradable and considered safe by the FDA. In this study, The NIR dye Cy7 was conjugated to SPIONs to generate optoacoustic contrast and allow real-time dynamic tracking of SPION distributions in various compartments in vivo.

The reaction scheme for synthesizing PEGylated Cy7-SPIONs is illustrated in **Figure 5.1**. Cross-linked, aminated SPIONs were first prepared from starch-coated SPIONs using the method developed by Cole and colleagues [159]. The well-established NHS-amine reaction chemistry was then used to conjugate sulfo-Cy7 NHS and mPEG-NHS (2K, 5K or 20K) to the surface of aminated SPIONs. The optimum reaction conditions were determined through extensive optimization experiments, and involve incubating sulfo-Cy7-NHS with aminated SPIONs at pH 8.5 for 80 minutes at a 1:4 Cy7 to NHS ratio, followed by addition of mPEG-NHS at a 1.3:1 PEG to NHS ratio. The NIR dye sulfo-Cy7-NHS was chosen due to its strong optoacoustic property around 750 nm, which allows for sensitive MSOT imaging of SPION pK and biodistribution. PEG was chosen for its hydrophilicity and addition of steric stabilization to SPIONs.

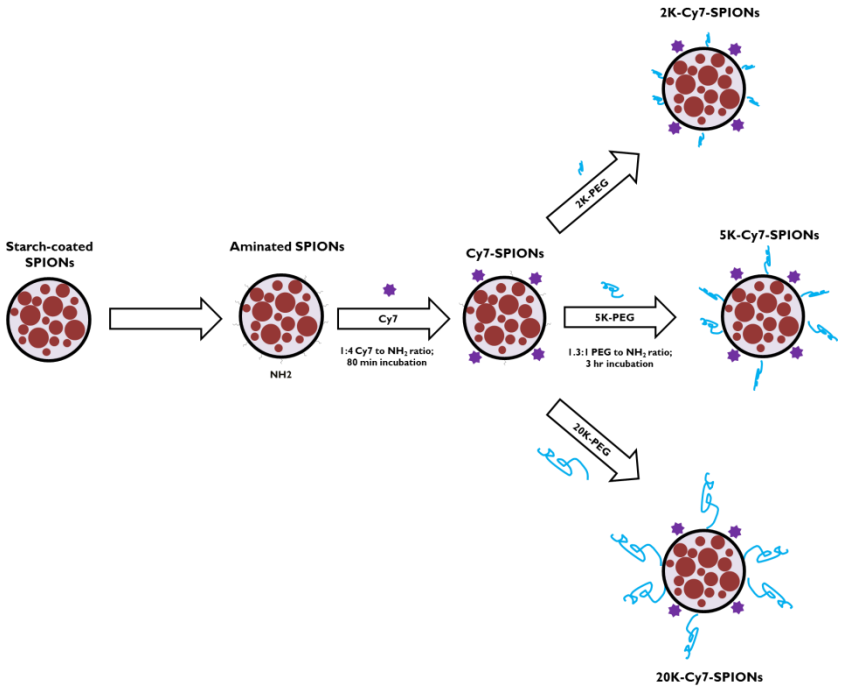

Figure 5.1 Reaction scheme for synthesizing 2K, 5K, and 20K-Cy7-SPIONs. NHS-amine reaction chemistry was used to conjugate sulfo-Cy7 NHS, then mPEG-NHS (2K, 5K or 20K) to the surface of aminated SPIONs.

DLS was used to measure the hydrodynamic diameter and zeta potential of aminated SPIONs and PEGylated Cy7-SPIONs in H_2O (**Table 5.1**). The addition of sterically-stabilizing PEG resulted in the breakage of small aggregates of neighboring SPIONs and an overall decrease in hydrodynamic diameter. Aminated SPIONs had a high positive zeta potential due to the presence of positively charged amine groups on its surface. The presence of neutral-charged 2K, 5K, and 20K PEG on the surface of SPIONs (without Cy7) caused a shift in zeta potential towards neutral values (results not shown here). Finally, the presence of negatively-charged Cy7 caused a shift in zeta potential towards negative values.

Table 5.1 DLS characterization of PEGylated Cy7-SPIONs in DI H_2O.

	Hydrodynamic diameter (nm) in H_2O	**Zeta potential (mV)**
Aminated SPIONs	136.20 ± 0.28	+52.67 ± 0.98
2K-Cy7-SPIONs	116.65 ± 7.00	-29.00 ± 0.92
5K-Cy7-SPIONs	96.89 ±0.06	-13.80 ±0.95
20K-Cy7-SPIONs	101.5 ± 2.10	-20.10 ± 2.2

The concentration of Cy7 on the surface of 2K, 5K, and 20K-Cy7-SPIONs was quantified through spectrophotometric analysis at 750 nm. 2K-Cy7-SPIONs had the highest concentration of Cy7 on their surface, equal to 83.3 nmol Cy7/mg Fe. The percentage coverage of amine groups by Cy7 was then calculated by dividing Cy7 concentration (nmol Cy7/mg Fe) by amine concentration (nmol NH_2/mg Fe). 5.24, 4.77 and 4.38% of total available amine groups were covered by Cy7 in 2K, 5K, and 20K-Cy7-SPIONs, respectively (**Table 5.2**). Despite the addition of equivalent molar amounts, the molecular weight of PEG had a clear impact on the amount of conjugated Cy7.

Table 5.2 Quantifying nmol Cy7/mg Fe and % coverage of amine groups by Cy7.

	nmol Cy7/ mg Fe	nmol Cy7/ nmol NH_2	% coverage of NH_2 groups by Cy7
2K-Cy7-SPIONs	83.3	0.052	5.24
5K-Cy7-SPIONs	75.9	0.048	4.77
20K-Cy7 SPIONs	69.6	0.044	4.38

5.3.2 Size stability and *in vitro* uptake of PEG-Cy7-SPIONs by RAW 264.7 cells

The plasma clearance process of SPIONs involves the RES – primarily macrophage uptake following opsonization of SPIONs by plasma proteins. This process is highly dependent on the size and surface properties of SPIONs. Conjugating hydrophilic, neutral-charged PEG moieties create stealth nanoparticles that are less visible to macrophages of the liver and spleen. In this study, *in vitro* RES simulations were conducted to study the macrophage uptake and colloidal stability of SPIONs coated with various sizes of PEG.

The uptake of aminated and PEGylated SPIONs (with and without Cy7) by murine RAW 264.7 macrophage cells was tested to simulate the *in vivo* reticuloendothelial macrophage uptake process. **Figure 5.2A** indicates that the uptake of 2K-SPIONs (622.15 fg Fe/cell, $p < 0.01$), 5K-SPIONs (460.43 fg Fe/cell, $p < 0.01$), 20K-SPIONs (369.59 fg Fe/cell, $p < 0.01$), 2K-Cy7-SPIONs (1114.68 fg Fe/cell, $p < 0.01$) and 5K-Cy7-SPIONs (152.46 fg Fe/cell, $p < 0.01$) were significantly lower compared to aminated SPIONs (9430.87 fg Fe/cell) and 20K-Cy7-SPIONs (10604.16 fg Fe/cell). The highly positively charged aminated nanoparticles adhered strongly to the

predominantly negative charge of cellular membranes, while 20K-Cy7-SPIONs visibly aggregated and adhered on top of the cell layer at the bottom of the plate leading to significantly higher cellular uptake [165,178]. The different mechanisms of cellular uptake – SPION-cell electrostatic interactions vs SPION aggregation – were validated by measuring SPION size stability in culture media with DLS. The hydrodynamic diameter of 20K-Cy7-SPIONs increased by 395.1 nm after 1 minute and reached 1 μm after 15 minutes (**Figure 5.2B**); indicating rapid aggregation due to strong particle-particle interactions in ionic solutions. Meanwhile, the hydrodynamic diameter and PDI of aminated SPIONs remained relatively constant in culture media over a period of 74 hours (**Figure 5.2C**).

The hydrodynamic diameter of 2K-Cy7-SPIONs and 5K-Cy7-SPIONs also remained relatively constant in cell culture media throughout the duration of the study. It is interesting to note that the initial hydrodynamic diameter of 2K-Cy7-SPIONs (72.2 nm) and 5K-Cy7-SPIONs (83.6 nm) were significantly smaller in culture media than in DI H_2O; indicating that the SPION aggregation/deaggregation phenomenon is highly dependent on the solvent conditions. In addition, while 2K-Cy7-SPIONs exhibited similar PDI values in DI H_2O and in culture media, 5K-Cy7-SPIONs had a significantly higher PDI in culture media than in DI H_2O. The difference in the behavior of the three PEGylated Cy7-SPIONs is due to the larger-sized PEG adopting a more mushroom-like (i.e. less brush) conformation in solutions with higher ionic strengths; thus, reducing the steric stabilization potential of PEG. This results in more intense hydrophobic interactions between Cy7 molecules on neighboring 5K-Cy7-SPIONs molecules (higher PDI) and rapid sedimentation – i.e. salting out – of 20K-Cy7-SPIONs in solutions with higher ionic strengths. To validate this theory, we synthesized Cy7-SPIONs without PEG. The resulting

particles aggregated rapidly even in H_2O due to strong hydrophobic interactions between Cy7 molecules on neighboring SPIONs that were no longer sterically shielded by PEG.

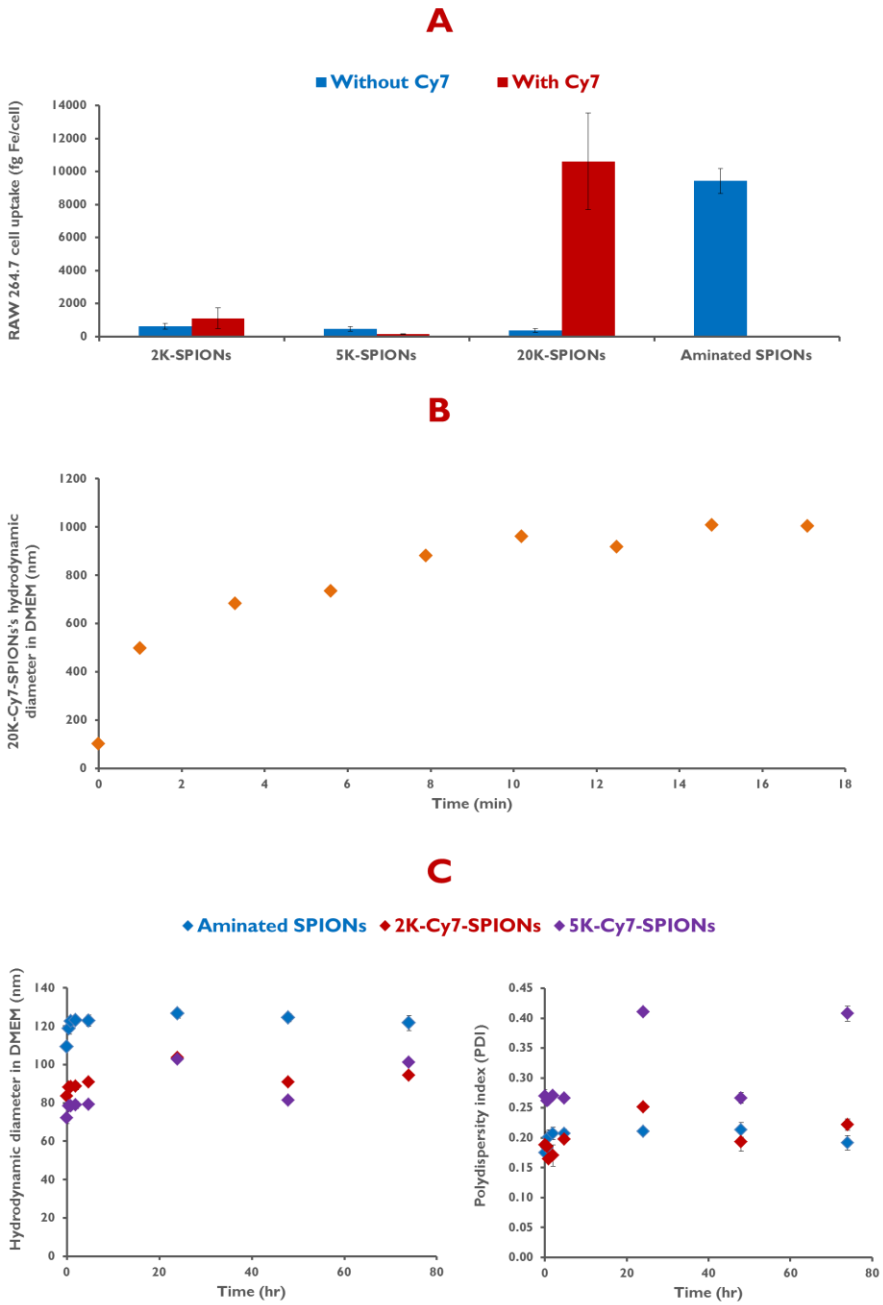

Figure 5.2 A. RAW 264.7 uptake. **B.** Size stability of 20K-Cy7-SPIONs in DMEM. **C.** Size stability and PDI of Aminated SPIONs, 2K-Cy7-SPIONs and 5K-Cy7-SPIONs in DMEM.

5.3.3 MSOT phantom studies of PEG-Cy7-SPIONs

MSOT phantom studies were conducted to measure the optoacoustic properties of 2K-Cy7-SPIONs and 5K-Cy7-SPIONs and to determine the sensitivity of the imaging system. Tissue-mimicking, scattering agar phantom gels were prepared according to the protocol provided by iThera Medical. Two cylindrical channels were generated within the phantom gel to accommodate both the tested sample and the control. The absorption profiles of 2K and 5K-Cy7-SPIONs were measured and inputted into the MSOT software. Importantly, the developed imaging agent had a distinctive absorption spectrum compared to the endogenous molecules hemoglobin and deoxyhemoglobin. Image reconstruction was based on a back-projection algorithm, and signal quantified around regions of interest (ROI) for each of the measured wavelengths to generate an optoacoustic spectrum. The optoacoustic and absorbance spectra followed a very similar trend in the 680-900 nm range with small differences due to minor changes in laser fluence distribution during optoacoustic imaging (Figure 3A). The absorption spectra of the individual absorbers were fit, based on least-squares linear regression, to the pixel intensities at different wavelengths. Images and subsequent quantification of MSOT signal for different concentrations of 2K and 5K-Cy7-SPIONs (R2>0.995) are shown in **Figures 5.3B and 5.3C**, respectively. Due to the higher concentration of Cy7 on its surface, 2K-Cy7-SPIONs exhibited stronger optoacoustic properties than 5K-Cy7-SPIONs. In addition, MSOT demonstrated excellent sensitivity, with a detection limit (DL) ≤ 0.78 μg Fe/mL, lower than other materials that include gold nanoprisms (DL=2.5 μg/mL) [109], Au–Fe_2C Janus nanoparticles (DL=25 μg/mL, R^2=0.973) [179], CuInS/ZnS quantum dots (DL=25 μg/mL, R^2=0.98) [180], star-shaped gold nanoparticles (DL=3.1 μg/mL, R^2=0.9982) and rod-shaped gold nanoparticles (DL=3.1 μg/mL, R^2=0.9822) [171].

2K and 5K-Cy7-SPIONs demonstrated high stability in culture media; negligible uptake by murine macrophage cells *in vitro*; and excellent optoacoustic properties. Therefore, both structures were deemed ready for an *in vivo* pK and biodistribution study.

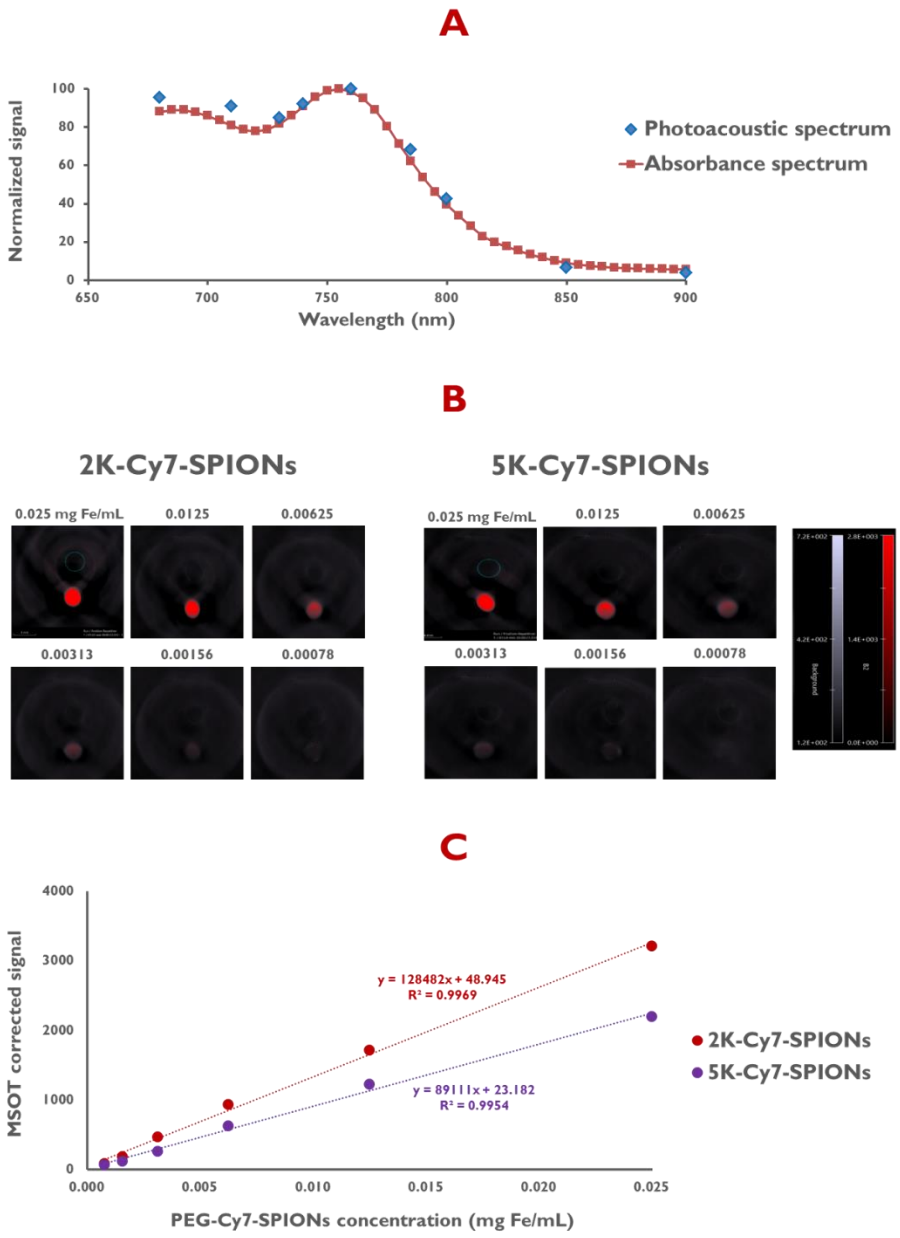

Figure 5.3 MSOT phantom studies **A.** Optoacoustic and absorbance spectra. **B.** MSOT images of phantom gels at different SPION concentrations. **C.** MSOT signal vs. SPION concentration.

5.3.4 MSOT imaging of *in vivo* pK and biodistribution of PEG-Cy7-SPIONs

MSOT was used to visualize and quantify the probe's pK and biodistribution *in vivo* following intravenous injection. The rate of nanoparticle clearance from circulation was monitored by longitudinal imaging of the neck region and quantifying signal around the jugular vein (**Figure 5.4A**). A one-compartment pK model was fit into the concentration versus time data, as shown in **Figure 5.4B**. 2K-Cy7-SPIONs demonstrated a longer circulation half-life and slower plasma clearance ($t_{1/2}$ = 8.10 min, *CL*=54.27 mL/min/kg) compared to 5K-Cy7-SPIONs ($t_{1/2}$ = 2.75 min, *CL*=108.83 mL/min/kg). In addition, plasma was exposed to nearly twice the amount of 2K-Cy7-SPIONs ($AUC_{0\rightarrow\infty}$ = 0.243 mg*min/mL) from a single dosage compared to 5K-Cy7-SPIONs ($AUC_{0\rightarrow\infty}$ = 0.134 mg*min/mL).

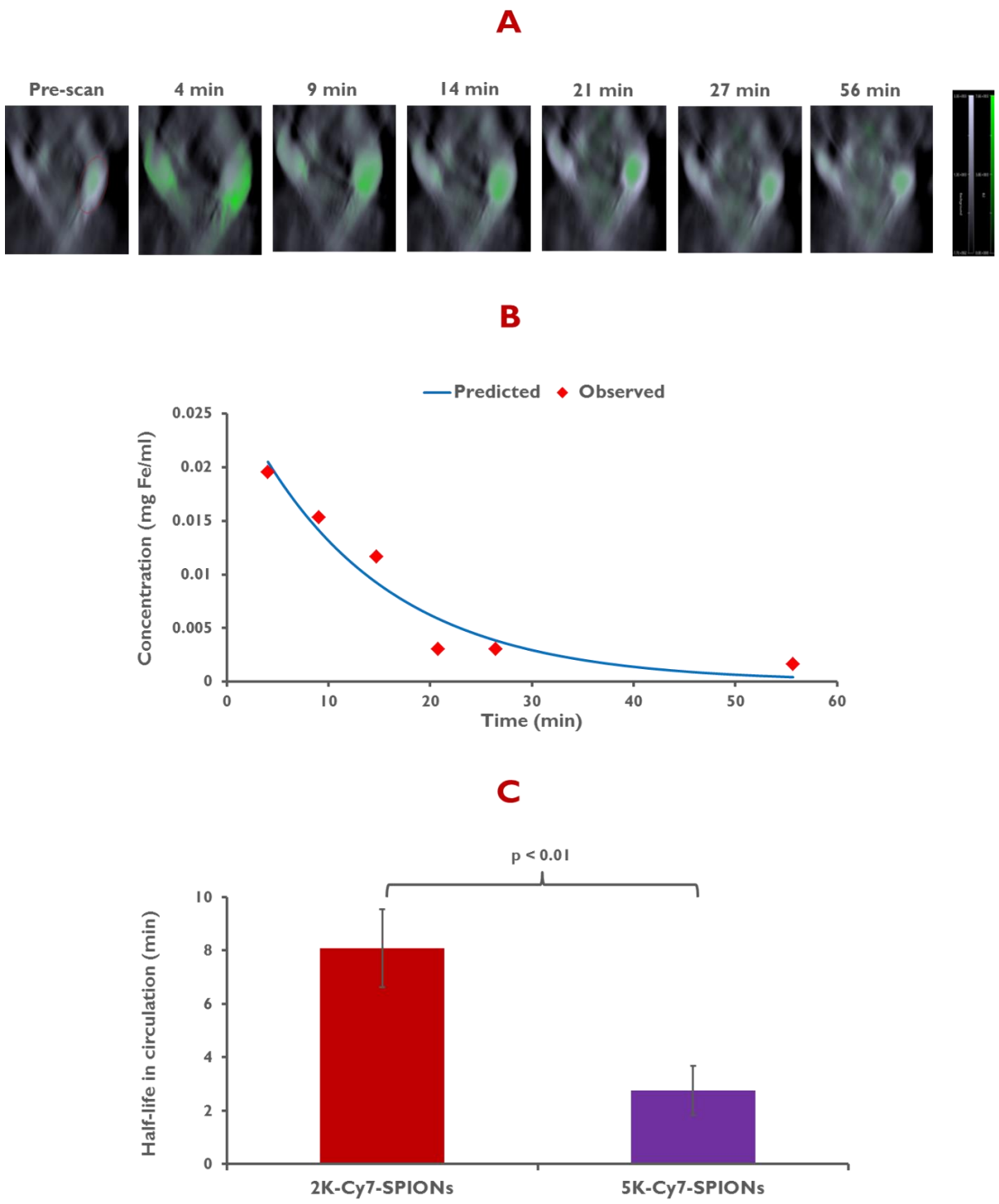

Figure 5.4 A. MSOT images of the jugular vein before and after injection of 2K-Cy7-SPIONs. **B.** Observed pK data in the jugular vein along with a one-compartment pK fit. **C.** Circulation half-life of 2K and 5K-Cy7-SPIONs.

The biodistribution of SPIONs in the liver (**Figure 5.5**), spleen (**Figure 5.6**), and kidneys (not shown) was monitored. Opsonization and subsequent macrophage uptake of circulating SPIONs resulted in its rapid clearance by the liver and spleen; with signal reaching half its maximum value in 5.43 min (2K-Cy7-SPIONs) and 5.56 min (5K-Cy7-SPIONs) in the liver, and 4.61 min (2K-Cy7-SPIONs) and 3.33 min (5K-Cy7-SPIONs) in the spleen. The pK and biodistribution results matched very well: Rapid clearance of SPIONs from circulation through macrophage uptake (circulation-$t_{1/2}$ < 10 min) resulted in its rapid accumulation in the liver and spleen ($t_{1/2\ max,\ liver}$ and $t_{1/2\ max,\ spleen}$ < 10 min). Finally, the size of SPIONs (>100 nm) was significantly higher than the cutoff for renal filtration – resulting in a negligible change in MSOT signal in the kidneys throughout the duration of the study.

In a similar study conducted by Cole and colleagues, 2K and 5K PEGylated SPIONs that were synthesized with the same starting material had significantly longer circulation half-lives (7.29 hr and 11.75 hr, respectively) compared to the PEGylated Cy7-SPIONs used in this study [159]. The surface charge and hydrophobicity of SPIONs affects their colloidal stability and electrostatic binding of plasma proteins [181]. It is possible that, despite decent size stability and minimal uptake by macrophages *in vitro*, the negatively charged PEGylated Cy7-SPIONs interacted strongly with circulating plasma proteins (opsonins) such as albumin, complement proteins, fibronectins, fibrinogens and immunoglobulins in their native environment, resulting in rapid clearance from circulation [182].

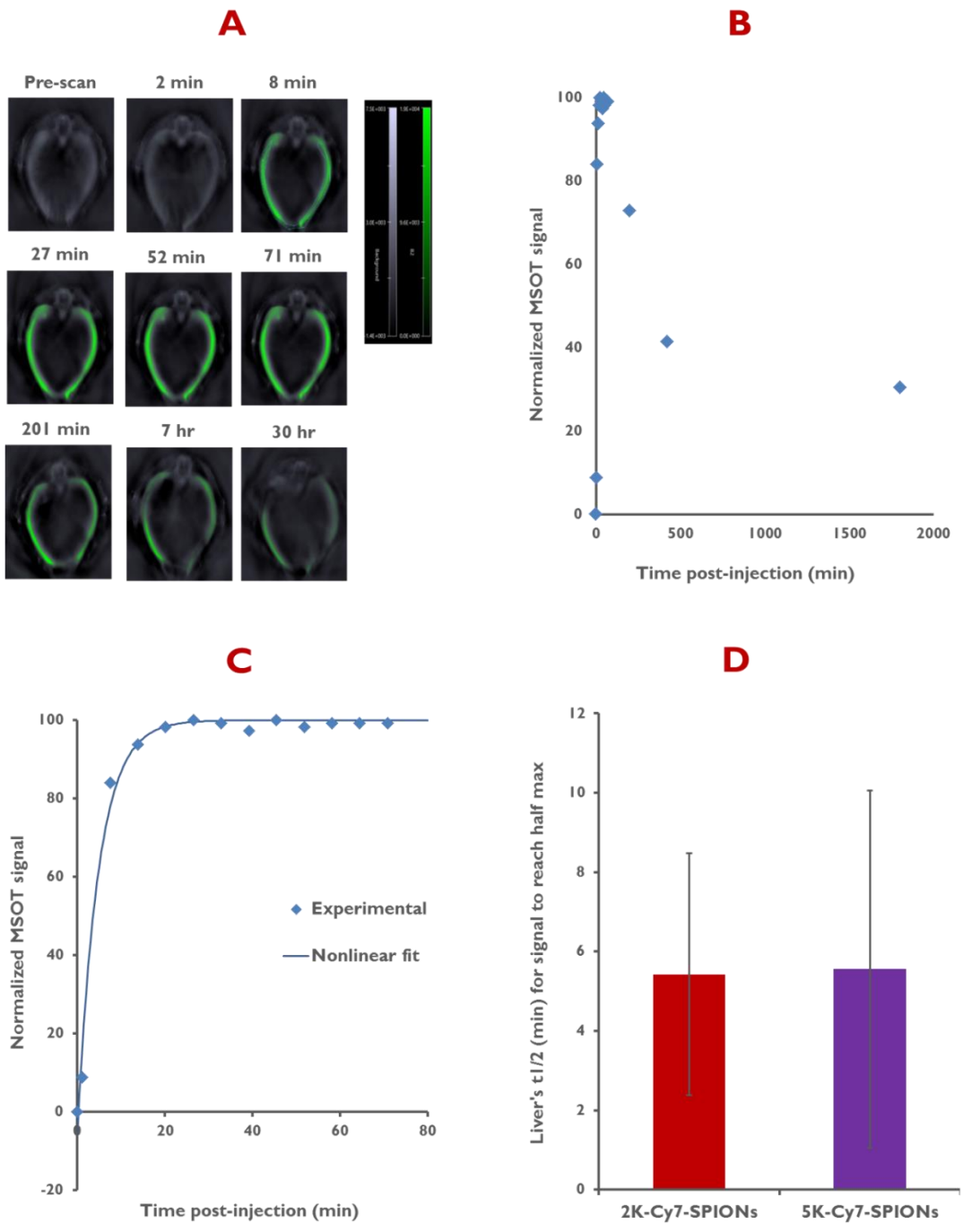

Figure 5.5 Biodistribution of SPIONs in the liver. **A.** MSOT images of the liver before and after injection of 2K-Cy7-SPIONs. **B.** MSOT signal in the liver over the entire period. **C.** MSOT signal for the first 70 min. **D.** $t_{1/2\ max,\ liver}$ (time for the signal to reach half its maximum value).

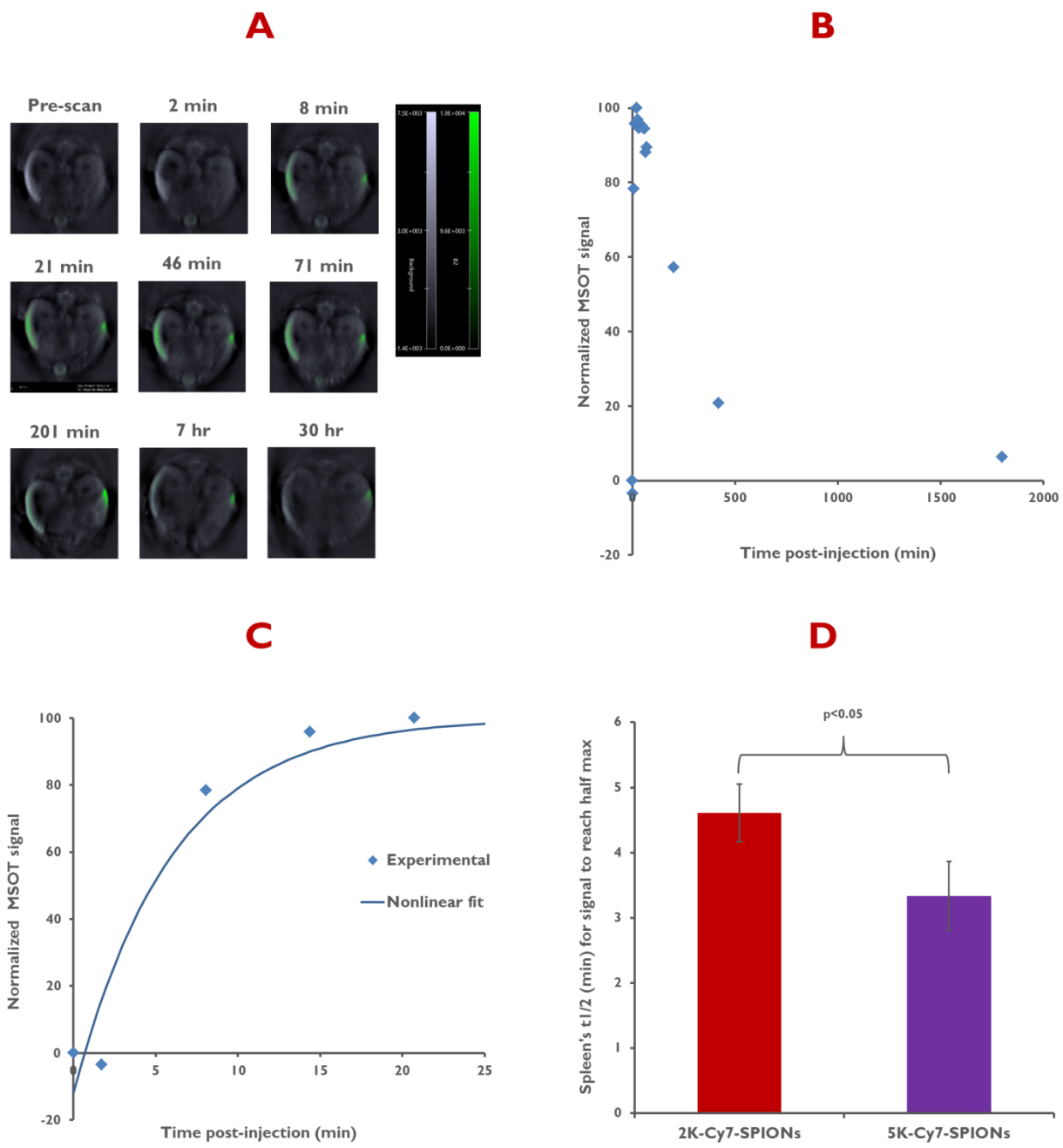

Figure 5.6 Biodistribution of SPIONs in the spleen. **A.** MSOT images of the spleen before and after injection of 2K-Cy7-SPIONs. **B.** MSOT signal in the spleen over the entire period. **C.** MSOT signal for the first 25 min. **D.** $t_{1/2\ max,\ spleen}$ (time for the signal to reach half its maximum value).

5.3.5 Validating MSOT measurements with EPR spectroscopy

EPR is a well-established method for quantifying SPION concentrations in *ex vivo* tissues [122,159]. EPR standard curves demonstrated an excellent linear trend between EPR signal and SPION concentration (results not shown here). Quantitative EPR analysis of the liver, spleen, kidneys, heart, and brain is shown in **Figure 5.7A**. As expected, maximum SPION accumulation was observed in the liver followed by the spleen, with negligible accumulation in the kidneys, brain, and heart (for all mice).

A comparison of the two analytical methods (MSOT and EPR) used to quantify SPION concentrations was made. EPR and terminal MSOT measurements in the liver, spleen, and kidneys were normalized for each animal relative to the liver signal (**Figure 5.7B**). Both EPR and MSOT confirmed maximum SPION accumulation (per unit weight) in the liver of all tested animals; nearly half as much SPION accumulation (per unit weight) in the spleen; and negligible SPION accumulation in the kidneys. Despite an excellent agreement in terms of the fit, the absolute quantitative values generated by EPR and MSOT differed significantly (**Figure 5.7C**). The corrected MSOT signal intensities were converted to SPION concentrations using the standard curves created from the phantom studies. In this case, a human breast-mimicking phantom was used, with absorption and scattering properties that could differ significantly from those of the animal's liver and spleen. The different slopes of the liver and spleen linear fit also indicate that their properties might differ as well. Future studies should include multiple phantom gels that better replicate the sound and optical properties of the different tissues in the animal.

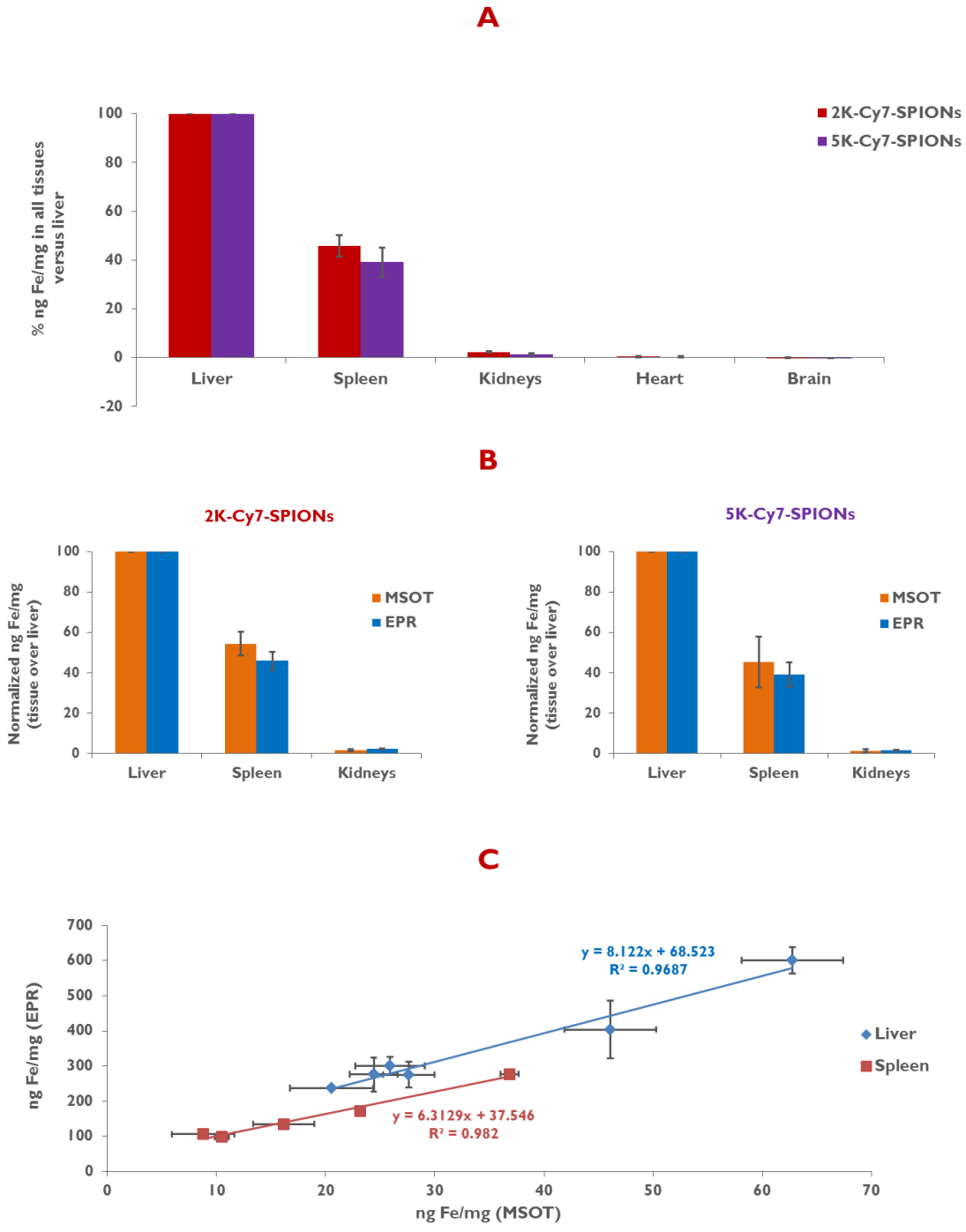

Figure 5.7 A. *Ex vivo* quantification of SPION accumulation using EPR. **B.** Comparison between EPR and MSOT (normalized for liver signal) for 2K and 5K-Cy7-SPION accumulation in the liver, spleen, and kidneys. **C.** Quantitative comparison between EPR and MSOT.

5.4 Conclusion

MSOT was used to non-invasively track, with high spatial and temporal resolution, the removal of PEGylated Cy7-SPIONs from circulation and its time-resolved accumulation in organs of elimination. This form of pK modeling reduces the total number of tested animals significantly compared to other pK quantification techniques. The quantitative feature of MSOT was also validated in this study through direct comparison with EPR.

The plasma half-life ($t_{1/2}$) was measured by spectral unmixing of the signal around the jugular vein. Results indicated that the plasma half-life ($t_{1/2}$) of 2K-Cy7-SPIONs was significantly longer than the $t_{1/2}$ of 5K-Cy7-SPIONs. While both SPIONs were cleared fast ($t_{1/2}$ < 10 min), the majority of SPIONs were cleared by the liver and spleen, which make it excellent for macrophage imaging in inflammation sites. However, due to its rapid clearance from circulation, the developed probe is unlikely to be effective for tumor targeting applications that rely on the passive targeting of the tumor interstitium. Various strategies could be employed to enhance the pK properties of this probe, such as increasing the PEG to Cy7 ratio on the surface of SPIONs. While this strategy will diminish the optoacoustic properties of the probe, the reaction conditions need to be optimized to ensure that the optoacoustic properties remain within reasonable detection limits.

Chapter 6 Development of MMP-2 responsive SPIONs

6.1 Introduction

Proteases are a group of evolutionarily conserved enzymes that regulate various biological processes such as gene expression, apoptosis, proliferation, angiogenesis, invasion and migration [83,183]. The activity of proteases is strictly regulated by protease signaling pathways, and dysregulation can cause pathologies such as cancer, neurodegenerative diseases, and immune disorder [37,65,70]. Proteases are heavily involved in tumor progression at the primary and metastatic sites [28]. They degrade multiple components of the extracellular matrix, release growth factors and chemokines and activate latent proteins on the cell membrane [34]. Proteases are classified into six groups depending on the mechanism of catalysis: aspartic, cysteine, glutamic, metalloproteases, serine, and threonine proteases [183]. The activity of matrix metalloproteinases (MMPs), a family of extracellular, zinc-dependent proteins involved in extracellular matrix remodeling, increases significantly in many types of cancers [35,36,184]. MMPs are active participants in all the major hallmarks of tumorigenesis, including proliferation, apoptosis, angiogenesis and metastasis [7,185,186]. It's been shown that the expression of MMP-2, one of the key members of the MMP family, correlates with tumor aggressiveness in prostate [5,6], brain [7], and non-small cell lung cancer [9]. The purpose of this study was to create an MMP-2 responsive probe (MSP-PEG-SPIONS) to quantify MMP-2 expression. The selectivity of the probe towards MMP-2 was assessed versus other MMPs (MMP-7, 8, 9, 13 and 14) and other tumor-associated proteases (cathepsin B, caspase 3, 6, and 8, legumain and trypsin). In addition, the selectivity of MSP-PEG-SPIONs towards

MMP-2 was compared to MSCRP-PEG-SPIONs (carrying the scrambled peptide GVRLGPGC) and MSP2-PEG-SPIONs (carrying a second MMP-2 specific peptide GGPRQITAGC). Last, the stability of the probe was assessed in biological media by monitoring peptide hydrolysis in 100% FBS and cell culture media.

6.2 Materials and methods

6.2.1 Materials

100 nm starch-coated, fluidMAG-D superparamagnetic iron oxide nanoparticles (SPIONs) were purchased from Chemicell GmbH. 2 kDa succinimidyl PEG NHS (2K mPEG-NHS) was purchased from Nanocs. Eagle's Minimum Essential Medium (EMEM) was purchased from the American Type Culture Collection (ATCC). Hydrochloric acid, glycerol, and dimethyl sulfoxide (DMSO) were purchased from BDH Chemicals. Sodium Chloride, calcium chloride anhydrous, potassium phosphate monobasic anhydrous, sodium phosphate dibasic heptahydrate, sodium phosphate monobasic monohydrate, sodium acetate, chaps, EDTA, and TRIS were purchased from Amresco. Bovine serum albumin (BSA) and 4-Aminophenylmercuric acetate (APMA) were purchased from Sigma Aldrich. Brij 35 was purchased from Spectrum Chemical. Zinc chloride and HEPES were purchased from Alfa Aesar. Ac-DEVD –pNA , (Z - Arg)2Rh110 • 2HCl, 390 MMP FRET substrate III (Mca-PLA-Nva-Dpa-AR–NH2), 520 MMP FRET substrate III (QXL® 520 -PLGC(Me)HAr-K(5 - FAM)-NH2), Human MMP-2, MMP-7, MMP-8, MMP-13, and MMP-14 were purchased from Anaspec. Defined trypsin inhibitor was purchased from Gibco. Dithiothreitol (DTT) was purchased from TCI. FAM-GPLGVRGC-amide, FAM-GVRLGPGC-amide, and FAM-GGPRQITAGC-amide were purchased from LifeTein. Sulfosuccinimidyl 4-(N-maleimidomethyl) cyclohexane-1-carboxylate (Sulfo SMCC) and Ellman's reagent were purchased from Thermo Scientific. GM 6001 (Galardin) and MMP-9 proenzyme were purchased from CalbioChem. Trypsin was purchased from Ward's Science. Cathepsin B, Caspase-3, 6 and 8 were purchased from BioVision. Legumain was purchased from Novoprotein.

6.2.2 Synthesis, characterization and optimization of MMP-2 responsive SPIONs

Two methods of conjugation and varying SMCC to PEG ratio

Two different methods were used to conjugate the MMP-2 responsive peptide-dye (FAM-GPLGVRGC-amide) to the surface of SPIONs. In method 1, a 30:70 and 50:50 mixtures of sulfo SMCC and 2K mPEG-NHS were added to aminated SPIONs (1211.7 mg Fe/mL in pH 7.4 phosphate buffer) at a 1:2 NHS to amine ratio. DMSO was added at a 25% V/V ratio. Both mixtures were incubated for 3.5 hours at room temperature and then centrifuged twice at 14,000 RPM to remove excess unreacted PEG and SMCC. Afterward, both solutions were mixed with FAM-GPLGVRGC-amide at a 1:2.5 peptide to SMCC ratio in 0.1M phosphate buffer and incubated overnight at room temperature. The functionality of the thiol group was confirmed with the Ellman's assay (described below). The excess unreacted peptide was removed with magnetic separation.

In method 2, FAM-GPLGVRGC-amide was mixed with sulfo SMCC in pH 7.4 phosphate buffer (3:1 peptide to SMCC ratio) for 2.5 hours at room temperature. The solution was then split into two equal fractions, and 2K mPEG-NHS was added either at a 30:70 or 50:50 SMCC to PEG ratio. The solutions were incubated overnight and then placed on a magnetic separator to remove excess unreacted moieties.

Varying Peptide to SMCC ratio

The procedure was similar to method 1 explained above (30:70 SMCC to PEG ratio). In this case, three different peptide to SMCC ratios (1.8:1, 1:2.5 and 1:8) were added to SMCC-PEG-SPIONs. All supernatants were collected for further analysis.

Characterization of SPIONs

The particle size, polydispersity index (PDI) and zeta potential were measured by dynamic light scattering (Malvern Zetasizer Nano ZS; Malvern, UK).

Ellman's assay

Ellman's assay was used to confirm the activity of thiol group on the cysteine amino acid of all peptides. Briefly, 5 μL Ellman's reagent (4 mg/mL in a reaction buffer consisting of 0.1M sodium phosphate buffer, pH 8.0, 1 mM EDTA) was mixed with 275 μL of the peptide (0.1 mM in reaction buffer) and incubated for 15 minutes at room temperature. The control consisted of 5 μL reaction buffer (without Ellman's reagent) mixed with 275 μL of 0.1 mM peptide. 200 μL were transferred to a 96 well plate and its absorbance measured at 412 nm.

6.2.3 Synthesis and characterization of MSP-PEG-SPIONs

Synthesis procedure

A 50:50 mixture of sulfo SMCC and 2K mPEG-NHS was added to aminated SPIONs (1540.2 nmol NH2/mg Fe in pH 7.4 phosphate buffer) at a 1:2 NHS to amine ratio. DMSO was added at a 25% V/V ratio. The solution was incubated for 3.5 hours at room temperature, then centrifuged twice at 14,000 RPM to remove excess unreacted PEG and SMCC. Afterward, FAM-GPLGVRGC-amide (in 0.1M phosphate buffer) was added the solution at a 1:5 peptide to SMCC ratio, incubated overnight at room temperature, then placed on a magnetic separator to remove excess unreacted moieties. The solution was labeled MSP-PEG-SPIONs.

In addition, a scrambled version of the MMP-2 specific peptide (FAM-GVRLGPGC-amide), as well as a second MMP-2 specific peptide with a different amino acid sequence (FAM-GGPRQITAGC-amide), were conjugated to the surface of aminated SPIONs using the same

procedure described above, and labeled MSCRP-PEG-SPIONs and MSP2-PEG-SPIONs, respectively.

Physiochemical characterization of SPIONs

During the synthesis procedure, all supernatants, which contained unreacted Cy7, were collected after each wash. The concentration of peptide on the surface of SPIONs (nmol peptide/mg Fe) was calculated by measuring the fluorescence value of the supernatants at 495/525. A standard curve was also generated for fluorescence intensity of FAM-GPLGVRGC in the 0 to 90 µM concentration range. The surface density (S) of FAM-GPLGVRGC was then calculated using equation 6.1.

$$S = \frac{\#\ of\ Cy7\ molecules}{Average\ \#\ of\ nanoparticles\ (n)} \qquad Eq.\ 6.1$$

The average number of nanoparticles (n) and the number of Cy7 molecules in 1 g iron were calculated using equations 6.2 and 6.3:

$$n = \frac{6m}{\pi D^3 \rho} \qquad Eq.\ 6.2$$

$$Cy7 \quad molecules = \frac{nmol\ Cy7}{mg\ Fe} * \frac{1000\ mg\ Fe}{1\ g\ Fe} * \frac{1\ mol}{10^9 nmol} * \frac{6.022 * 10^{23} molecules}{mol} \qquad Eq.\ 6.3$$

Where m is the nanoparticle weight, D is the nanoparticle-based mean diameter, and ρ is the density of SPIONs, equal to ~1.1 g/cm^3.

6.2.4 Measuring proteolytic activity using FRET peptides

MMPs

The activity of MMPs in different buffers (**Table 6.1**) was tested. Pro-MMPs were activated by incubating the proteases with APMA for 2 hours at 37 ºC. Afterward, MMPs were mixed with either 390 or 520 MMP FRET substrates, and fluorescence intensity was monitored at 325/393 nm for the 390 FRET substrate or at 495/525 nm for the 520 FRET substrate. The i. MMP to APMA and the ii. MMP to substrate molar ratios used in this experiment are reported in **Figure 6.4**. The effect of varying the MMP to APMA ratio was also examined for all MMPs. MMPs were incubated with different amounts of APMA in buffer D for 2 hours at 37 ºC, mixed with either 390 or 520 MMP FRET substrate, and the fluorescence intensity was monitored over time. The exact MMP to APMA molar ratios are reported in **Figure 6.5**.

Finally, the effectiveness of Galardin as an MMP inhibitor was tested for all MMPs. Galardin was added to active MMPs in buffer D and incubated for 5 minutes, mixed with either 390 or 520 MMP FRET substrate, and the fluorescence intensity was monitored over time. The Galardin to MMP ratio was equal to 0.025 (μM Galardin/nM MMP) for MMPs 7, 13 and 14 (**Figure 6.5**), while different molar ratios were tested for MMP-2 and 9 (**Figure 6.6**).

Caspases, Trypsin and cathepsin B

The activities of caspase 3, 6, and 8 were tested against the substrate Ac - DEVD – pNA (Anaspec). 1 unit of each caspase was mixed with 25 μM of caspase substrate) in caspase buffer (**Table 6.3**), and absorbance was monitored at 408 nm.

The activity of trypsin was measured by mixing two different volumes (4 or 20 µL) of a 0.5 µM trypsin solution (equivalent to 2 or 10 pmol) with 100 µL of a 50 µM (Z - Arg)2Rh110 • 2HCl substrate in trypsin buffer (**Table 6.3**). Various amounts of defined trypsin inhibitor (1X) were added (**Figure 6.7B**), and fluorescence intensity was monitored at 495/525 nm.

The activity of cathepsin B was tested against (Z - Arg)2Rh110 • 2HCl substrate. 0.01 µM and 0.083 µM Cathepsin B were mixed with 25 µM substrate in Cathepsin B buffer (**Table 6.3**), and fluorescence intensity was monitored at 495/525 nm. The concentration of cathepsin B was increased to 0.383 µM after 134 minutes, and fluorescence was monitored for another 112 minutes.

Table 6.1 List of MMP buffers that were used to test the activity of MMPs against MMP FRET substrates.

MMP buffer label	Components
Buffer A	50 mM TRIS-HCl, pH 7.5, 150 mM NaCl, 10 mM CaCl2, and 1 mg/mL BSA Solution
Buffer B	50 mM TRIS-HCl, pH 7.5, 150 mM NaCl, 10 mM CaCl2, 1 mg/mL BSA and 0.05% Brij
Buffer C	50 mM TRIS-HCl, pH 7.5, 150 mM NaCl, 10 mM CaCl2, 1 mg/mL BSA Solution , 0.05% Brij and 1 µM ZnCl2
Buffer D	50 mM TRIS-HCl, pH 7.5, 150 mM NaCl, 10 mM CaCl2, and 0.05% Brij-35
Buffer E	MMP dilution buffer from sensolyte plus 520 assay kit (Anaspec); Components are unknown

6.2.5 Hydrolysis of MSP-PEG-SPIONs by proteases

Rate of hydrolysis of MSP-PEG-SPIONs by MMP-2 at different times

0.64 pmol MMP-2 was activated (4 nM MMP-2/mM APMA molar ratio) for 2 hours at 37 ºC, mixed with 0.02 mg Fe of MSCRP-PEG-SPIONs in MMP buffer D (n=5). 23.6 pmol of the MMP inhibitor Galardin was then added to the five tubes at different times (2, 5, 12, 25 and 40 min). The control consisted of all the above components except for MMP-2. All samples were centrifuged for 15 minutes at 14,500x g inside a 10K Nanosep centrifugal device (PALL Life Sciences) to separate the hydrolyzed peptide-dye from SPIONs. 200 µL of the supernatants were transferred to a 96 well plate and its fluorescence intensity measured at 495/525 nm using a microplate reader.

Initial rate of hydrolysis of MSP-PEG-SPIONs by all proteases

The optimum APMA concentrations for activating MMPs are listed in **Table 6.4**. 0.32 pmol of active MMP-2, 8, 9 and 13, 0.64 pmol of active MMP-7, 0.768 pmol of active MMP-14, 6.4 pmol of trypsin, 6.4 pmol cathepsin B, 0.32 pmol of caspase 3, 6, and 8, and 0.32 pmol legumain (activated in legumain buffer for 2 hours at 37 ºC) were incubated with 0.02 mg Fe of MSCRP-PEG-SPIONs for 10 minutes. A control was included for each buffer used (excludes proteases). All samples were then centrifuged for 15 minutes at 14,500x g inside a 10K Nanosep centrifugal device (PALL Life Sciences) to separate hydrolyzed peptide-dye from SPIONs. 200 µL of the supernatants were transferred to a 96 well plate and the fluorescence intensity was measured at 495/525 nm. The initial rate of hydrolysis by MMP-2 was also tested for MSP2-PEG-SPIONs and MSCRP-PEG-SPIONs under the same conditions described above.

Michaelis-Menten kinetics

The above experiment was repeated at different substrate (MSP-PEG-SPIONs) concentrations for MMP-2, 7, 8, 9, and 13. The selected concentrations were 0.02, 0.01, 0.004 and 0.0015 mg Fe of MSP-PEG-SPIONs, which correspond to 7.81, 3.90, 1.56 and 0.586 μM FAM-GPLGVRGC peptide. The Michaelis-Menten equation was then fitted into the data, according to equation 6.4:

$$V_o = \frac{V_{max}[S]}{K_m + [S]} \qquad Eq.\,6.4$$

$$k_{cat} = \frac{V_{max}}{[E]_o} \qquad Eq.\,6.5$$

Where V_o is the initial rate of reaction, $[S]$ is the substrate concentration, V_{max} is the maximum rate of reaction, K_m is the Michaelis constant, $[E]_o$ is the enzyme concentration, and k_{cat} is the turnover number. Nonlinear regression was used to calculate V_{max} and K_m as well as the error for both parameters. Propagation of error was then used to calculate the error of k_{cat}/K_m.

6.2.6 Peptide release in 100% FBS and HT-1080 culture media

MSP-PEG-SPIONs, MSP2-PEG-SPIONs, and MSCRP-PEG-SPIONs were incubated separately with 100% FBS and with complete culture media (EMEM + 10% FBS+ 1% antibiotics). The rate of peptide hydrolysis was monitored by measuring the change in fluorescence intensity at 495/525 nm over time.

6.2.7 Statistical analysis

All measurements were conducted in triplicates. Data are presented as mean ± S.D., and p values were calculated using the student's t-test.

6.3 Results and Discussion

6.3.1 Synthesis, characterization and optimization of MMP-2 responsive SPIONs

Two different methods were used to generate MM2-responsive SPIONs, which consist of an iron oxide core, 2K-PEG chains, and an MMP-2 specific peptide-dye conjugate (FAM-GPLGVRGC-amide) linked to SMCC (**Figure 6.1A**). SMCC is a bifunctional crosslinker with amine-reactive NHS and thiol-reactive maleimide groups on both ends of the molecule. In method 1, NHS chemistry was used to conjugate both mPEG-NHS and SMCC to the surface of SPIONs, followed by centrifugation to remove excess unreacted PEG and SMCC. Maleimide chemistry was then used to chemically attach the thiol-containing peptide-dye conjugate to the maleimide group on the other end of SMCC. In method 2, maleimide chemistry was first used to link the peptide-dye conjugate to SMCC. SMCC-peptide-dye and mPEG-NHS were then mixed with aminated SPIONs. Two different SMCC to PEG ratios were attempted for both methods. **Figure 6.1C** indicates that method 1 generated significantly smaller SPIONs with significantly smaller PDI values (at both SMCC to PEG ratios) compared to method 2. Therefore, method 1 was selected as the method of choice. In addition, there was no significant difference between the hydrodynamic diameter, PDI (both were mono-modally dispersed), and zeta potential of 30% SMCC-SPIONs versus 50% SMCC-SPIONs (**Figure 6.2B i-iii**) generated with method 1. As expected, 50% SMCC-SPIONs contained 74.4% extra peptide-dye on their surface compared to 30% SMCC-SPIONs (**Figure 6.2B iv)**. SMCC and PEG compete for the same available amine groups, thus the addition of extra SMCC (and less PEG) generates additional sites for peptide conjugation.

The effect of varying the peptide to SMCC ratio was then assessed for 30% SMCC-SPIONs. The addition of 1.8:1, 1:2.5 and 1:8 peptide to SMCC ratios generated SPIONs with

similar peptide concentrations on their surface (**Figure 6.2C**). Therefore, the peptide amount was already at saturation level even at the lowest peptide concentration. It must be noted that a 1:8 peptide to SMCC ratio refers to the starting SMCC concentration and not the leftover SMCC concentration on the surface of SPIONs. SMCC was initially added to aminated SPIONs, and excess SMCC were washed away, leaving only the conjugated SMCC molecules behind at a concentration that is likely to be significantly smaller than the starting amount.

The objective of this study was to optimize the protocol for synthesizing MMP-2 SPIONs. The selected parameters are as follows: i. Use method 1 of synthesis, ii. Add SMCC and PEG at a 50:50 molar ratio, and iii. Add peptide at a 1:5 peptide to SMCC ratio.

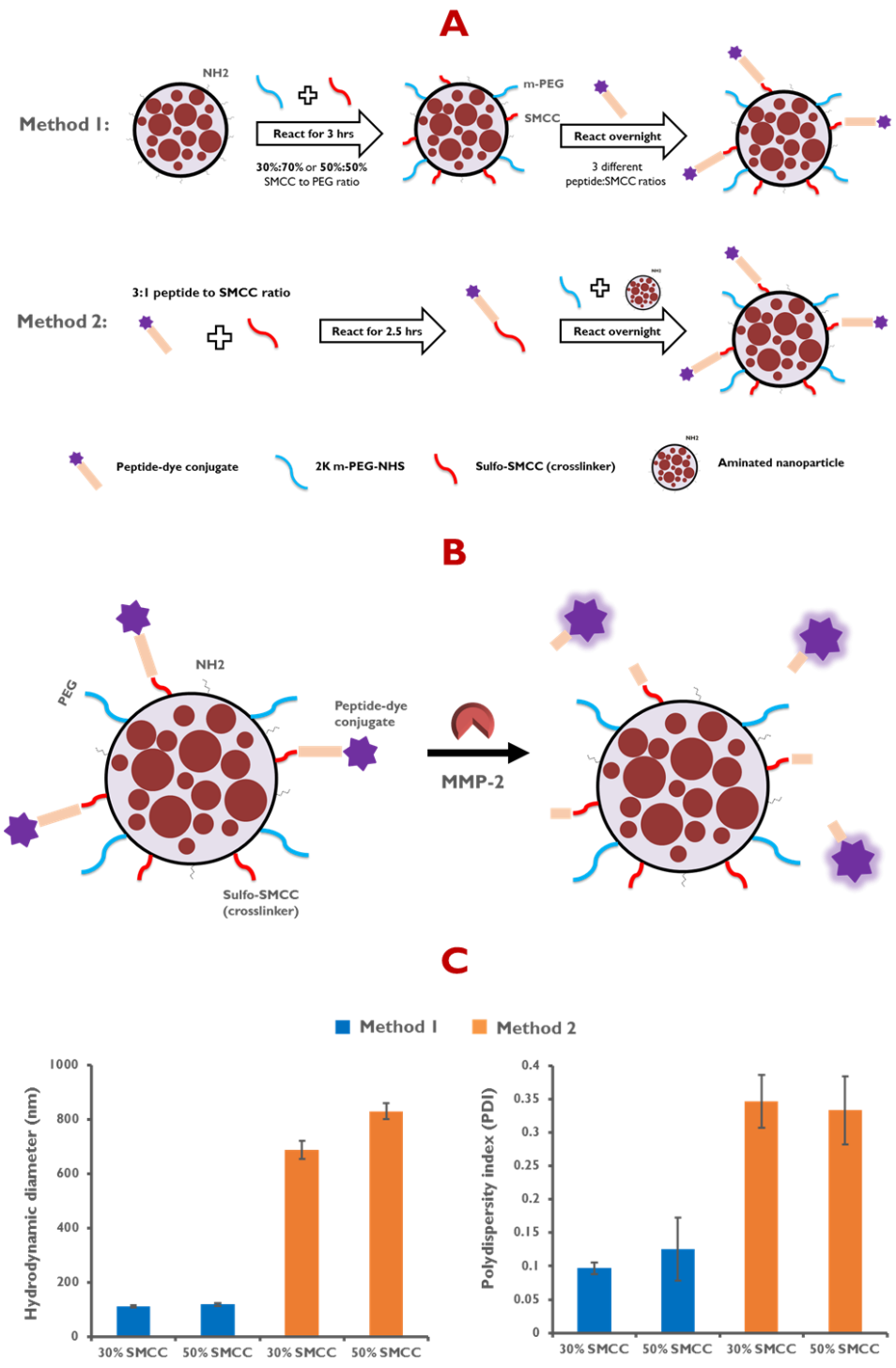

Figure 6.1 A. Reaction scheme for generating MMP-2 responsive SPIONs. **B.** Peptide hydrolysis in the presence of MMP-2. **C.** The effect of varying the method of conjugation and the starting SMCC: PEG ratio on size and PDI.

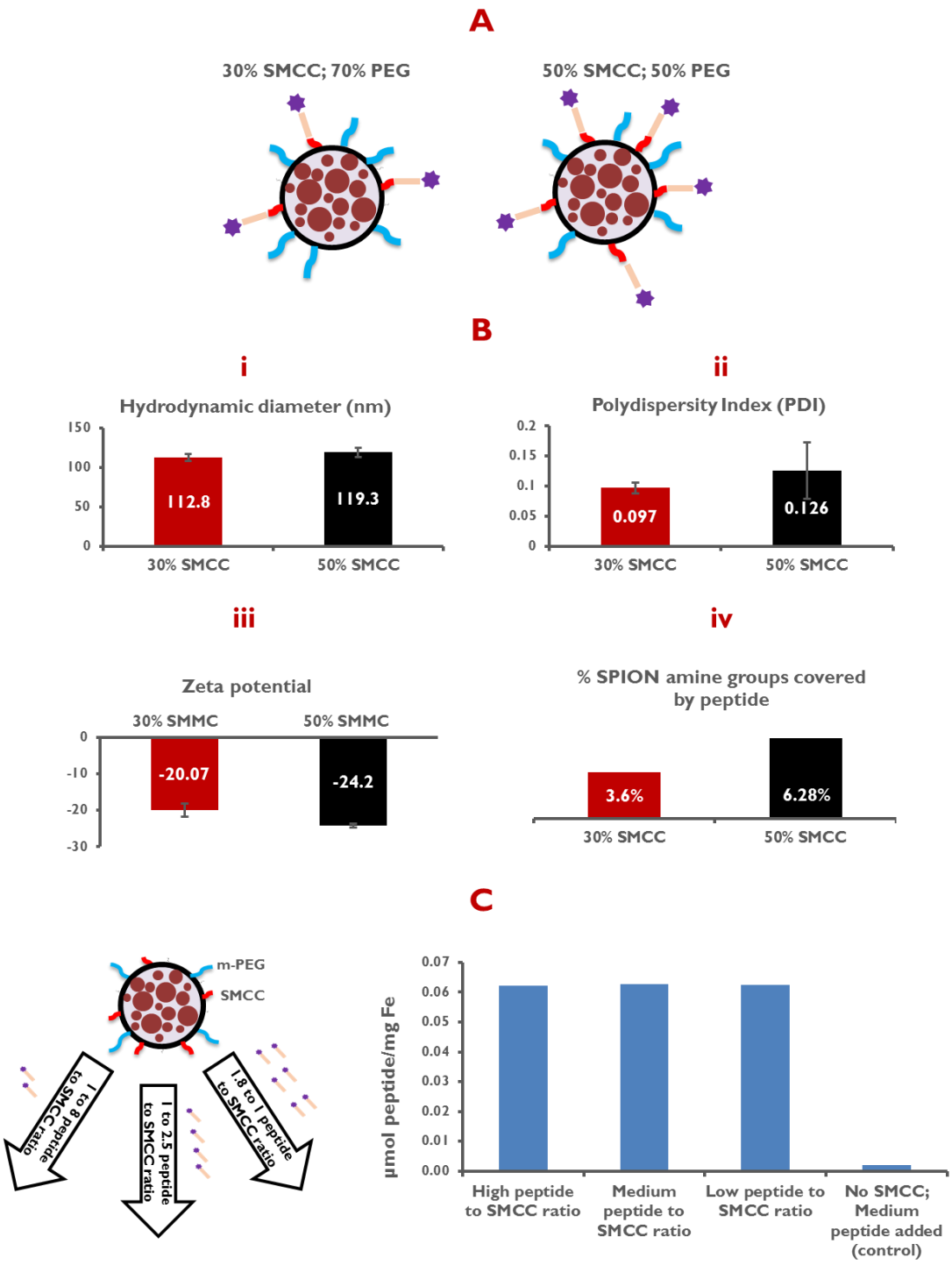

Figure 6.2 Optimizing the conjugation of MMP specific peptide to SPIONs. **A.** Two structures with different SMCC: PEG ratios **B.** Effect on size, PDI, zeta potential and surface coverage. **C.** Effect of varying peptide: SMCC ratio on surface coverage.

6.3.2 Synthesis and characterization of MSP-PEG-SPIONs

MMP-2 responsive SPIONs, labeled MSP-PEG-SPIONs, were synthesized using conjugation method #1 with 50%:50% SMCC to PEG molar ratio. The physiochemical properties of aminated and MSP-PEG-SPIONS are listed in **Table 6.2**. The decrease in hydrodynamic diameter from the aminated to the PEGylated state is due to the dispersion of larger SPION aggregates that exist in the aminated state to smaller aggregates following PEGylation. This process also creates SPIONs with a broader size distribution, as evidenced by an increase in PDI from 0.12 (aminated) to 0.18 (MSP-PEG-SPIONS). The zeta potential of aminated SPIONs is highly positive due to the presence of protonated amine groups at neutral pH. The addition of neutral PEG and negatively charged FAM-GPLGVRGC creates negatively charged MSP-PEG-SPIONs in water.

Table 6.2 Physiochemical properties of Aminated and MSP-PEG-SPIONs.

	Hydrodynamic diameter (nm)	**PDI**	**Zeta Potential**	**% peptide conjugation efficiency**	**nmol peptide/mg Fe**	**% coverage of NH_2 groups by peptide**	**Peptide surface density (S)**
Aminated SPIONs (1540.2 nmol NH_2/mg Fe)	139.43 ± 2.83	0.12 ± 0.01	34.47 ± 1.19	–	–	–	–
MSP-PEG-SPIONs	96.13 ± 1.53	0.18 ± 0.02	-21.70 ± 0.66	74.781	98.3	6.383	30287.43

Two additional SPION configurations were synthesized, one containing a scrambled version of the first MMP-specific peptide (labeled MSCRP-PEG-SPIONs), and the other containing a second commonly-used MMP-2 specific peptide with the sequence FAM-GGPRQITAGC-amide (labeled MSP2-PEG-SPIONs). It must be noted that a different batch of aminated SPIONs (albeit very similar to the first one) was used to generate MSCRP-PEG-SPIONs

and MSP2-PEG-SPIONs. Overall, the amount of conjugated peptide was similar for all three SPION configurations (**Tables 6.2 and 6.3**).

Table 6.3 Quantifying nmol peptide/mg Fe and % coverage of amine groups by peptide for MSP2-PEG-SPIONs and MSCRP-PEG-SPIONs.

	% peptide conjugation efficiency	**nmol peptide/mg Fe**	**% coverage of NH_2 groups by peptide**
Aminated SPIONs (1625.2 nmol NH_2/mg Fe)	–	–	–
MSP2-PEG-SPIONs	74.42	76.3	4.696
MSCRP-PEG-SPIONs	88.95	91.2	5.612

6.3.3 Proteolytic activity on FRET peptides

Pro-MMPs (inactive form) require activation by APMA. The activity of MMPs depends on the type of buffer used and the concentration of APMA. The optimum buffer was determined by mixing active MMP-2, 7, 8, 9, 13 or 14 with either a 390 MMP FRET substrate or 520 MMP FRET substrate (Anaspec) in different buffer solutions. The FRET substrate consists of a donor dye and a quencher on both ends of the MMP-specific peptide sequence (**Figure 6.3)**, and proteolytic cleavage of the substrate by MMP causes a change in the fluorescence signal that can be tracked with a microplate reader (**Figure 6.4**). All MMPs displayed maximum activity in buffer D, (50 mM TRIS-HCl, pH 7.5, 150 mM NaCl, 10 mM CaCl2, and 0.05% Brij-35). The composition of all the other buffers used is shown in **Table 6.1**.

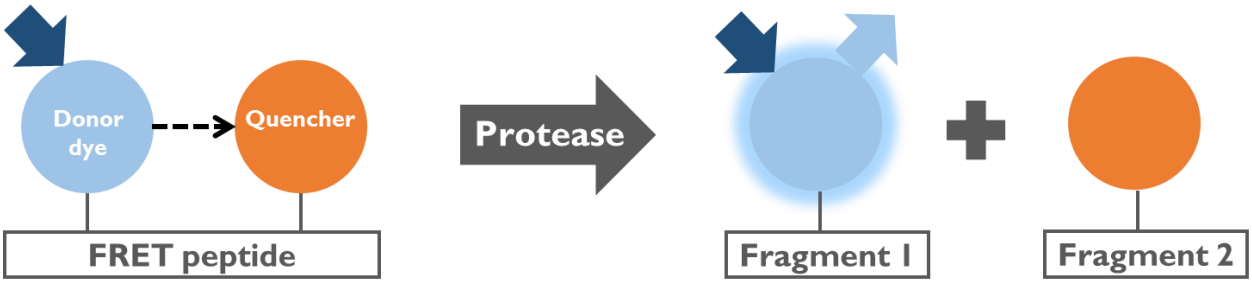

Figure 6.3 FRET peptides are used to test the activity of proteases and determine the optimum reaction conditions before incubation with MMP-responsive SPIONs.

The optimum APMA concentration was also measured for the different MMPs (**Figure 6.5 and Table 6.4**). It is interesting to note that the activity of MMPs increased with increasing APMA concentrations up to a certain point, then started to decrease when adding additional APMA. The optimum APMA to MMP ratios were used in the remainder of the studies. Finally, the effectiveness of Galardin as an MMP inhibitor was confirmed (**Figure 6.5** for MMP-7, 13 and 14, and **Figure 6.6** for MMP-2 and 9).

The activities of caspase 3, 6, and 8 were confirmed by incubating the proteases with a commercial caspase substrate (Ac - DEVD – pNA) and monitoring absorbance at 408 nm. The activity of trypsin and cathepsin B were also confirmed by incubating them with (Z - Arg)2Rh110 • 2HCl substrate and monitoring fluorescence at 495/525 nm. Results are shown in **Figure 6.7**.

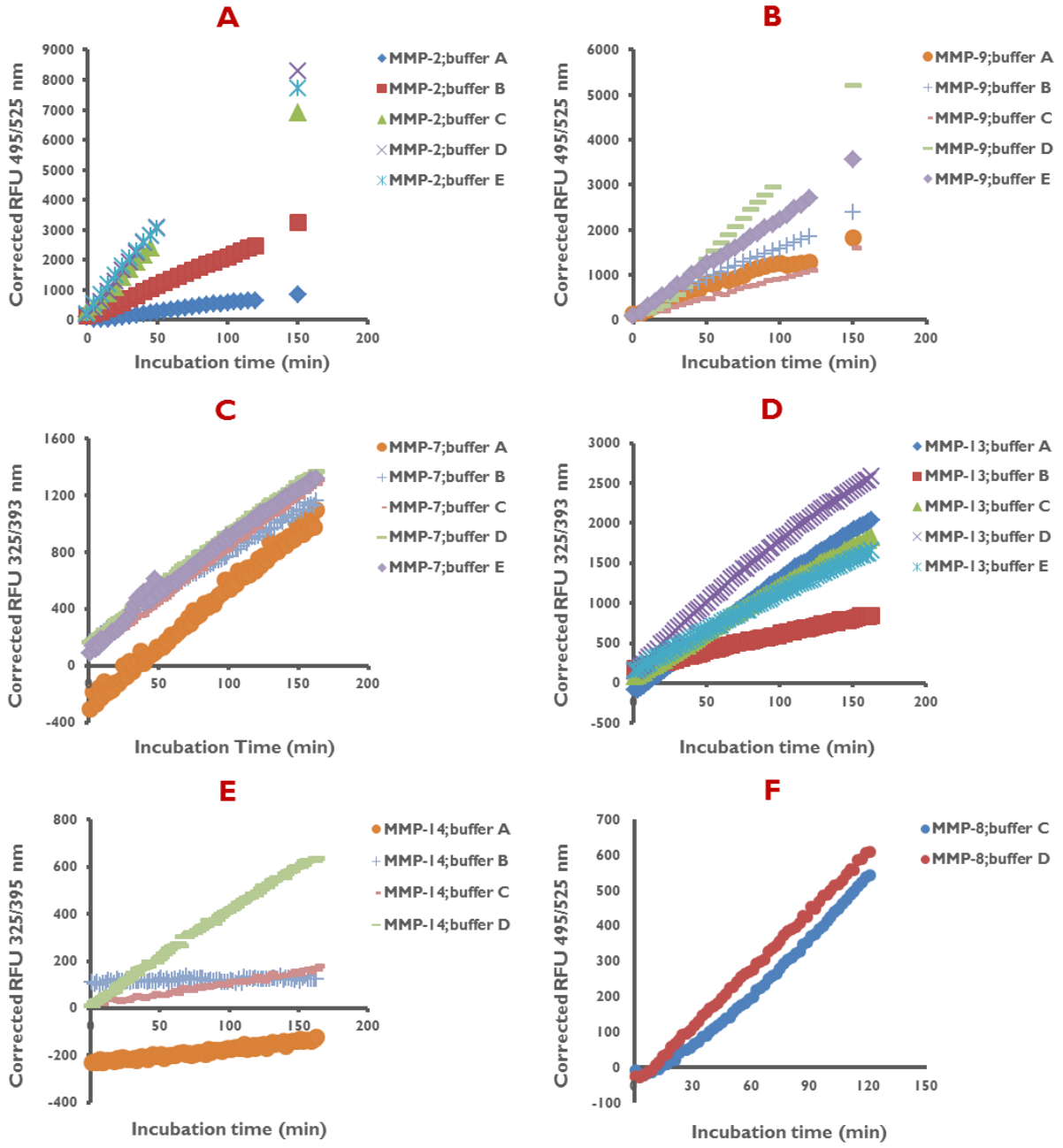

Figure 6.4 Testing the activity of different MMPs in different buffer solutions: **A.** 1.285 nM MMP-2 on 2.5 µM 520 FRET substrate (2.8 nM MMP-2/mM APMA), **B.** 3 nM MMP-9 activity on 2.5 µM 520 FRET substrate (1.13 nM MMP-9/mM APMA), **C.** 1.285 nM MMP-7 activity on 3.75 µM 390 FRET substrate (2 nM MMP-7/mM APMA), **D.** 1.285 nM MMP-13 activity on 3.75 µM 390 FRET substrate (10 nM MMP-13/mM APMA), **E.** 1.285 nM MMP-14 activity on 3.75 µM 390 FRET substrate (2 nM MMP-7/mM APMA) and **F.** 1.285 nM MMP-8 activity on 1.25 µM 520 FRET substrate (10 nM MMP-8/mM APMA).

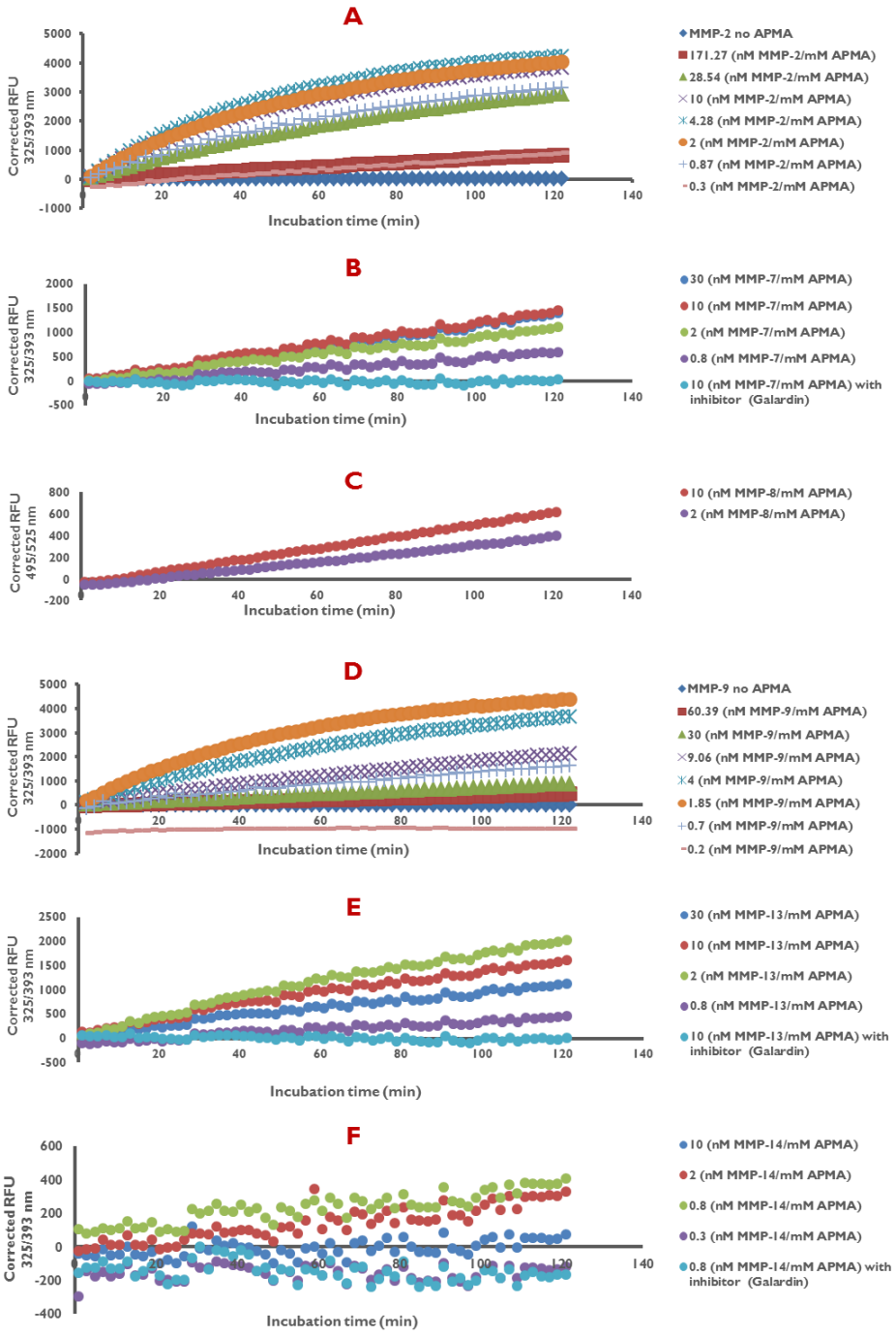

Figure 6.5 Testing the effect of varying APMA concentration on the activity of MMPs. **A.** 1.285 nM MMP-2 activity on 3.75 µM 390 FRET substrate. **B.** 1.285 nM MMP-7 activity on 3.75 µM 390 FRET substrate. **C.** 1.285 nM MMP-8 activity on 1.25 µM 520 FRET substrate. **D.** 3 nM MMP-9 activity on 3.75 µM 390 FRET substrate. **E.** 1.285 nM MMP-13 activity on 3.75 µM 390 FRET substrate. **F.** 1.285 nM MMP-14 activity on 3.75 µM 390 FRET substrate.

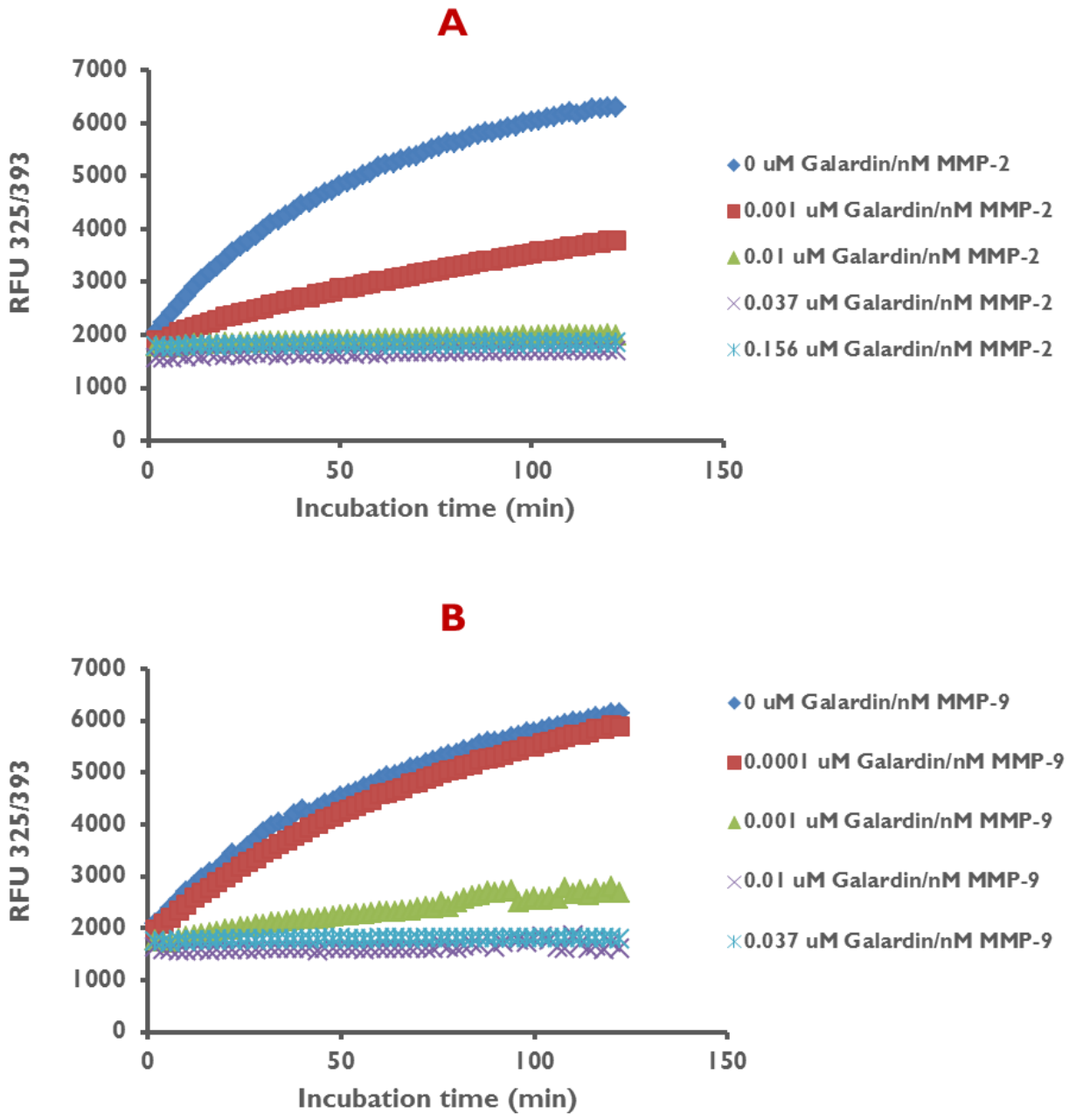

Figure 6.6 Testing the effect of adding an MMP inhibitor Galardin on the activity of MMP-2 and 9. **A.** 1.285 nM MMP-2 activity on 3.75 µM 390 FRET substrate. **B.** 3 nM MMP-9 activity on 3.75 µM 390 FRET substrate.

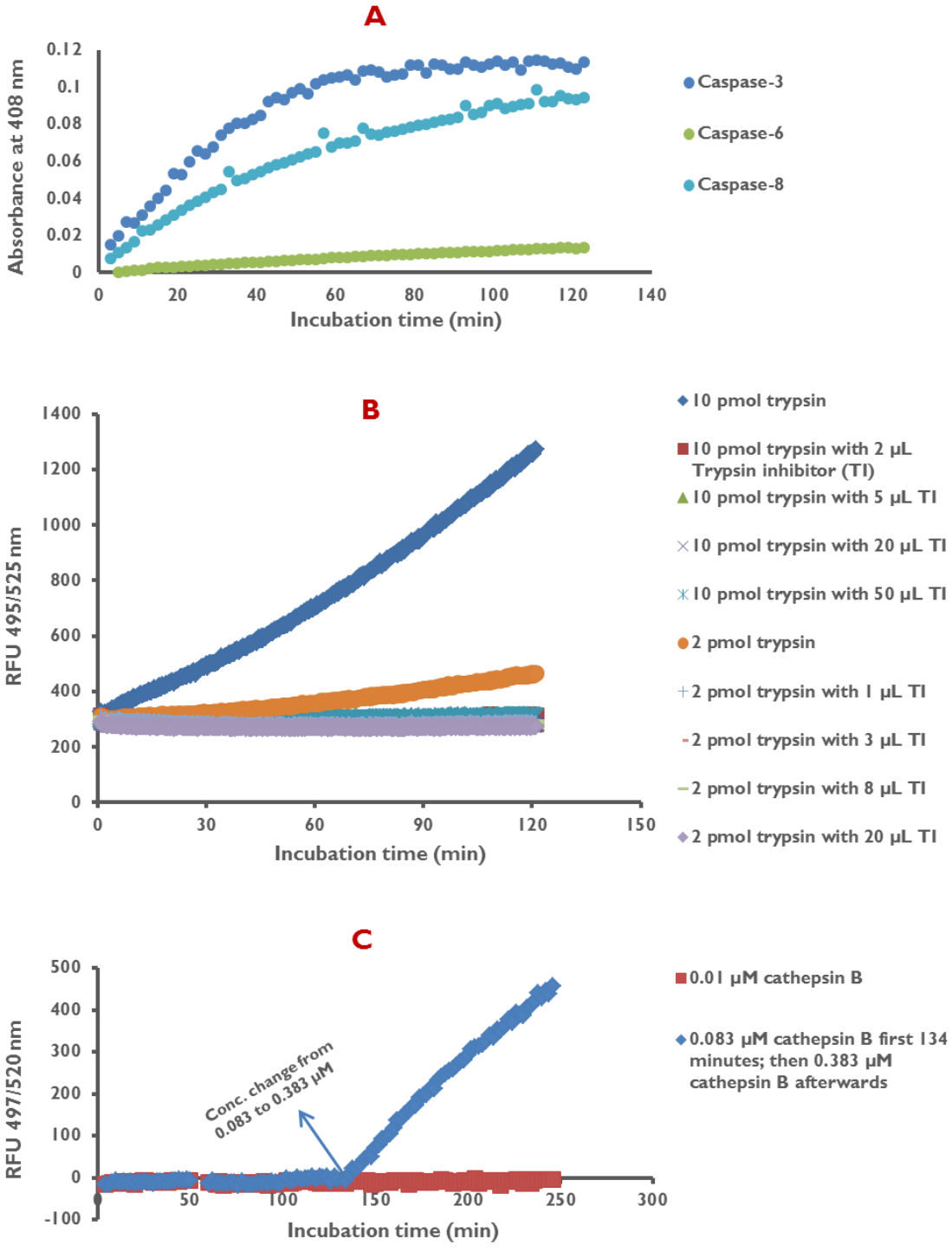

Figure 6.7 Testing the activity of Caspases, trypsin and cathepsin B. **A.** 1 unit caspase activity on 25 µM caspase substrate. **B.** Trypsin activity on 25 µM (Z - Arg)2Rh110 • 2HCl substrate. **C.** Cathepsin B activity on 25 µM (Z - Arg)2Rh110 • 2HCl substrate.

6.3.4 Hydrolysis of MSP-PEG-SPIONs by proteases

The specificity of MMP-2 towards MSP-PEG-SPIONs was compared against other MMPs. As shown in **Figure 6.8A**, the rate of hydrolysis of FAM-GPLGVRGC-amide (pmol peptide hydrolyzed/min) on the surface of MSP-PEG-SPIONS by MMP-2 (169.59 ± 16.32) was significantly higher than the rate of cleavage by MMP-7 (11.91 ± 1.39, $p < 0.01$), MMP-8 (42.25 ± 14.82, $p < 0.01$), MMP-9 (61.90 ± 10.00, $p < 0.01$), MMP-13 (48.27 ± 2.31, $p < 0.01$), and MMP-14 (-1.61 ± 3.28, $p < 0.01$). In addition, the rate of hydrolysis of MSP-PEG-SPIONS by non-MMP proteases was negligible (< 2 pmol peptide hydrolyzed/min for all non-MMP proteases). Results are shown in **Figure 6.8B**.

In addition, MMP-2 showed negligible activity towards MSCRP-PEG-SPIONs carrying the scrambled peptide FAM-GVRLGPGC-amide (-2.36 ± 1.46 pmol peptide hydrolyzed/min), and significantly lower activity towards MSP2-PEG-SPIONs carrying the second MMP-2 peptide FAM-GGPRQITAGC-amide (102.32 ± 7.01 pmol peptide hydrolyzed/min, $p < 0.01$) compared to MSP-PEG-SPIONs (**Figure 6.10A**).

The Michaelis-Menten kinetics of MMP-2, 7, 8, 9, and 13 against MSP-PEG-SPIONS were tested. **Figure 6.9A** shows the rate of peptide release per pmol MMP-2 at different time points. Data shows that there was a linear increase in peptide hydrolysis over the first 12 minutes, which indicates that the initial rate of release can be calculated by inhibiting the reaction anytime over the first 12 minutes and collecting the hydrolyzed peptide. The initial rate of release was then calculated for different substrate concentrations (after 10 minutes) at fixed MMP concentrations. The maximum rate of reaction (V_{max}) and Michaelis constant (K_m) were deduced by fitting the Michaelis-Menten equation into the initial rate vs. substrate data shown in **Figure 6.9B**. The

turnover number k_{cat} was then calculated using **equation 6.5**. k_{cat}/K_m, a measure of catalytic efficiency, was highest for MMP-2, followed by MMP-9, MMP-13, MMP-8, and MMP-7.

Table 6.4 Molarity, optimum APMA concentration (for MMPs) and buffer conditions for all tested proteases.

Protease	Molarity (nM)	Optimum APMA concentration (nM MMP/mM APMA)	Buffer
MMP-2	138.89	4	50 mM TRIS-HCl, pH 7.5, 150 mM NaCl, 10 mM CaCl2, 0.05% Brij-35
MMP-7	357.14	10	
MMP-8	117.65	10	
MMP-9	547 (at 50 µg/mL)	2	
MMP-13	192.31	10	
MMP-14	322.58	2	
Trypsin	85840 (at 2 mg/mL)	N/A	200mM Tris/HCl, pH 7.5, 20 mM CaCl2
Cathepsin B	20000	N/A	100 mM Na/K phosphate, pH 6.0, 1.33 mM EDTA, 2 mM DTT
Legumain	13232	N/A	50 mM sodium acetate, 100 mM NaCl
Caspase-3	464.8	N/A	50 mM Hepes, pH 7.2, 50 mM NaCl, 0.1% Chaps, 10 mM EDTA, 5% Glycerol, 10 mM DTT
Caspase-6	554.7	N/A	
Caspase-8	541.4	N/A	

6.3.5 Peptide hydrolysis in 100% FBS and HT1080 culture media

Finally, the rate of peptide hydrolysis was tested in 100% FBS and complete culture media, and shown to be negligible (**Figure 6.10B**). This is an important result that indicates that the MMP-2 specific peptide on the surface of MSP-PEG-SPIONs is stable under physiological conditions.

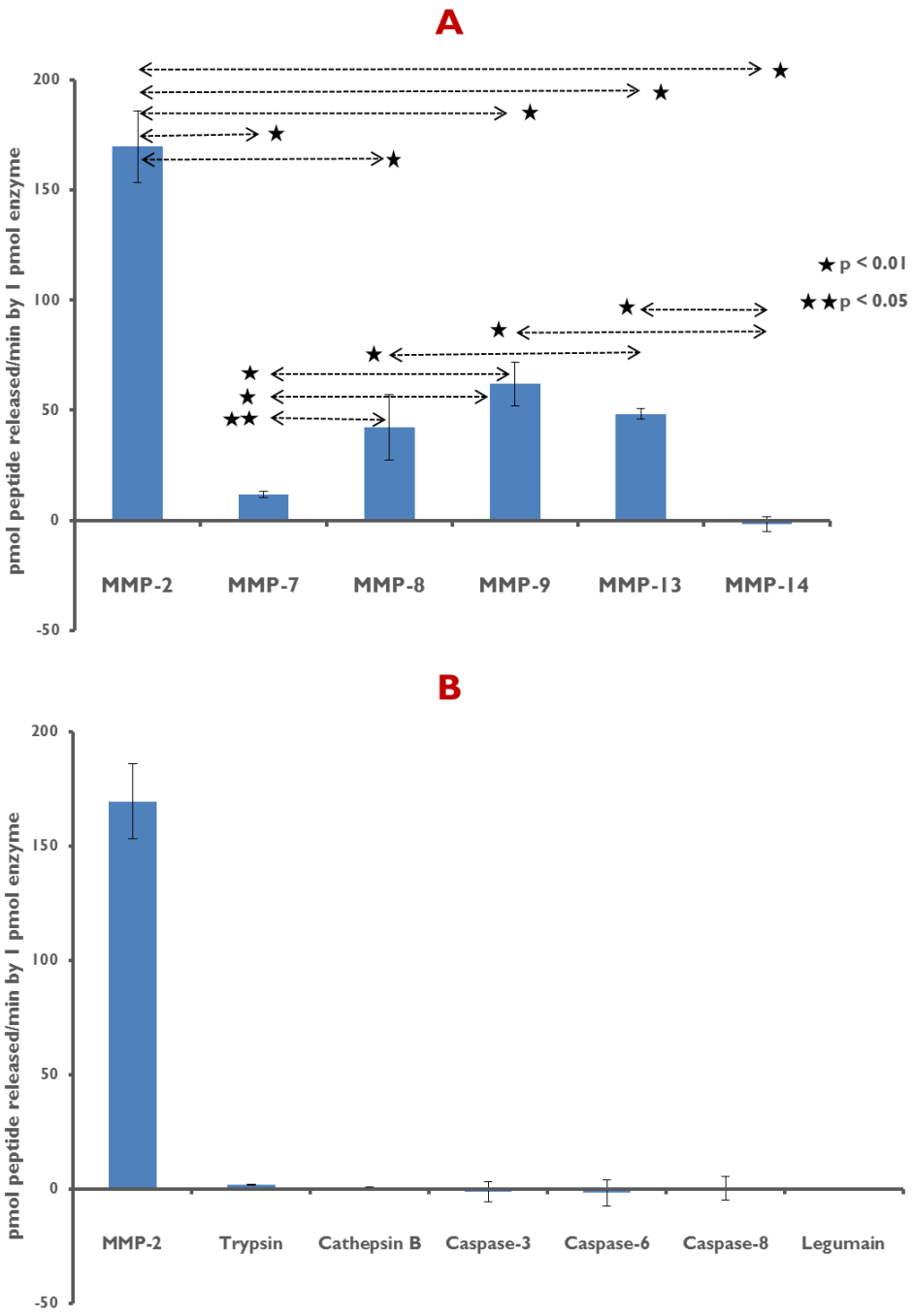

Figure 6.8 Protease activity on MSP-PEG-SPIONs. Showing initial rate (pmol peptide released/min by 1 pmol of protease) for **A.** All MMPs and **B.** MMP-2 vs non-MMPs.

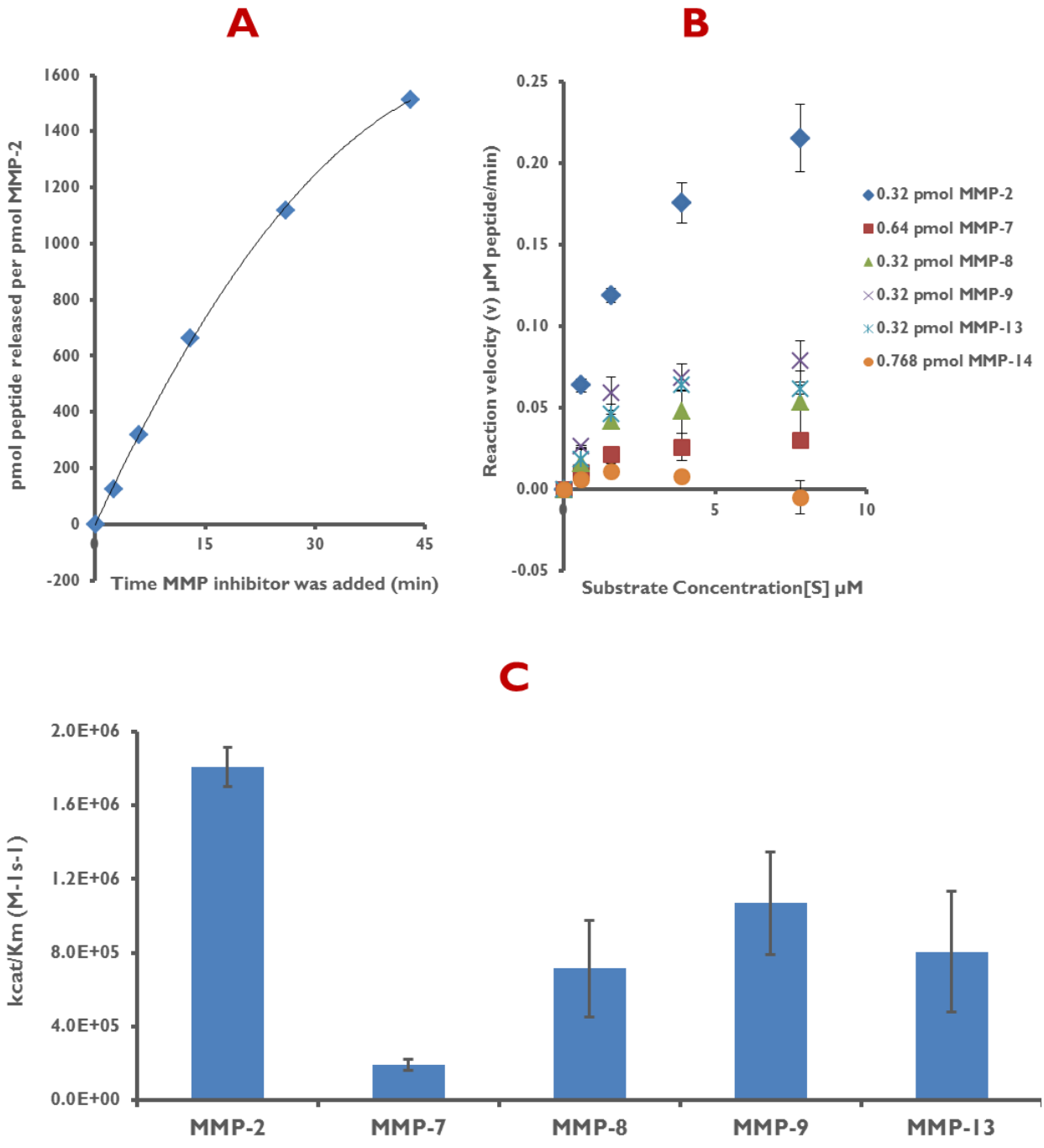

Figure 6.9 Michaelis Menten kinetics. **A.** Shows pmol peptide released per pmol MMP-2 at different time points. **B.** Initial reaction rate (velocity) at different substrate concentrations for all studies MMPs; **C.** k_{cat}/K_m for MMP-2, 7, 8, 9 and 13.

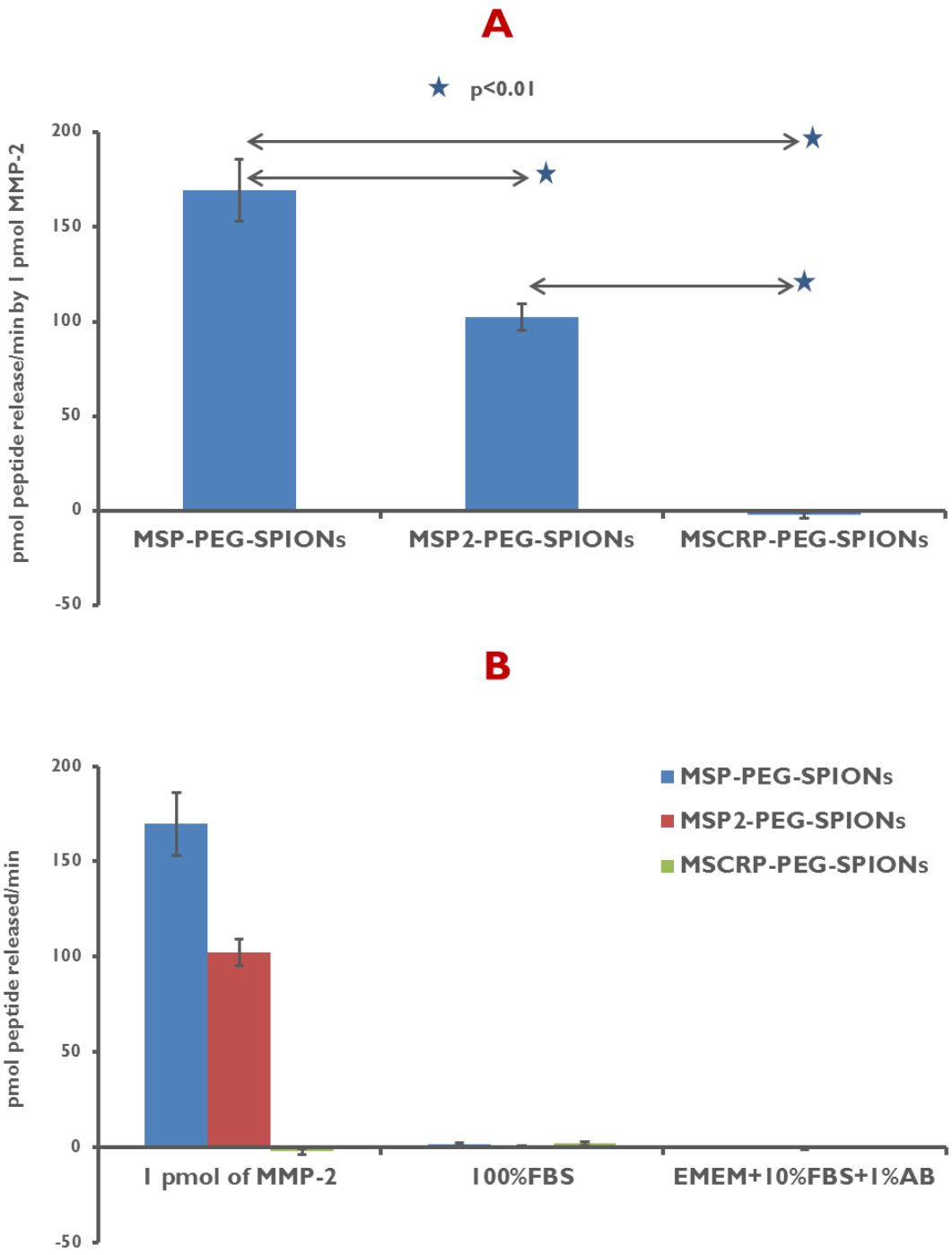

Figure 6.10 Pmol peptide hydrolyzed per minute for MSP-PEG-SPIONs (with MMP specific peptide #1), MSP2-PEG-SPIONs (with MMP specific peptide #2), and MSCRP-PEG-SPIONs (with MMP scrambled peptide to #1) **A.** with 1 pmol MMP-2, and **B.** in various conditions to assess stability in physiological mimicking conditions.

6.4 Conclusion

While several nanoprobes have been developed to quantify MMP activity, only a few have been tested against a wide variety of tumor-associated proteases. The tumor microenvironment consists of several types of proteases; therefore, it is important to create a probe that is specific towards a certain protease. MSP-PEG-SPIONs demonstrated significantly higher specificity towards MMP-2 versus all other MMPs. In addition, the probe showed negligible response towards trypsin, caspase 3, 6 and 8, cathepsin B and legumain. Finally, MSP-PEG-SPIONs demonstrated excellent stability in biological media.

Chapter 7 Development of tumor-targeting SPIONs

7.1 Introduction

So far, pharmacokinetically stable (chapter 3) and MMP-2 responsive (chapter 6) SPIONs were developed that can be tracked *in vivo* with high-resolution MSOT imaging (chapter 5). However, for the probe to be effective as a molecular imaging agent, it must selectively target the MMP-2 rich tumor microenvironment and accumulate in sufficient concentrations.

SPIONs can be engineered to preferentially target the tumor site via passive targeting, molecular targeting, and/or magnetic targeting. Due to abnormal angiogenesis associated with rapid growth, tumors contain a "leaky vasculature" with fenestrations and gaps in between endothelial cells that can be passively targeted with properly-sized SPIONs circulating in blood [53]. Moreover, due to poor lymphatic drainage, SPIONs are retained in the tumor interstitium for a longer period of time. Most clinically approved SPION-based T_2 contrast agents rely on passive targeting techniques for tumor imaging [165].

Alternatively, the vast surface area of SPIONs can be modified with targeting ligands (peptides, antibodies, aptamers, small molecules, lectins, etc.) that bind molecular signatures of cancer cells or endothelial cells of the tumor vasculature [53,187]. For example, the tumor-targeting peptide RGD binds preferentially to $\alpha_v\beta_3$ integrin, a cell adhesion receptor involved in tumor angiogenesis and overexpressed on the membrane of cancer and endothelial cells of malignant

tumors [188,189]. $\alpha_v\beta_3$ integrin-rich tumor cells have previously demonstrated significantly higher uptake of RGD-coated SPIONs compared to unconjugated SPIONs [190].

Last, the magnetic properties of SPIONs have been utilized in the magnetic targeting of SPIONs to the tumor region. Applying an external magnetic field over the tumor tissue creates an attractive force that guides nearby SPIONs in circulation to the tumor tissue. Sufficient magnetic force is necessary to overcome the drag force applied on SPIONs by blood flow [53].

While magnetic targeting is an attractive strategy, it goes beyond the scope of this dissertation. This chapter discusses the development of tumor targeting-SPIONs for molecular binding of several types of cancer cell lines *in vitro*.

7.2 Materials and methods

7.2.1 Materials

Amicon Ultra-4 centrifugal filter device (MWCO=50 kDa) was purchased from EMD Millipore. 5kDa Succinimidyl polyethylene glycol (5K mPEG-NHS) and 5kDa maleimide-PEG-NHS (5K MAL-PEG-NHS), were obtained from Nanocs. Pierce BCA protein assay kit, Sulfosuccinimidyl 4-(N-maleimidomethyl) cyclohexane-1-carboxylate (Sulfo SMCC) and Ellman's reagent were purchased from Thermo Scientific. Cyclo (-Arg-Gly-Asp-D-Phe-Cys) acetate salt (cRGDfC, molecular weight 578.65) was purchased from Bachem. Materials for the ferrozine assay were discussed in section 3.1.1. TrypLE Express was purchased from gibco by life technologies. Eagle's Minimum Essential Medium (EMEM) and HT-1080 fibrosarcoma human cells were purchased from the American Type Culture Collection (ATCC).

7.2.2 Gelatin Zymography to quantify MMP-2 secretion by HT-1080 cells

Gelatin zymography was used to detect pro and active levels of the gelatinase (MMP-2 and MMP-9) enzymes released by HT-1080 cells. The procedure is based on two protocols found in literature [191,192].

Zymographic gel preparation:

15 mL of an 8 % resolving gel solution were made by thoroughly mixing 4.89 mL DI water, 3.75 mL 1.5M Tris-Cl (pH 8.8), 0.3 mL 20% sodium dodecyl sulfate (SDS), 4.05 mL 30% acrylamide, and 2.25 mL 1% gelatin. 60 µL of 10% ammonium persulfate (APS) and 12 µL *N*, *N*, *N*′, *N*′-tetramethylethylenediamine (TEMED) were added after three minutes. The mixture was vortexed for a few seconds, then immediately poured into a gel casting chamber. Bubbles can

be removed by carefully overlaying the separating gel solution with 100% isopropyl alcohol, which was poured off after ~30 minutes (until the resolving gel polymerized).

8 mL of 5% stacking gel solution were prepared by mixing 5.4 mL DI water, 1.34 mL 30% acrylamide, 1 mL 1M TRIS (pH 6.8), 80 µL 10% SDS, 80 µL 10% APS, and 8 µL TEMED. The stacking gel solution was immediately pipetted over the polymerized resolving gel, and a 10-well comb was inserted into the liquid stacking gel while making sure no bubbles were trapped under the comb. The gel polymerized after 30 minutes and can be stored at 4 ◦C for a few days.

MMP preparation:

Various concentrations of pro and active MMP-2 and MMP-9 were prepared. Active MMPs were obtained by addition of 4-aminophenylmercuric acetate (APMA) to pro-MMPs.

Preparation of serum-free conditioned media:

Since serum contains gelatinases, it was important to prepare serum-free conditioned media for accurate analysis. HT-1080 cells incubated in 24 well plate at ~80% confluency were washed three times with EMEM (without FBS and antibiotics) and incubated with 60% of the usual volume (i.e. 600 µL) of serum-free media (99% EMEM, 1% antibiotics) for 16 hours. The serum-free media were collected and centrifuged to remove cells and debris. The protein content of the supernatant was measured using the protein BCA assay.

Preparation of cell lysates

HT1080 cells (~80% confluency) were washed twice with cold PBS. 250 µL of the cold lysis buffer were added to each well, and the lysate collected and incubated on ice for 15 minutes. The samples were then vortexed and centrifuged for 20 minutes at 4 ºC. The protein content of the supernatant was measured using the protein BCA assay.

Running and developing gel:

After pulling the comb from the stacking gel, the cassette was placed in the gel apparatus and the chambers filled with 1X running buffer (30.3 g Tris-base, 14.4 g glycine, 10 g SDS, 1 L DI water. The protein ladder was loaded first, followed by samples and standards, all in 1X sample buffer (20 µL per lane). The apparatus was operated at 60V for the first ~30 minutes (until the blue band reached the bottom of the stacking gel) and at 120V afterward, until the bromophenol blue tracking dye reached the bottom of the gel.

Gel activation:

The gel was carefully removed from the electrophoretic plates and placed in a plastic tray containing 100 mL renaturing buffer. The gel was incubated for 15 minutes at room temperature with gentle agitation, at which point the buffer was replaced with another 100-mL renaturing buffer and agitated for an extra 15 minutes. The renaturing buffer was decanted, and replaced with 100 mL 1X development buffer then incubated for 30 minutes with gentle agitation. The development buffer was replaced with 100 mL fresh development buffer discard, and the gel was incubated for 24 hours at 37 C.

Gel staining and destaining:

The developing buffer was decanted, and the gel stained with staining solution for 1 hour at room temperature with gentle agitation. Afterward, the gel was destained with a destaining solution and agitated until clear sharp bands appeared over the blue background.

7.2.3 Synthesizing RGD-PEG-SPIONs (method 1)

144.4 µL cRGDfC (at 2 mg/mL in water) were added to 100 µL 5 kDa MAL-PEG-NHS (at 10 mg/mL in pH 7.1 0.2M phosphate buffer), and the mixture incubated for 3 hours at 25 ºC. This corresponds to a 2.5:1 RGD to MAL-PEG-NHS ratio. This step relies on specific thiol group reaction with maleimide at near neutral pH. 100 µL aminated SPIONs (6.54 mg Fe/mL in 0.2M pH 8 0.2 M phosphate buffer) were then added to the RGD-PEG-NHS mixture, and incubated for 30 minutes at 25 ºC. Afterward, 2 mg 5K m-PEG-NHS, dissolved in 100 µL pH 8 0.2M pH 8 phosphate buffer and 100 µL DMS, were added to the mixture and incubated for 3 hours at 25 ºC. Excess unreacted components were separated from the final RGD-PEG-SPION mixture using Amicon Ultra-4 centrifugal filter device (MWCO of 50 kDa) and washed 7 times with DI water. A control was made and consisted of the same components but without RGD (labeled PEG-SPION).

7.2.4 Size stability of RGD-PEG-SPIONs in HT1080 cell culture medium

RGD-PEG-SPIONs were mixed with 1 mL complete HT-1080 cell culture media (EMEM + 10% FBS + 1% antibiotics) at a concentration of 0.055 mg Fe/mL in DLS cuvettes, then placed inside a cell culture incubator for 72 hours. At set time points, particle size was measured using DLS.

7.2.5 Protein BCA assay to quantify HT-1080 cell number

HT-1080 cells grown to 70% confluency in a 24 well plate was washed several times with 1X PBS. 200 µL of trypsin was added to detach cells from the surface of the well plate. Cells were counted using a hemocytometer, and 25 µL of different dilutions were added to a 96 well plate. 200 µL of BCA's working reagent was added to the mixture, incubated for 1 hour at 37 ◦C, cooled down to room temperature for 10 minutes, and its absorbance measured at 562 nm using a microplate reader.

7.2.6 Uptake of RGD-PEG-SPIONs (method 1) by HT-1080 fibrosarcoma cells

HT-1080 fibrosarcoma cells were cultured in 100 mm dishes containing EMEM supplemented with 10% FBS and 1% antibiotics in a cell incubator (37 ◦C, 5% CO_2). Cells were harvested with trypsin, counted with a hemocytometer under a microscope, and seeded at $4*10^4$ cells/well (1 mL total) in a 24-well plate. Cells were incubated for 48 hours until they reached ~70% confluency, then washed twice with 1X HBSS. 1 mL of RGD-PEG-SPIONs and PEG-SPIONs (0.055 mg Fe/mL in complete culture media) were added (n=3) to the cells and placed in a cell culture incubator for 4 hours. Blank media (without SPIONs) was used as a control. Following incubation, wells were washed 3 times with 1X PBS and detached with 260 µL trypsin. 200 µL were transferred to a 24 well plate, and the ferrozine assay was conducted similarly to what was described in **section 3.2.2**. In addition, a quantitative protein BCA assay (**section 7.2.5**) was run concurrently to quantify cell number in each well.

7.2.7 Synthesizing F3-PEG-SPIONs and RGD-PEG-SPIONs (method 2) with various SMCC to PEG ratios

A different method was used to attach the tumor-targeting peptide F3 (PKAARALPSQRSRPPEKAKKPPDKPAPEKKKC; MW~3536.18=g/mol) and RGD to aminated SPIONs. In this case, sulfo SMCC and 2K mPEG-NHS were added to aminated SPIONs (1624.75 mg Fe/mL in pH 7.4 phosphate buffer), along with DMSO at a 25% V/V ratio. Various NHS to amine ratios and SMCC to PEG ratios were used in synthesizing different samples (**Table 7.1**). All samples were incubated for 3.5 hours at room temperature and then centrifuged twice at 13,000 RPM to remove excess unreacted PEG and SMCC. RGD peptide (5 mg/mL in H_2O) was added to tubes R1-R4 at a 1:2.5 peptide to SMCC ratio in 0.1M phosphate buffer. F3 peptide (5 mg/mL in H_2O) was added to tubes F1-F3 at a 1:10 peptide to SMCC ratio and to tube F4 at a 1:2.5 peptide to SMCC ratio in 0.1M phosphate buffer. The functionality of the thiol group was confirmed with the Ellman's assay (**Section 6.2.2**). All samples were incubated overnight at room temperature. The excess unreacted peptide was removed with magnetic separation.

Table 7.1 All different formulations of RGD and F3-PEG-SPIONs (method 2).

	NHS:amine ratio	SMCC:PEG	Peptide:SMCC	Targeting peptide
R1	1 to 1	50:50	1:2.5	RGD
R2	1 to 2	50:50	1:2.5	RGD
R3	1 to 2	30:70	1:2.5	RGD
R4	1 to 2	10:90	1:2.5	RGD
F1	1 to 2	10:90	1:10	F3
F2	1 to 2	5:95	1:10	F3
F3	1 to 2	1:99	1:10	F3
F4	1 to 2	10:90	1:2.5	F3
Control	1 to 2	0:100	No peptide	None

7.2.8 Uptake of RGD-PEG-SPIONs (method 2) by MCF-7 and PC3 cells

PC3 cells and MCF-7 cells were seeded at 7*10^3 cells/well and at 2.7*10^4 cells/well, respectively, in a 24 well plate. Plates were incubated for 48 hours to allow cells to reach ~70-80% confluency and then washed twice with 1X HBSS. 500 µL of R1, R2, R3, R4 and control (0.08 and 0.04 mg Fe/mL) in complete culture medium (F12-K for PC3 and DMEM for MCF-7) were incubated with PC3 and MCF-7 cells for 4 hours and then washed with PBS. After the last wash, 100 µL of 1X PBS and 200 µL of 50 mM NaOH were added to the wells and incubated for 30 minutes at 37 ºC. Two 25 µL samples were transferred for quantitative protein analysis with the BCA assay, while the remaining 250 µL of cell lysate was kept in the original well for quantitative iron analysis with the ferrozine assay.

In the BCA assay, 200 µL of the BCA working reagent was added to the 25 µL cell lysate and incubated at 60 ºC for 30 minutes. Samples were cooled down for 5 minutes, and their absorbance measured at 562 nm. A standard curve was created by counting RAW 264.7 cells with a hemocytometer, and measuring the associated BCA signal of various dilutions.

In the ferrozine assay, 250 µL of equal volumes of 4.5% KMnO4 and 1.4M HCl were added to the 250 µL cell lysate, and the mixture incubated for 2 hours at 60 ºC. 62.5 µL of ferrozine solution (6.5mM ferrozine, 6.5mM Neocuproine, 2.5M ammonium acetate, and 1M ascorbic acid in H_2O) was added to the mixture and incubated for 30 minutes at room temperature. 250 µL were then transferred to a 96 well plate and absorbance was measured at 550 nm. Standard curves were created using known concentrations of SPIONs between 0 and 6.7 µg Fe/mL.

7.2.9 Uptake of F3-PEG-SPIONs (method 2) by MCF-7 and PC3 cells

PC3 cells and MCF-7 cells were seeded at 7*10^3 cells/well and at 2.7*10^4 cells/well, respectively, in a 24 well plate. Plates were incubated for 48 hours to allow cells to reach ~70-80% confluency and then washed twice with 1X HBSS. 500 μL of F1, F2, F3, F4 and control (0.15, 0.08 and 0.05 mg Fe/mL for PC3 and 0.08 mg Fe/mL for MCF-7) SPIONs in complete culture medium (F12-K for PC3 and DMEM for MCF-7) were incubated with the cells for 4 hours, and then washed with PBS. The BCA and ferrozine assays were conducted, as described in the previous section.

7.2.10 Statistical analysis

All measurements were run three times (unless otherwise stated). Data are presented as mean ± S.D.

7.3 Results and discussion

Selective accumulation of SPIONs at the tumor site can be accomplished using passive, molecular, and/or magnetic targeting. The size of SPIONs (~120 nm) already permits passive targeting into the tumor site via the enhanced permeability and retention effect. However, particles that rely solely on passive targeting can also accumulate in the inflamed region of non-cancerous tissues [193,194]. Moreover, the tumor vasculature is known to be heterogeneous, with variability in vessel gap size, which can result in a heterogeneous accumulation of SPIONs at the tumor site [53]. A complementary strategy is to actively target overexpressed tumor cell receptors through a tumor targeting ligand. The objective of this study was to investigate the effect of conjugating tumor targeting ligands on SPION uptake by several cancer cell lines.

7.3.1 Gelatin Zymography to quantify MMP-2 expression

The fast-growing and highly vascularized HT-1080 fibrosarcoma cells are the most commonly used cell line for studying MMP activity *in vitro* and *in vivo* [4,12,20,33,48,195–198]. In this experiment, gelatin zymography was used to confirm the secretion of MMP-2 and 9 in HT-1080 cell- conditioned media (**Figure 7.1**).

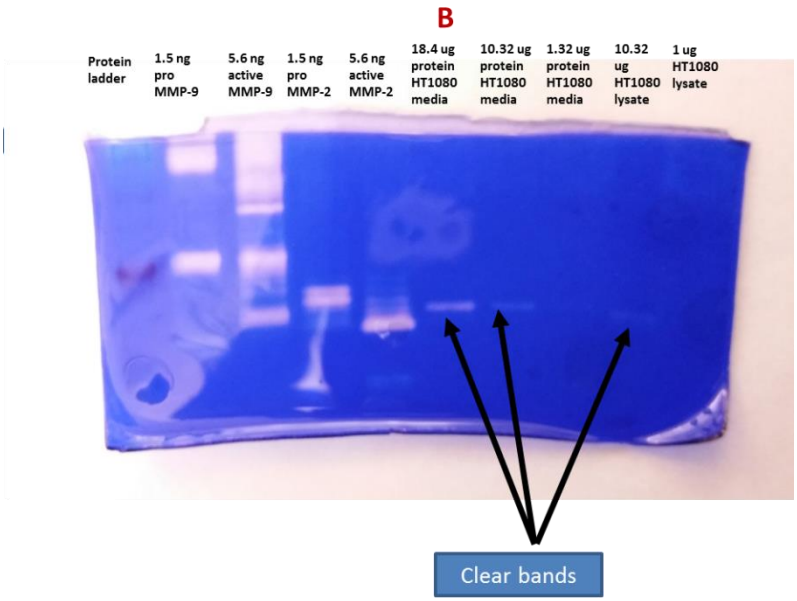

Figure 7.1 Gelatin zymography on serum-free conditioned media confirmed MMP-2 and MMP-9 secretion by HT-1080 cells.

7.3.2 Synthesizing RGD-PEG-SPIONs

Several articles reported the overexpression of $\alpha_v\beta_3$ integrin receptor on the surface of HT-1080 cells [199–201]. The RGD peptide is a potent antagonist of $\alpha_v\beta_3$ integrin and was thus chosen as the tumor targeting ligand for molecular targeting of HT-1080 cells [189,201]. The cyclic form of the RGD (cRGD) peptide was chosen due to its higher stability and higher affinity towards $\alpha_v\beta_3$ integrin over its linear counterpart (**Figure 7.2**) [202–204].

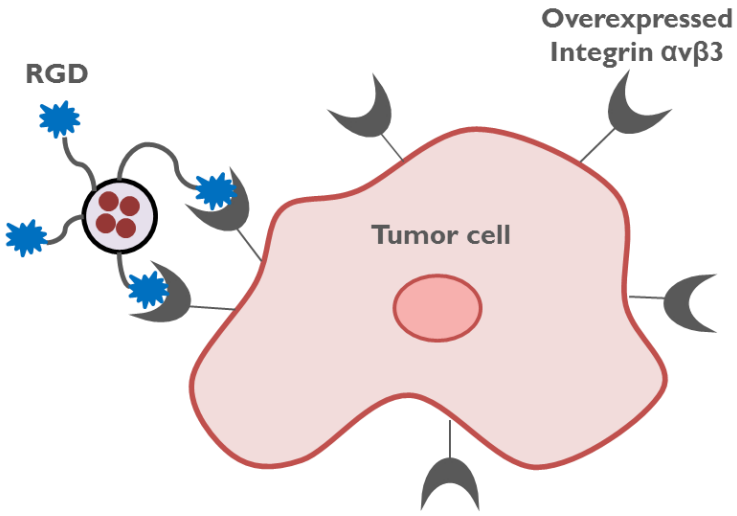

Figure 7.2 Conceptual schematic of the interaction between RGD-SPIONs and integrin $\alpha_v\beta_3$ on the surface of HT1080 fibrosarcoma cells.

The reaction scheme for attaching the cRGDfC peptide to aminated SPIONs is shown in **Figure 7.3** (method 1). Thiol-containing cRGDfC were first conjugated to the maleimide end of the heterobifunctional MAL-PEG-NHS (MAL-PEG-NHS) through a thiol-maleimide reaction. The $_D$-amino acid residue (f) forces the peptide into a conformation that favors binding to $\alpha_v\beta_3$ integrin over other members of the integrin family [204]. The particles were labeled RGD-PEG-SPIONs.

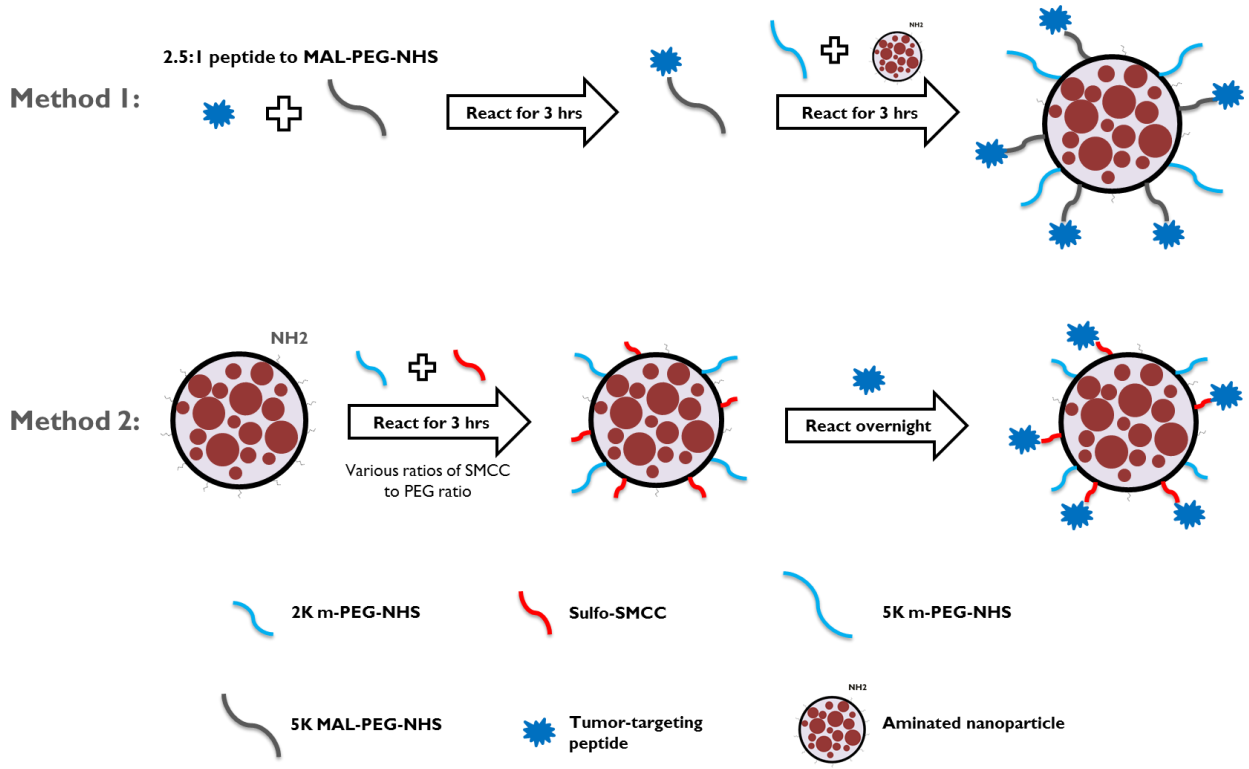

Figure 7.3 Reaction scheme for conjugating cRGDfC targeting ligand to aminated SPIONs.

7.3.3 RGD-PEG-SPION size stability and uptake by HT1080 fibrosarcoma cells

The size stability of RGD-PEG-SPIONs was tested in HT-1080 complete cell culture medium (**Figure 7.4A**). The tumor-targeting SPIONs demonstrated excellent size stability, with the hydrodynamic diameter increasing by only a few nanometers over the first 24 hours, and by less than 20 nm after 72 hours. A cell uptake study was then conducted to assess the impact of RGD on molecular targeting of HT-1080 cells. The ferrozine and BCA assays were used to quantify iron uptake and number of cells per well, respectively. **Figure 7.4C** indicates that the uptake of RGD-PEG-SPIONs by HT-1080 cells was significantly (35.3 times) higher than uptake of PEG-SPIONs without the RGD ligand.

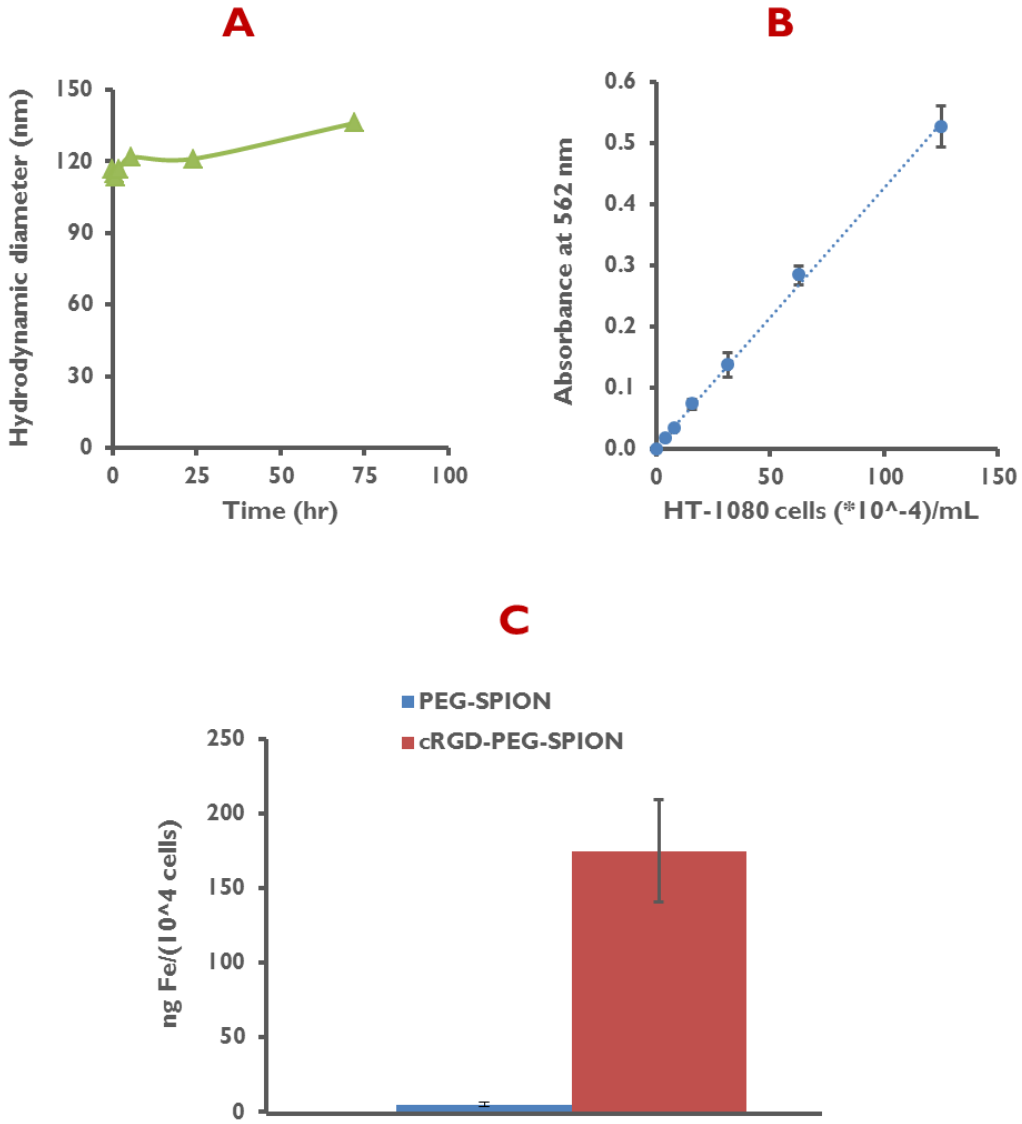

Figure 7.4 RGD studies **A.** 72 hour-size stability study of RGD-PEG-SPION (method 1) in HT-1080 complete culture medium. **B.** A standard curve for BCA protein quantification at different HT-1080 cell number. **C.** Uptake of RGD-PEG-SPIONs and the control (PEG-SPIONs) by HT1080 cells.

7.3.4 RGD-PEG-SPION uptake by PC3 and MCF-7 cells

The uptake of RGD-PEG-SPIONs by PC3 prostate cancer and MCF-7 breast cancer cells was tested. For this experiment, a new strategy was used to conjugate RGD peptide to the surface of SPIONs (**Figure 7.3**, method 2). SMCC, which has both a maleimide and NHS groups, was used as the crosslinker, while 2 kDa mPEG-NHS was used to add steric stabilization to SPIONs. The ratio of SMCC to PEG moieties, which affects both the concentration of RGD on SPIONs as well as its colloidal stability, was varied among different structures. Increasing the amount of SMCC also increases the amount of RGD attached to the surface of SPIONs. However, preliminary experiments have indicated that addition of more than 50% SMCC causes rapid particle aggregation.

Two different concentrations of the different RGD-PEG-SPION structures were incubated with both PC3 and MCF-7 cells. Results are shown in **Figure 7.5**. R1 SPIONs (1:1 NHS to amine and 50:50 SMCC to PEG) at 0.04 mg Fe/well had the highest uptake by PC3 cells among all tested SPIONs, and its uptake is significantly higher than PEG-SPIONs (control). Surprisingly, there was no significant difference in the uptake of any of the RGD-PEG-SPIONs by MCF-7 cells compared to PEG-SPIONs. MCF-7 is known to be $\alpha_v\beta_3$ integrin-rich and is commonly used in literature for RGD-uptake studies [205].

7.3.5 F3-PEG-SPION uptake by PC3 and MCF-7 cells

F3 peptide targets overexpressed nucleolin on the surface of cancer cells. The uptake of F3-PEG-SPIONs by PC3 prostate cancer and MCF-7 breast cancer cells was studied *in vitro*. Results are shown in **Figure 7.6**. F1 SPIONs (1:2 NHS to amine, 50:50 SMCC to PEG and 1:10 peptide to SMCC) at 0.075 mg Fe/well had the highest uptake by PC3 cells among all tested

structures, and its uptake was significantly (2.45 times) higher than PEG-SPIONs. None of the F3-PEG-SPIONs were taken up significantly more by MCF-7 cells compared to PEG-SPIONs.

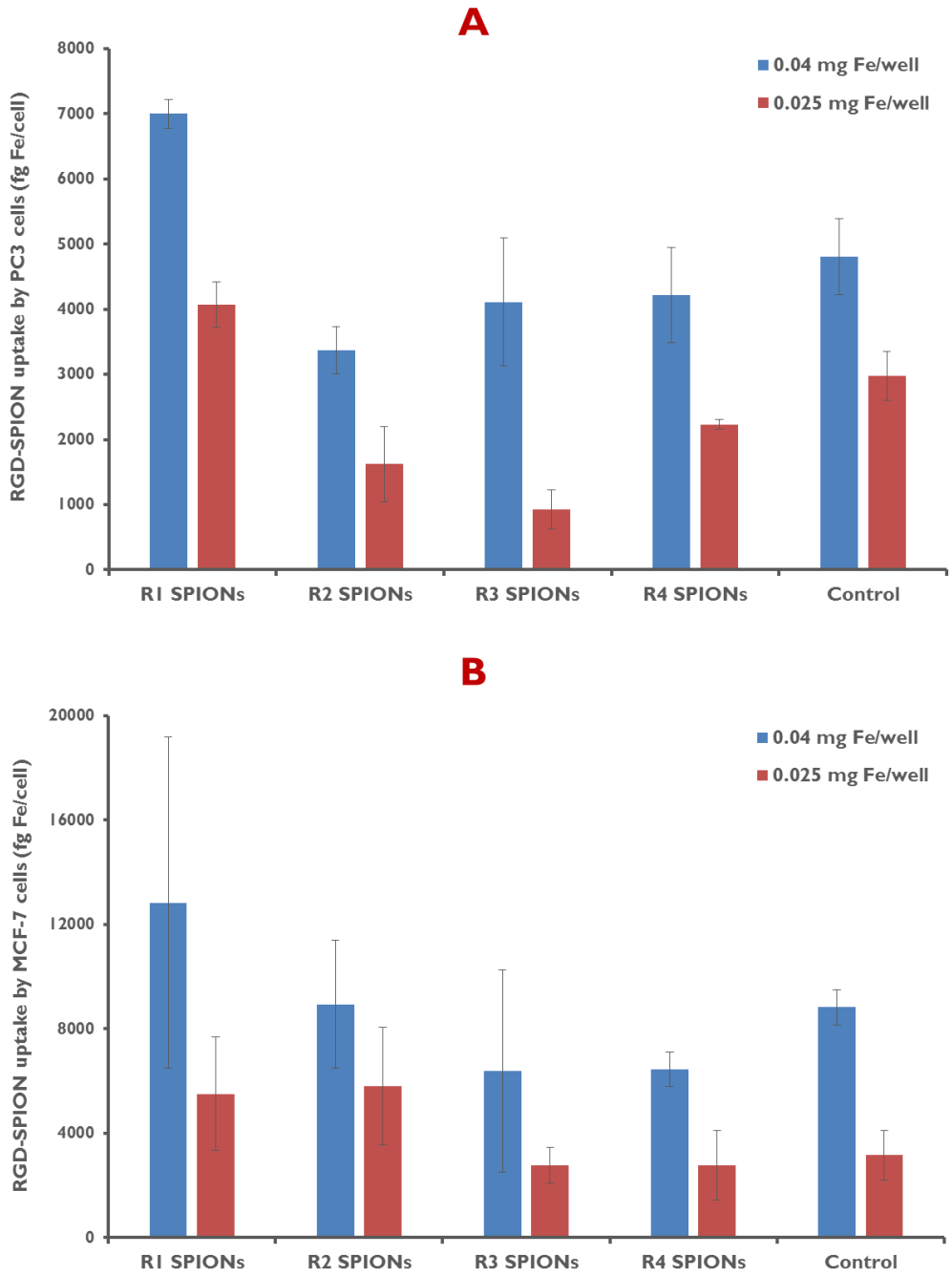

Figure 7.5 Uptake of RGD-PEG-SPIONs by **A.** PC3 cells, and **B.** MCF-7 cells.

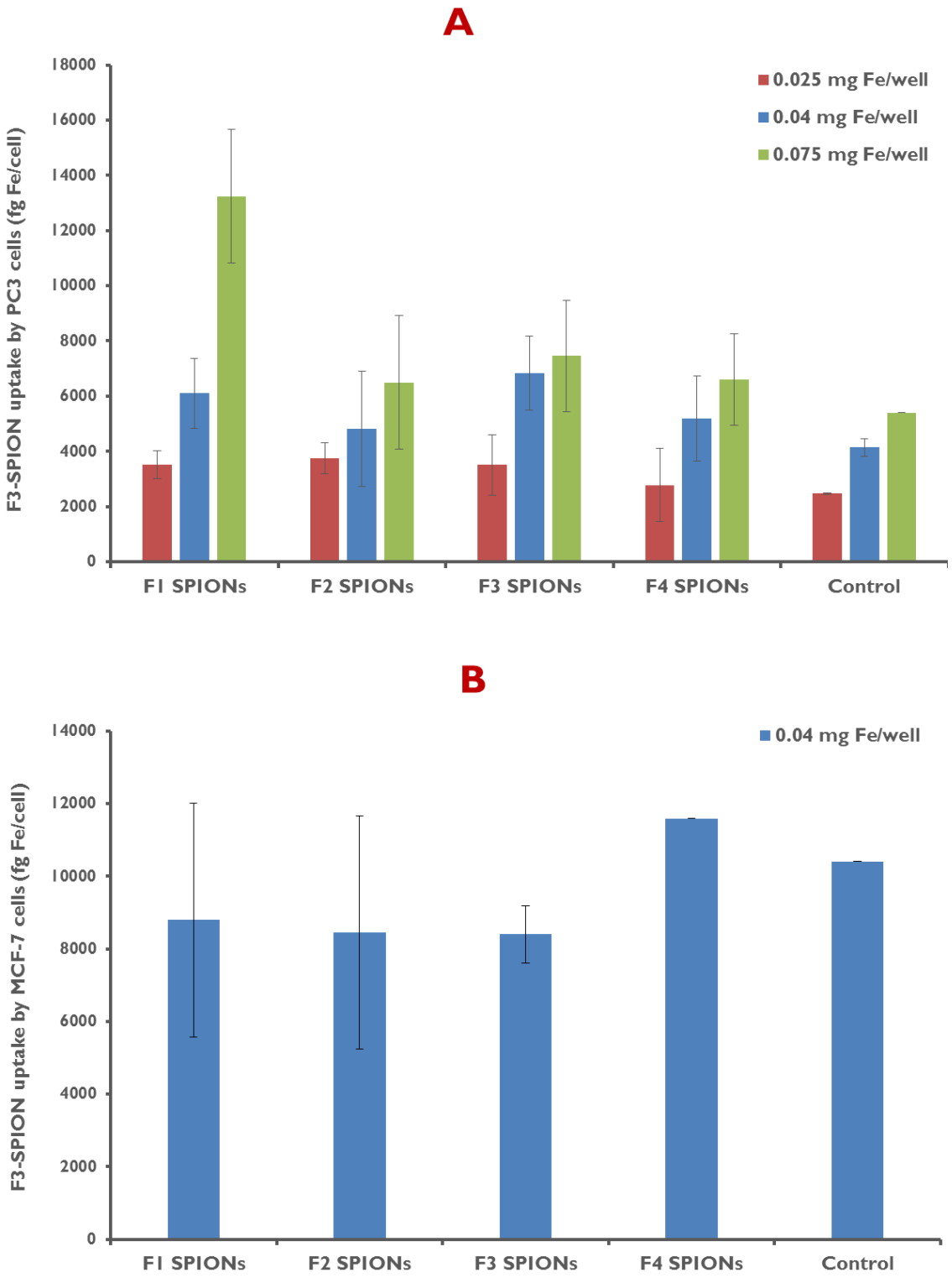

Figure 7.6 Uptake of F3-PEG-SPIONs by **A.** PC3 cells, and **B.** MCF-7 cells.

7.4 Conclusion

For the imaging probe to be effective, it must be colloidally stable in physiological conditions; target a specific protease, have strong optoacoustic properties, and accumulate selectively in the tumor microenvironment. The first three objectives were fulfilled in the previous chapters. In this chapter, two tumor targeting ligands (RGD and F3) were conjugated to the surface of aminated SPIONs, and their uptake by HT-1080, PC3 and MCF-7 cells studied. It appears that the best combination involves RGD-PEG-SPIONs targeting HT-1080 cells, which resulted in a 35-fold increase in uptake over PEG-SPIONs.

Chapter 8 Summary

The goal of this research project was to develop SPIONs with high colloidal stability (chapter 3), strong optoacoustic properties (chapters 4&5), and tumor targeting ability (chapter 7) for quantifying MMP-2 activity with high specificity and sensitivity (chapter 6).

In chapter 3, 5 kDa polyethylene glycol (PEG) moieties were conjugated to the surface of aminated SPIONs for added sterical stabilization. PEG-SPIONs demonstrated significantly higher colloidal stability, reduced plasma protein adsorption and significantly lower uptake by macrophage cells *in vitro* compared to unmodified SPIONs.

The effect of varying the molecular weight of PEG (2K, 5K, and 20K) on colloidal stability was investigated both *in vitro* and *in vivo* in chapter 5. 2K and 5K-Cy7-SPIONs demonstrated significantly higher colloidal stability and reduced uptake by macrophage cells compared to 20K-Cy7-SPIONs and were thus carried forward for further *in vivo* testing. Molecular imaging of SPION pharmacokinetics (pK) and biodistribution was conducted using multispectral optoacoustic tomography (MSOT) and included longitudinal tomographic scanning of the jugular vein, liver, kidneys, and spleen. MSOT is a novel imaging modality that provides high resolution and improved penetration depths compared to near-infrared fluorescence imaging. As expected, the majority of SPIONs were cleared by the liver and spleen. 2K-Cy7- SPIONs had significantly longer circulation half-life compared to 5K-Cy7-SPIONs, making it the preferred imaging agent moving forward. To validate the quantitative findings of MSOT, *ex vivo* tissues were collected, and SPION concentrations quantified with electron paramagnetic resonance (EPR). The signal was

maximum in the liver then spleen, and negligible in the kidneys, brain, and heart. In addition, EPR and MSOT showed remarkable agreement.

Next, an MMP-2 sensitive peptide was conjugated to the surface of 2K PEG-SPIONs, and its specificity towards MMP-2 was thoroughly investigated (chapter 6). The resulting probe demonstrated significantly higher specificity towards MMP-2 compared to all the other tumor-associated proteases. Active tumor targeting was also achieved by conjugating the tumor targeting ligands RGD and F3 to the surface of SPIONs (chapter 7). RGD-SPIONs and F3-SPIONs demonstrated a high affinity to HT-1080 fibrosarcoma and PC3 prostate cancer cell lines, respectively.

The developed probe can be used in several future biomedical applications. First, it can be used to quantify MMP-2 activity in MMP-2 overexpressing HT-1080 tumors *in vivo*. In that case, the dual fluorochrome probe Cy5-Cy7-SPIONs developed in chapter 4 will be modified by linking the Cy7 fluorophore to SPIONs through an MMP-2 cleavable peptide (GPLGVRGC) used in chapter 6. In addition, the tumor targeting capability of RGD-conjugated SPIONs (chapter 7) can be utilized for drug delivery applications.

References

1. Siegel, R. L., Miller, K. D. & Jemal, A. Cancer statistics, 2017. *CA. Cancer J. Clin.* **67,** 7–30 (2017).

2. Massoud, T. F. & Gambhir, S. S. Molecular imaging in living subjects: seeing fundamental biological processes in a new light. *Genes Dev.* **17,** 545–580 (2003).

3. Mankoff, D. a. A definition of molecular imaging. *J. Nucl. Med.* **48,** 18N, 21N (2007).

4. Harris, T. J. *et al.* Protease-triggered unveiling of bioactive nanoparticles. *Small* **4,** 1307–1312 (2008).

5. Ross, J. S. *et al.* Prognostic significance of matrix metalloproteinase 2 and tissue inhibitor of metalloproteinase 2 expression in prostate cancer. *Mod. Pathol.* **16,** 198–205 (2003).

6. Kuniyasu, H. *et al.* Relative Expression of Type IV Collagenase , E-cadherin , and Vascular Endothelial Growth Factor / Vascular Permeability Factor in Prostatectomy Specimens Distinguishes Organ-confined from Pathologically Advanced Prostate Cancers Relative Expression of Ty. *Clin. Cancer Res.* **6,** 2295–2308 (2000).

7. Yong, V. W., Power, C., Forsyth, P. & Edwards, D. R. Metalloproteinases in biology and pathology of the nervous system. *Nat. Rev. Neurosci.* **2,** 502–511 (2001).

8. Verma, S. Matrix metalloproteinases and gastrointestinal cancers: Impacts of dietary antioxidants. *World J. Biol. Chem.* **5,** 355 (2014).

9. Hadler-Olsen, E., Winberg, J. O. & Uhlin-Hansen, L. Matrix metalloproteinases in cancer: Their value as diagnostic and prognostic markers and therapeutic targets. *Tumor Biol.* **34,** 2041–2051 (2013).

10. Gujrati, V., Mishra, A. & Ntziachristos, V. Molecular imaging probes for multi-spectral optoacoustic tomography. *Chem. Commun. (Camb).* **53,** 4653–4672 (2017).

11. Cha, E.-J. *et al.* Development of MRI/NIRF 'activatable' multimodal imaging probe based on iron oxide nanoparticles. *J. Control. release* **155,** 152–8 (2011).

12. Olson, E. S. *et al.* Activatable cell penetrating peptides linked to nanoparticles as dual

probes for in vivo fluorescence and MR imaging of proteases. *Proc. Natl. Acad. Sci. U. S. A.* **107,** 4311–6 (2010).

13. Haris, M. *et al.* In vivo magnetic resonance imaging of tumor protease activity. *Sci. Rep.* **4,** 6081 (2014).

14. Kimbrough, C. W., Hudson, S., Khanal, A., Egger, M. E. & McNally, L. R. Orthotopic pancreatic tumors detected by optoacoustic tomography using Syndecan-1. *J. Surg. Res.* **193,** 246–254 (2015).

15. Lee, S., Ryu, J., Park, K., Lee, A. & Lee, S. Polymeric nanoparticle-based activatable near-infrared nanosensor for protease determination in vivo. *Nano Lett.* **9,** 4412–4416 (2009).

16. Lee, S. *et al.* Tumor-homing glycol chitosan-based optical/PET dual imaging nanoprobe for cancer diagnosis. *Bioconjug. Chem.* **25,** 601–10 (2014).

17. Lee, S. *et al.* A near-infrared-fluorescence-quenched gold-nanoparticle imaging probe for in vivo drug screening and protease activity determination. *Angew. Chem. Int. Ed. Engl.* **47,** 2804–7 (2008).

18. Pysz, M. A., Gambhir, S. S. & Willmann, J. K. Molecular Imaging: Current Status and Emerging Strategies. *Clin. Radiol.* **65,** 500–516 (2010).

19. Albanese, A., Tang, P. S. & Chan, W. C. W. The effect of nanoparticle size, shape, and surface chemistry on biological systems. *Annu. Rev. Biomed. Eng.* **14,** 1–16 (2012).

20. Wong, C. *et al.* Multistage nanoparticle delivery system for deep penetration into tumor tissue. *Proc. Natl. Acad. Sci. U. S. A.* **108,** 2426–2431 (2011).

21. Cardone, R. a, Casavola, V. & Reshkin, S. J. The role of disturbed pH dynamics and the Na+/H+ exchanger in metastasis. *Nat. Rev. Cancer* **5,** 786–795 (2005).

22. Rofstad, E. K., Mathiesen, B., Kindem, K. & Galappathi, K. Acidic extracellular pH promotes experimental metastasis of human melanoma cells in athymic nude mice. *Cancer Res.* **66,** 6699–6707 (2006).

23. Crayton, S. H. & Tsourkas, A. pH titratable superparamagnetic iron oxide for improved nanoparticle accumulation in acidic tumor microenvironments. *ACS Nano* **5,** 9592–9601 (2011).

24. Krohn, K. A., Link, J. M. & Mason, R. P. Molecular Imaging of Hypoxia. *J. Nucl. Med.* **49,** 129S–148S (2008).

25. Napp, J. *et al.* Targeted luminescent near-infrared polymer-nanoprobes for in vivo imaging of tumor hypoxia. *Anal. Chem.* **83,** 9039–9046 (2011).

26. Anani, T., Panizzi, P. & David, A. E. Nanoparticle-based probes to enable noninvasive imaging of proteolytic activity for cancer diagnosis. *Nanomedicine* **11,** 2007–2022 (2016).

27. Bray, F., Jemal, A., Grey, N., Ferlay, J. & Forman, D. Global cancer transitions according to the Human Development Index (2008-2030): a population-based study. *Lancet. Oncol.* **13,** 790–801 (2012).

28. Yang, Y., Hong, H., Zhang, Y. & Cai, W. Molecular imaging of proteases in cancer. *Cancer growth metastasis* **2,** 13–27 (2009).

29. Luo, S., Zhang, E., Su, Y., Cheng, T. & Shi, C. A review of NIR dyes in cancer targeting and imaging. *Biomaterials* **32,** 7127–38 (2011).

30. Seaman, M. & Contino, G. Molecular imaging agents: impact on diagnosis and therapeutics in oncology. *Expert Rev. Mol. Med.* **12,** e20 (2010).

31. Sivasubramanian, M., Hsia, Y. & Lo, L.-W. Nanoparticle-facilitated functional and molecular imaging for the early detection of cancer. *Front. Mol. Biosci.* **1,** 1–16 (2014).

32. Yoon, S. M. *et al.* Application of Near-Infrared Fluorescence Imaging Using a Polymeric Nanoparticle-Based Probe for the Diagnosis and Therapeutic Monitoring of Colon Cancer. *Dig. Dis. Sci.* **56,** 3005–3013 (2011).

33. Chien, M.-P. *et al.* Enzyme-Directed Assembly of a Nanoparticle Probe in Tumor Tissue. *Adv Mater.* **25,** 3599–3604 (2013).

34. Steeg, P. S. Tumor metastasis: mechanistic insights and clinical challenges. *Nat. Med.* **12,** 895–904 (2006).

35. Lin, X. *et al.* Hybrid ferritin nanoparticles as activatable probes for tumor imaging. *Angew. Chemie - Int. Ed.* **50,** 1569–1572 (2011).

36. Lee, C.-M. *et al.* Optical imaging of MMP expression and cancer progression in an inflammation-induced colon cancer model. *Int. J. Cancer* **131,** 1846–53 (2012).

37. Yhee, J. Y. *et al.* Optical imaging of cancer-related proteases using near-infrared fluorescence matrix metalloproteinase-sensitive and cathepsin B-sensitive probes. *Theranostics* **2,** 179–89 (2012).

38. Lee, S. *et al.* Dark Quenched Matrix Metalloproteinase Fluorogenic Probe for Imaging Osteoarthritis Development in Vivo. *Bioconjug. Chem.* **19,** 1743–1747 (2008).

39. Jiang, T. *et al.* Tumor imaging by means of proteolytic activation of cell-penetrating peptides. *Proc. Natl. Acad. Sci. U. S. A.* **101,** 17867–72 (2004).

40. Bremer, C., Tung, C. H. & Weissleder, R. In vivo molecular target assessment of matrix metalloproteinase inhibition. *Nat. Med.* **7,** 743–748 (2001).

41. McIntyre, J., Fingleton, B., Wells, K. & Piston, D. Development of a novel fluorogenic proteolytic beacon for in vivo detection and imaging of tumour-associated matrix metalloproteinase-7 activity. *Biochem. J* **377,** 617–628 (2004).

42. Scherer, R., VanSaun, M., McIntyre, O. & Matrisian, L. Optical imaging of matrix metalloproteinase-7 activity in vivo using a proteolytic nanobeacon. *Mol. Imaging* **7,** 118–131 (2008).

43. Kim, K. *et al.* Cell-permeable and biocompatible polymeric nanoparticles for apoptosis imaging. *J. Am. Chem. Soc.* **128,** 3490–3491 (2006).

44. Ryu, J. H. *et al.* Early diagnosis of arthritis in mice with collagen-induced arthritis, using a fluorogenic matrix metalloproteinase 3-specific polymeric probe. *Arthritis Rheum.* **63,** 3824–32 (2011).

45. Thorek, D., Ogirala, A., Beattie, B. & Grimm, J. Quantitative imaging of disease signatures through radioactive decay signal conversion. *Nat. Med.* **19,** 1345–1350 (2013).

46. Sun, I. C. *et al.* Tumor-targeting gold particles for dual computed tomography/optical cancer imaging. *Angew. Chemie - Int. Ed.* **50,** 9348–9351 (2011).

47. Gallo, J. *et al.* CXCR4-targeted and MMP-responsive iron oxide nanoparticles for enhanced magnetic resonance imaging. *Angew. Chem. Int. Ed. Engl.* **53,** 9550–4 (2014).

48. Harris, T. J., Von Maltzahn, G., Derfus, A. M., Ruoslahti, E. & Bhatia, S. N. Proteolytic actuation of nanoparticle self-assembly. *Angew. Chemie - Int. Ed.* **45,** 3161–3165 (2006).

49. Yao, H., Zhang, Y., Xiao, F., Xia, Z. & Rao, J. Quantum dot/bioluminescence resonance energy transfer based highly sensitive detection of proteases. *Angew. Chemie - Int. Ed.* **46,** 4346–4349 (2007).

50. Egusquiaguirre, S. P. *et al.* Optoacoustic imaging enabled biodistribution study of cationic polymeric biodegradable nanoparticles. *Contrast Media Mol. Imaging* 1644 (2015). doi:10.1002/cmmi.1644

51. Mccarthy, J. R. & Weissleder, R. Multifunctional magnetic nanoparticles for targeted imaging and therapy. *Adv. Drug Deliv. Rev.* **60,** 1241–1251 (2008).

52. Welch, M. J., Hawker, C. J. & Wooley, K. L. The advantages of nanoparticles for PET. *J. Nucl. Med.* **50,** 1743–1746 (2009).

53. Cole, A. J., Yang, V. C. & David, A. E. Cancer theranostics: The rise of targeted magnetic nanoparticles. *Trends Biotechnol.* **29,** 323–332 (2011).

54. Shin, S. J., Beech, J. R. & Kelly, K. a. Targeted nanoparticles in imaging: paving the way for personalized medicine in the battle against cancer. *Integr. Biol.* **5,** 29–42 (2013).

55. von Maltzahn, G. *et al.* Nanoparticle self-assembly gated by logical proteolytic triggers. *J. Am. Chem. Soc.* **129,** 6064–5 (2007).

56. Schellenberger, E. *et al.* Protease-Specific Nanosensors for Magnetic Resonance Imaging. *Bioconjug. Chem.* **19,** 2440–2445 (2008).

57. Yan, L., Gao, Y., Pierce, R. & Dai, L. Development of Y-shaped peptide for constructing nanoparticle systems targeting tumor-associated macrophages in vitro and in vivo. *Mater. Res. Express* **1,** (2014).

58. Ansari, C. *et al.* Development of novel tumor-targeted theranostic nanoparticles activated by membrane-type matrix metalloproteinases for combined cancer magnetic resonance imaging and therapy. *Small* **10,** 566–575 (2014).

59. O, C. R. *et al.* Intracellular Self-Assembly and Disassembly of 19 F Nanoparticles Confer Respective 'Off' and 'On' 19 F NMR/MRI Signals for Legumain Activity Detection in Zebra fish. *ACS Nano* **9,** 5117–5124 (2015).

60. Ryu, J. H. *et al.* Non-invasive optical imaging of cathepsin B with activatable fluorogenic nanoprobes in various metastatic models. *Biomaterials* **35,** 2302–11 (2014).

61. Park, K., Jeong, J. & Chung, B. H. Cascade imaging of proteolytic pathways in cancer cells using fluorescent protein-conjugated gold nanoquenchers. *Chem. Commun. (Camb).* **48,** 10547–9 (2012).

62. Deng, D., Zhang, D., Li, Y., Achilefu, S. & Gu, Y. Gold nanoparticles based molecular beacons for in vitro and in vivo detection of the matriptase expression on tumor. *Biosens. Bioelectron.* **49,** 216–221 (2013).

63. Xie, J. *et al.* Manipulating the Power of an Additional Phase: A Flower-like Au−Fe3O4 Optical Nanosensor for Imaging Protease Expressions In vivo. *ACS Nano* **5,** 3043–3051 (2011).

64. Mu, C., LaVan, D., Langer, R. & Zetter, B. Self-assembled gold nanoparticle molecular probes for detecting proteolytic activity in vivo. *ACS Nano* **4,** 1511–1520 (2010).

65. Cordovilla, C. & Swager, T. M. Strain release in organic photonic nanoparticles for protease sensing. *J. Am. Chem. Soc.* **134,** 6932–5 (2012).

66. Kim, Y., Daniel, W. L., Xia, Z., Xie, H. & Mirkin, A. Bioluminescent nanosensors for protease detection based upon gold nanoparticle – luciferase conjugates w. *Chem. Commun.* **46,** 76–78 (2010).

67. Zeng, T. *et al.* Compact, Programmable, and Stable Biofunctionalized Upconversion Nanoparticles Prepared through Peptide-Mediated Phase Transfer for High-Sensitive Protease Sensing and in Vivo Apoptosis Imaging. *Appl. Mater. Interfaces* **7,** 11849–11856 (2015).

68. Chen, W.-H. *et al.* Therapeutic nanomedicine based on dual-intelligent functionalized gold nanoparticles for cancer imaging and therapy in vivo. *Biomaterials* **34,** 8798–807 (2013).

69. Yi, D. K. *et al.* Matrix metalloproteinase sensitive gold nanorod for simultaneous bioimaging and photothermal therapy of cancer. *Bioconjug. Chem.* **21,** 2173–7 (2010).

70. Yang, K. *et al.* Visualization of protease activity in vivo using an activatable photo-acoustic imaging probe based on CuS nanoparticles. *Theranostics* **4,** 134–41 (2014).

71. Veiseh, O., Gunn, J. W. & Zhang, M. Design and fabrication of magnetic nanoparticles for targeted drug delivery and imaging. *Adv. Drug Deliv. Rev.* **62,** 284–304 (2010).

72. Felton, C. *et al.* Magnetic nanoparticles as contrast agents in biomedical imaging: recent advances in iron- and manganese-based magnetic nanoparticles. *Drug Metab. Rev.* **46,** 142–

154 (2014).

73. Chertok, B. *et al.* Iron Oxide Nanoparticles as a Drug Delivery Vehicle for MRI Monitored Magnetic Targeting of Brain Tumors. *Biomaterials* **29,** 487–496 (2008).

74. Liu, C., Sun, C., Huang, H., Janda, K. & Edgington, T. Overexpression of legumain in tumors is significant for invasion/metastasis and a candidate enzymatic target for prodrug therapy. *Cancer Res.* **63,** 2957–2964 (2003).

75. Lin, S. *et al.* A novel legumain protease-activated micelle cargo enhances anticancer activity and cellular internalization of doxorubicin. *J. Mater. Chem. B* **3,** 6001–6012 (2015).

76. Siveen, K. S. & Kuttan, G. Role of macrophages in tumour progression. *Immunol. Lett.* **123,** 97–102 (2009).

77. Luo, Y. *et al.* Targeting tumor-associated macrophages as a novel strategy against breast cancer. *J. Clin. Invest.* **116,** 2132–2141 (2006).

78. Ansari, C. *et al.* Development of novel tumor-targeted theranostic nanoparticles activated by membrane-type matrix metalloproteinases for combined cancer magnetic resonance imaging and therapy. *Small* **10,** 566–417 (2014).

79. Hilderbrand, S. a. & Weissleder, R. Near-infrared fluorescence: application to in vivo molecular imaging. *Curr. Opin. Chem. Biol.* **14,** 71–79 (2010).

80. Kim, J., Piao, Y. & Hyeon, T. Multifunctional nanostructured materials for multimodal imaging, and simultaneous imaging and therapy. *Chem. Soc. Rev.* **38,** 372–390 (2009).

81. Frangioni, J. V. New technologies for human cancer imaging. *J. Clin. Oncol.* **26,** 4012–4021 (2008).

82. Sinha, C. *et al.* Förster Resonance Energy Transfer - An approach to visualize the spatiotemporal regulation of macromolecular complex formation and compartmentalized cell signaling. *Biochim. Biophys. Acta - Gen. Subj.* **1840,** 3067–3072 (2014).

83. Mohamed, M. M. & Sloane, B. F. Cysteine cathepsins: multifunctional enzymes in cancer. *Nat. Rev. Cancer* **6,** 764–775 (2006).

84. Swierczewska, M., Lee, S. & Chen, X. The design and application of fluorophore–gold nanoparticle activatable probes. *Phys. Chem. Chem. Phys.* **13,** 9929 (2011).

85. Chen, G., Qiu, H., Prasad, P. N. & Chen, X. Upconversion Nanoparticles: Design, Nanochemistry, and Applications in Theranostics. *Chem. Rev.* **114,** 5161–5214 (2014).

86. Cheng, Z., Zaki, A. Al, Hui, J., Muzykantov, V. & Tsourkas, A. Multifunctional nanoparticles: cost versus benefit of adding targeting and imaging capabilities. *Science (80-.).* **338,** 903–910 (2012).

87. Wang, F. *et al.* Doxorubicin-tethered responsive gold nanoparticles facilitate intracellular drug delivery for overcoming multidrug resistance in cancer cells. *ACS Nano* **5,** 3679–3692 (2011).

88. Calderón, M. *et al.* Development of efficient acid cleavable multifunctional prodrugs derived from dendritic polyglycerol with a poly(ethylene glycol) shell. *J. Control. Release* **151,** 295–301 (2011).

89. Tauro, M., McGuire, J. & Lynch, C. C. New approaches to selectively target cancer-associated matrix metalloproteinase activity. *Cancer Metastasis Rev.* **33,** 1043–1057 (2014).

90. Xia, K., Zhang, L., Huang, Y. & Lu, Z. Preparation of Gold Nanorods and Their Applications in Photothermal Therapy. *J. Nanosci. Nanotechnol.* **15,** 63–73 (2015).

91. Luke, G. P., Yeager, D. & Emelianov, S. Y. Biomedical applications of photoacoustic imaging with exogenous contrast agents. *Ann. Biomed. Eng.* **40,** 422–437 (2012).

92. Wu, D., Huang, L., Jiang, M. & Jiang, H. Contrast Agents for Photoacoustic and Thermoacoustic Imaging: A Review. *Int. J. Mol. Sci.* **15,** 23616–23639 (2014).

93. Kircher, M. F., Weissleder, R. & Josephson, L. A Dual Fluorochrome Probe for Imaging Proteases. *Bioconjug. Chem.* **15,** 242–248 (2004).

94. Xu, J.-H. *et al.* Supramolecular gelatin nanoparticles as matrix metalloproteinase responsive cancer cell imaging probes. *Chem. Commun.* **49,** 4462–4 (2013).

95. Lee, D.-E. *et al.* Multifunctional nanoparticles for multimodal imaging and theragnosis. *Chem. Soc. Rev.* **41,** 2656 (2012).

96. Razgulin, A., Ma, N. & Rao, J. *Strategies for in vivo imaging of enzyme activity: an overview and recent advances. Chemical Society reviews* **40,** (2011).

97. Kruger, R. Photoacoustic ultrasound. *Med. Phys.* **21,** 127–131 (1994).

98. Burton, N. C. *et al.* Multispectral Opto-acoustic Tomography (MSOT) of the Brain and Glioblastoma Characterization. *Neuroimage* **65,** 522–528 (2013).

99. Tzoumas, S., Nunes, A., Deliolanis, N. C. & Ntziachristos, V. Effects of multispectral excitation on the sensitivity of molecular optoacoustic imaging. *J. Biophotonics* **9999,** n/a-n/a (2014).

100. Ntziachristos, V. & Razansky, D. Molecular imaging by means of multispectral optoacoustic tomography (MSOT). *Chem. Rev.* **110,** 2783–2794 (2010).

101. De La Zerda, A. *et al.* Family of enhanced photoacoustic imaging agents for high-sensitivity and multiplexing studies in living mice. *ACS Nano* **6,** 4694–4701 (2012).

102. Buehler, A. *et al.* High resolution tumor targeting in living mice by means of multispectral optoacoustic tomography. *EJNMMI Res.* **2,** 14 (2012).

103. Balasundaram, G. *et al.* Molecular photoacoustic imaging of breast cancer using an actively targeted conjugated polymer. *Int. J. Nanomedicine* **10,** 387–397 (2015).

104. Tzoumas, S., Deliolanis, N., Morscher, S. & Ntziachristos, V. Unmixing molecular agents from absorbing tissue in multispectral optoacoustic tomography. *IEEE Trans. Med. Imaging* **33,** 48–60 (2014).

105. Taruttis, a., van Dam, G. M. & Ntziachristos, V. Mesoscopic and Macroscopic Optoacoustic Imaging of Cancer. *Cancer Res.* **75,** 1548–1560 (2015).

106. Herzog, E., Taruttis, A., Beziere, N., Lutich, A. a & Razansky, D. Optical imaging of cancer heterogeneity with Multispectral optoacosutic tomography. *Radiology* **263,** 461–468 (2012).

107. Beziere, N. *et al.* Dynamic imaging of PEGylated indocyanine green (ICG) liposomes within the tumor microenvironment using multi-spectral optoacoustic tomography (MSOT). *Biomaterials* **37,** 415–424 (2015).

108. Hudson, S. V. *et al.* Targeted Noninvasive Imaging of EGFR-Expressing Orthotopic Pancreatic Cancer Using Multispectral Optoacoustic Tomography. *Cancer Res.* **74,** 6271–6279 (2014).

109. Bao, C. *et al.* Gold nanoprisms as optoacoustic signal nanoamplifiers for in vivo bioimaging of gastrointestinal cancers. *Small* **9,** 68–74 (2013).

110. Levi, J. *et al.* Molecular Photoacoustic Imaging of Follicular Thyroid Carcinoma. *Clin. Cancer Res.* **19,** 1494–1502 (2013).

111. Beziere, N. *et al.* Optoacoustic imaging and staging of inflammation in a murine model of arthritis. *Arthritis Rheumatol.* **66,** 2071–2078 (2014).

112. Vonnemann, J. *et al.* Polyglycerolsulfate functionalized gold nanorods as optoacoustic signal nanoamplifiers for in vivo bioimaging of rheumatoid arthritis. *Theranostics* **4,** 629–641 (2014).

113. Taruttis, A. *et al.* Multispectral optoacoustic tomography of myocardial infarction. *Photoacoustics* **1,** 3–8 (2013).

114. Morscher, S., Driessen, W. H. P., Claussen, J. & Burton, N. C. Semi-quantitative multispectral optoacoustic tomography (MSOT) for volumetric PK imaging of gastric emptying. *Photoacoustics* **2,** 103–110 (2014).

115. Stritzker, J. *et al.* Vaccinia virus-mediated melanin production allows MR and optoacoustic deep tissue imaging and laser-induced thermotherapy of cancer. *Proc. Natl. Acad. Sci. U. S. A.* **110,** 3316–20 (2013).

116. Taruttis, A., Morscher, S., Burton, N. C., Razansky, D. & Ntziachristos, V. Fast multispectral optoacoustic tomography (MSOT) for dynamic imaging of pharmacokinetics and biodistribution in multiple organs. *PLoS One* **7,** e30491 (2012).

117. Laurent, S. *et al.* Magnetic iron oxide nanoparticles: Synthesis, stabilization, vectorization, physicochemical characterizations and biological applications. *Chem. Rev.* **108,** 2064–2110 (2008).

118. Thomas, R., Park, I.-K. & Jeong, Y. Y. Magnetic iron oxide nanoparticles for multimodal imaging and therapy of cancer. *Int. J. Mol. Sci.* **14,** 15910–30 (2013).

119. Lam, T., Pouliot, P., Avti, P. K., Lesage, F. & Kakkar, A. K. Superparamagnetic iron oxide based nanoprobes for imaging and theranostics. *Adv. Colloid Interface Sci.* **199–200,** 95–113 (2013).

120. Estelrich, J., Sanchez-Martin, M. J. & Busquets, M. A. Nanoparticles in magnetic resonance imaging: from simple to dual contrast agents. *Int. J. Nanomedicine* **10,** 1727–1741 (2015).

121. Choi, H. S. *et al.* Renal clearance of nanoparticles. *Nat. Biotechnol.* **25,** 1165–1170 (2007).

122. Chertok, B., Cole, A. J., David, A. E. & Yang, V. C. Comparison of electron spin resonance spectroscopy and inductively-coupled plasma optical emission spectroscopy for biodistribution analysis of iron-oxide nanoparticles. *Mol. Pharm.* **7,** 375–385 (2010).

123. Neuberger, T., Schöpf, B., Hofmann, H., Hofmann, M. & Von Rechenberg, B. Superparamagnetic nanoparticles for biomedical applications: Possibilities and limitations of a new drug delivery system. *J. Magn. Magn. Mater.* **293,** 483–496 (2005).

124. Wahajuddin & Arora, S. Superparamagnetic iron oxide nanoparticles: Magnetic nanoplatforms as drug carriers. *Int. J. Nanomedicine* **7,** 3445–3471 (2012).

125. Acharya, S. & Sahoo, S. K. PLGA nanoparticles containing various anticancer agents and tumour delivery by EPR effect. *Adv. Drug Deliv. Rev.* **63,** 170–183 (2011).

126. Bronstein, L. M. *et al.* Nanoparticles by decomposition of long chain iron carboxylates: From spheres to stars and cubes. *Langmuir* **27,** 3044–3050 (2011).

127. Lee, N. *et al.* Magnetosome-like ferrimagnetic iron oxide nanocubes for highly sensitive MRI of single cells and transplanted pancreatic islets. *Proc. Natl. Acad. Sci. U. S. A.* **108,** 2662–2667 (2011).

128. Mohapatra, J., Mitra, A., Tyagi, H., Bahadur, D. & Aslam, M. Iron oxide nanorods as high-performance magnetic resonance imaging contrast agents. *Nanoscale* **7,** 9174–9184 (2015).

129. Roca, a G. *et al.* Progress in the preparation of magnetic nanoparticles for applications in biomedicine. *J. Phys. D. Appl. Phys.* **42,** 224002 (2009).

130. Shokrollahi, H. Structure, synthetic methods, magnetic properties and biomedical applications of ferrofluids. *Mater. Sci. Eng. C* **33,** 2476–2487 (2013).

131. Bautista, M. C. *et al.* Comparative study of ferrofluids based on dextran-coated iron oxide and metal nanoparticles for contrast agents in magnetic resonance imaging. *Nanotechnology* **15,** S154–S159 (2004).

132. Reddy, L. H., Arias, J. L., Nicolas, J. & Couvreur, P. Magnetic nanoparticles: design and characterization, toxicity and biocompatibility, pharmaceutical and biomedical applications. *Chem. Rev.* **112,** 5818–78 (2012).

133. Geraldes, C. F. G. C. & Laurent, S. Classification and basic properties of contrast agents for magnetic resonance imaging. *Contrast Media Mol. Imaging* **4,** 1–23 (2009).

134. Weinstein, J. S. *et al.* Superparamagnetic iron oxide nanoparticles: diagnostic magnetic resonance imaging and potential therapeutic applications in neurooncology and central nervous system inflammatory pathologies, a review. *J. Cereb. blood flow Metab.* **30,** 15–35 (2010).

135. Lim, Ekn. for T. R. A. and F. C. *et al.* Nanomaterials for Theranostics: Recent Advances and Future Challenges. *Chem. Rev.* (2014). doi:Nanomaterials for Theranostics: Recent Advances and Future Challenges

136. Dorofeev, G. a., Streletskii, a. N., Povstugar, I. V., Protasov, a. V. & Elsukov, E. P. Determination of nanoparticle sizes by X-ray diffraction. *Colloid J.* **74,** 675–685 (2012).

137. Bom, D. *et al.* Thermogravimetric Analysis of the Oxidation of Multiwalled Carbon Nanotubes: Evidence for the Role of Defect Sites in Carbon Nanotube Chemistry. *Nano Lett.* **2,** 615–619 (2002).

138. Chatterjee, J., Haik, Y. & Chen, C.-J. Size dependent magnetic properties of iron oxide nanoparticles. *J. Magn. Magn. Mater.* **257,** 113–118 (2003).

139. Lee, J. H., Kim, J. W. & Cheon, J. Magnetic nanoparticles for multi-imaging and drug delivery. *Mol. Cells* **35,** 274–284 (2013).

140. Thorek, D. L. J., Chen, A. K., Czupryna, J. & Tsourkas, A. Superparamagnetic iron oxide nanoparticle probes for molecular imaging. *Ann. Biomed. Eng.* **34,** 23–38 (2006).

141. Anderson, S. a *et al.* Magnetic resonance contrast enhancement of neovasculature with alpha(v)beta(3)-targeted nanoparticles. *Magn. Reson. Med.* **44,** 433–439 (2000).

142. Cole, A. J., David, A. E., Wang, J., Galbán, C. J. & Yang, V. C. Magnetic brain tumor targeting and biodistribution of long-circulating PEG-modified, cross-linked starch-coated iron oxide nanoparticles. *Biomaterials* **32,** 6291–6301 (2011).

143. Cheon, J. & Lee, J. H. Synergistically integrated nanoparticles as multimodal probes for nanobiotechnology. *Acc. Chem. Res.* **41,** 1630–1640 (2008).

144. Xu, H. *et al.* Antibody conjugated magnetic iron oxide nanoparticles for cancer cell separation in fresh whole blood. *Biomaterials* **32,** 9758–9765 (2011).

145. Samanta, A. & Ravoo, B. J. Magnetic Separation of Proteins by a Self-Assembled Supramolecular Ternary Complex. *Angew. Chemie Int. Ed.* **53,** 12946–12950 (2014).

146. Cano, M., Sbargoud, K., Allard, E. & Larpent, C. Magnetic separation of fatty acids with iron oxide nanoparticles and application to extractive deacidification of vegetable oils. *Green Chem.* **14,** 1786 (2012).

147. Liu, X., Hu, Q., Fang, Z., Zhang, X. & Zhang, B. Magnetic chitosan nanocomposites: A useful recyclable tool for heavy metal ion removal. *Langmuir* **25,** 3–8 (2009).

148. Palchoudhury, S. & Lead, J. R. A Facile and Cost-Effective Method for Separation of Oil − Water Mixtures Using Polymer-Coated Iron Oxide Nanoparticles. *Environ. Sci. Technol.* **48,** 14558–14563 (2014).

149. Liao, S.-H. *et al.* Functionalized magnetic iron oxide / alginate core- shell nanoparticles for targeting hyperthermia. *Int. J. Nanomedicine* **10,** 3315–3328 (2015).

150. Liu, Y., Yuan, M., Qiao, L. & Guo, R. An efficient colorimetric biosensor for glucose based on peroxidase-like protein-Fe3O4 and glucose oxidase nanocomposites. *Biosens. Bioelectron.* **52,** 391–396 (2014).

151. Gu, W. *et al.* Stabilized, Superparamagnetic Functionalized Graphene/Fe3O4@Au Nanocomposites for a Magnetically-Controlled Solid-State Electrochemiluminescence Biosensing Application. *Anal. Chem.* **87,** 1876–1881 (2015).

152. Quan, Q. *et al.* HSA coated iron oxide nanoparticles as drug delivery vehicles for cancer therapy. *Mol. Pharm.* **8,** 1669–1676 (2011).

153. Sun, C. *et al.* Tumor-targeted drug delivery and MRI contrast enhancement by chlorotoxin-conjugated iron oxide nanoparticles. *Nanomedicine* **3,** 495–505 (2008).

154. Ren, Y. *et al.* Facile, high efficiency immobilization of lipase enzyme on magnetic iron oxide nanoparticles via a biomimetic coating. *BMC Biotechnol.* **11,** 63 (2011).

155. Sommaruga, S. *et al.* Immobilization of carboxypeptidase from Sulfolobus solfataricus on magnetic nanoparticles improves enzyme stability and functionality in organic media. *BMC Biotechnol.* **14,** 82 (2014).

156. Hola, K., Markova, Z., Zoppellaro, G., Tucek, J. & Zboril, R. Tailored functionalization of iron oxide nanoparticles for MRI, drug delivery, magnetic separation and immobilization of biosubstances. *Biotechnol. Adv.* (2015). doi:10.1016/j.biotechadv.2015.02.003

157. Polshettiwar, V. *et al.* Magnetically recoverable nanocatalysts. *Chem. Rev.* **111,** 3036–3075 (2011).

158. Na, H. Bin, Song, I. C. & Hyeon, T. Inorganic nanoparticles for MRI contrast agents. *Adv. Mater.* **21,** 2133–2148 (2009).

159. Cole, A. J. *et al.* Polyethylene glycol modified, cross-linked starch-coated iron oxide nanoparticles for enhanced magnetic tumor targeting. *Biomaterials* **32,** 2183–2193 (2011).

160. Rodriguez, O. *et al.* Contrast-Enhanced In Vivo Imaging of Breast and Prostate Cancer Cells by MRI. *Cell Cycle* **5,** 113–119 (2006).

161. Josephson, L., Kircher, M. F., Mahmood, U., Tang, Y. & Weissleder, R. Near-Infrared Fluorescent Nanoparticles as Combined MR / Optical Imaging Probes. *Bioconjug. Chem.* **13,** 554–560 (2002).

162. Lee, H.-Y. *et al.* PET/MRI dual-modality tumor imaging using arginine-glycine-aspartic (RGD)-conjugated radiolabeled iron oxide nanoparticles. *J. Nucl. Med.* **49,** 1371–1379 (2008).

163. Lee, J. E. *et al.* Uniform mesoporous dye-doped silica nanocrystals for simultaneous enhanced magnetic resonance imaging, fluorescence imaging, and drug delivery. *J. Am. Chem. Soc.* **132,** 552–557 (2010).

164. Cohen, Y. & Shoushan, S. Y. Magnetic nanoparticles-based diagnostics and theranostics. *Curr. Opin. Biotechnol.* **24,** 672–81 (2013).

165. Rosen, J. E., Chan, L., Shieh, D.-B. & Gu, F. X. Iron oxide nanoparticles for targeted cancer imaging and diagnostics. *Nanomedicine* **8,** 275–90 (2012).

166. Riemer, J., Hoepken, H. H., Czerwinska, H., Robinson, S. R. & Dringen, R. Colorimetric ferrozine-based assay for the quantitation of iron in cultured cells. *Anal. Biochem.* **331,** 370–375 (2004).

167. Mahmoudi, M., Sant, S., Wang, B., Laurent, S. & Sen, T. Superparamagnetic iron oxide nanoparticles (SPIONs): development, surface modification and applications in chemotherapy. *Adv. Drug Deliv. Rev.* **63,** 24–46 (2011).

168. Cherry, S. R. Multimodality in vivo imaging systems: twice the power or double the trouble? *Annu. Rev. Biomed. Eng.* **8,** 35–62 (2006).

169. Weber, J., Beard, P. C. & Bohndiek, S. E. Contrast agents for molecular photoacoustic imaging. *Nat. Methods* **13,** 639–50 (2016).

170. Zeiderman, M. R. *et al.* Acidic pH-Targeted Chitosan-Capped Mesoporous Silica Coated Gold Nanorods Facilitate Detection of Pancreatic Tumors via Multispectral Optoacoustic Tomography. *ACS Biomater. Sci. Eng.* **2,** 1108–1120 (2016).

171. Wang, J. *et al.* In vivo pharmacokinetic features and biodistribution of star and rod shaped gold nanoparticles by multispectral optoacoustic tomography. *RSC Adv.* **5,** 7529–7538 (2015).

172. Bao, C. *et al.* Gold Nanoprisms as Optoacoustic Signal Nanoamplifiers for In Vivo Bioimaging of Gastrointestinal Cancers. *Small* **9,** 68–74 (2013).

173. De La Zerda, A. *et al.* Carbon nanotubes as photoacoustic molecular imaging agents in living mice. *Nat. Nanotechnol.* **3,** 557–562 (2008).

174. Bashir, M. R., Bhatti, L., Marin, D. & Nelson, R. C. Emerging applications for ferumoxytol as a contrast agent in MRI. *J. Magn. Reson. Imaging* **41,** 884–898 (2015).

175. Muthiah, M., Park, I.-K. & Cho, C.-S. Surface modification of iron oxide nanoparticles by biocompatible polymers for tissue imaging and targeting. *Biotechnol. Adv.* **31,** 1224–36 (2013).

176. Juang, J. H. *et al.* Magnetic resonance imaging of transplanted mouse islets labeled with chitosan-coated superparamagnetic iron oxide nanoparticles. *Transplant. Proc.* **42,** 2104–2108 (2010).

177. Egusquiaguirre, S. P. *et al.* Optoacoustic imaging enabled biodistribution study of cationic polymeric biodegradable nanoparticles. *Contrast Media Mol. Imaging* (2015). doi:10.1002/cmmi.1644

178. Jin, H., Heller, D. a, Sharma, R. & Strano, M. S. Size-Dependent Cellular Uptake and Expulsion of Single-Walled Carbon Nanotubes : Single Particle Tracking and Nanoparticles. *ACS Nano* **3,** 149–158 (2009).

179. Ju, Y. *et al.* Monodisperse Au–Fe2C Janus Nanoparticles: An Attractive Multifunctional Material for Triple-Modal Imaging-Guided Tumor Photothermal Therapy. *ACS Nano* **11,** 9239–9248 (2017).

180. Lv, G. *et al.* Near-Infrared Emission CuInS/ZnS Quantum Dots: All-in-One Theranostic

Nanomedicines with Intrinsic Fluorescence/Photoacoustic Imaging for Tumor Phototherapy. *ACS Nano* **10,** 9637–9645 (2016).

181. Liu, G., Gao, J., Ai, H. & Chen, X. Applications and potential toxicity of magnetic iron oxide nanoparticles. *Small* **9,** 1533–1545 (2013).

182. Nie, S. Understanding and overcoming major barriers in cancer nanomedicine. *Nanomedicine (Lond).* **5,** 523–528 (2010).

183. López-Otín, C. & Bond, J. S. Proteases: Multifunctional enzymes in life and disease. *J. Biol. Chem.* **283,** 30433–30437 (2008).

184. Atkinson, J. M., Siller, C. S. & Gill, J. H. Tumour endoproteases: the cutting edge of cancer drug delivery? *Br. J. Pharmacol.* **153,** 1344–1352 (2008).

185. Talvensaari-Mattila, a, Pääkkö, P. & Turpeenniemi-Hujanen, T. Matrix metalloproteinase-2 (MMP-2) is associated with survival in breast carcinoma. *Br. J. Cancer* **89,** 1270–1275 (2003).

186. Folgueras, A. R., Pendás, A. M., Sánchez, L. M. & López-Otín, C. Matrix metalloproteinases in cancer: From new functions to improved inhibition. *Int. J. Dev. Biol.* **48,** 411–424 (2004).

187. Jin, R., Lin, B., Li, D. & Ai, H. Superparamagnetic iron oxide nanoparticles for MR imaging and therapy: design considerations and clinical applications. *Curr. Opin. Pharmacol.* **18,** 18–27 (2014).

188. Desgrosellier, J. S. & Cheresh, D. A. Integrins in cancer: biological implications and therapeutic opportunities. *Nat. Rev. Cancer* **10,** 9–22 (2010).

189. Yang, X. *et al.* cRGD-functionalized, DOX-conjugated, and 64Cu-labeled superparamagnetic iron oxide nanoparticles for targeted anticancer drug delivery and PET/MR imaging. *Biomaterials* **32,** 4151–4160 (2011).

190. Xie, J. *et al.* Ultrasmall c(RGDyK)-Coated Fe3O4 Nanoparticles and Their Specific Targeting to Integrin αvβ3-Rich Tumor Cells. *J. Am. Chem. Soc.* **130,** 7542–7543 (2008).

191. Frankowski, H., Gu, Y.-H., Heo, J. H., Milner, R. & del Zoppo, G. J. Use of Gel Zymography to Examine Matrix Metalloproteinase (Gelatinase) Expression in Brain Tissue or in Primary Glial Cultures. *Methods Mol Biol.* **814,** 221–233 (2012).

192. Toth, M. & Fridman, R. Assessment of Gelatinases (MMP-2 and MMP-9) by Gelatin Zymography. *Methods Mol Biol.* **57,** 163–174 (2001).

193. Garnett, M. C. & Kallinteri, P. Nanomedicines and nanotoxicology: Some physiological principles. *Occup. Med. (Chic. Ill).* **56,** 307–311 (2006).

194. Iyer, A. K., Khaled, G., Fang, J. & Maeda, H. Exploiting the enhanced permeability and retention effect for tumor targeting. *Drug Discov. Today* **11,** 812–818 (2006).

195. Chuang, C.-H. *et al.* In Vivo Positron Emission Tomography Imaging of Protease Activity by Generation of a Hydrophobic Product from a Noninhibitory Protease Substrate. *Clin. cancer Res.* **18,** 238–47 (2012).

196. Myochin, T., Hanaoka, K., Komatsu, T., Terai, T. & Nagano, T. Design strategy for a near-infrared fluorescence probe for matrix metalloproteinase utilizing highly cell permeable boron dipyrromethene. *J. Am. Chem. Soc.* **134,** 13730–7 (2012).

197. Wang, H.-X. *et al.* Matrix metalloproteinase 2-responsive micelle for siRNA delivery. *Biomaterials* **35,** 7622–34 (2014).

198. Chau, Y., Tan, F. E. & Langer, R. Synthesis and Characterization of Dextran - Peptide - Methotrexate Conjugates for Tumor Targeting via Mediation by Matrix Metalloproteinase II and Matrix Metalloproteinase IX. *Bioconjug. Chem.* **15,** 931–941 (2004).

199. Kim, J. *et al.* Active targeting of RGD-conjugated bioreducible polymer for delivery of oncolytic adenovirus expressing shRNA against IL-8 mRNA. *Biomaterials* **32,** 5158–5166 (2011).

200. Kessler, T. *et al.* Inhibition of tumor growth by RGD peptide-directed delivery of truncated tissue factor to the tumor vasculature. *Clin. Cancer Res.* **11,** 6317–6324 (2005).

201. Garrigues, H. J., Rubinchikova, Y. E., Dipersio, C. M. & Rose, T. M. Integrin alphaVbeta3 Binds to the RGD motif of glycoprotein B of Kaposi's sarcoma-associated herpesvirus and functions as an RGD-dependent entry receptor. *J. Virol.* **82,** 1570–1580 (2008).

202. Montet, X., Montet-Abou, K., Reynolds, F., Weissleder, R. & Josephson, L. Nanoparticle imaging of integrins on tumor cells. *Neoplasia* **8,** 214–222 (2006).

203. Kilian, K. A. & Mrksich, M. Directing Stem Cell Fate by Controlling the Affinity and Density of Ligand-Receptor Interactions at the Biomaterials Interface. *Angew. Chemie - Int. Ed.* **51,** 4891–4895 (2012).

204. Temming, K., Schiffelers, R. M., Molema, G. & Kok, R. J. RGD-based strategies for selective delivery of therapeutics and imaging agents to the tumour vasculature. *Drug Resist. Updat.* **8,** 381–402 (2005).

205. Juan, H.-F. *et al*. Proteomics analysis of a novel compound: Cyclic RGD in breast carcinoma cell line MCF-7. *Proteomics* **6,** 2991–3000 (2006).